Electronic Engineering
Electronic Micro and Nanosystems

Application of carbon-based materials in hybrid energy storage and harvesting systems

October 2024

Candidate:
Marco Carrozza

Supervisor:
Prof. Andrea Lamberti

Co-supervisors:
Dr. Roberto Speranza
Dr. Pietro Zaccagnini

Contents

Abstract

In a world that is actively trying to reach a more sustainable future, energy storage represents the challenge of the present. As renewable sources are not continuous (in the sense that their availability is affected by factors such as weather and time of day), and energy harvesting devices become more and more efficient, the need for a reliable storage system is critical. In this work, the focus is directed towards the long-term viability of energy storage units, which should encompass environmental impact of manufacturing processes, cyclability and end-of-life disposal. A strong effort is put in designing an hybrid device combining strong power capabilities with high energy density. This is done by exploiting a supercapacitor's (SC) double layer charge mechanism coupled with reversible faradaic reactions from a battery-like electrode. The final goal of the project is to connect the SC to an appropriately sized dye-sensitized solar cell (DSSC), so that their combined operation can drive low-power sensors and devices in a charge/discharge cycle alternating between day and night. The whole system would therefore be self-sustaining and low maintenance thanks to the reversibility of the charge and discharge processes. To ensure environmental friendliness, the choice of materials includes low-cost and widely available compounds, such as carbon-based substances and lithium manganese oxide, the latter being a strong alternative to lithium cobalt oxide, which has dominated the battery market but raises sustainability concerns due to limited availability, environmental impact from mining, and recycling challenges. The carbon-based source in this case comes from agricultural waste, in the form of rice husk (RH), which has already exploited as a source of silica in literature. The RH has been transformed in a 4-step procedure into carbon aerogel, which provides the porous structure yielding the high surface-to-volume ratio needed to reach a considerable capacitance. All in all, the final device aims to be a significant step towards achieving net zero carbon emissions by integrating sustainable materials and advanced energy storage technologies. With the combination of SCs and DSSCs, this approach hopefully contributes to a more sustainable future and sets a precedent for new developments in eco-friendly energy storage systems.

Chapter 1

Introduction

1.1 Power and Energy density

The main characteristic of energy storage devices is the ability to store power under the form of electrical charges that are later delivered to a load. The main difference between different classes is about power delivery and working mechanism.
A straightforward explanation is visually presented using a Ragone plot, the standard comparison graph for various types of energy storage devices. It's always in logarithmic scale and there are isostatic straight lines indicating maximum charge and discharge times. As we can see from **Fig. 1.1**, the criteria for the classification is determined on the base of power and energy densities.
For energy storage devices, the definition of energy density is:

$$E_{density} = \frac{1}{2}\frac{C\Delta V^2}{m} \tag{1.1}$$

while the power density definition is:

$$P_{density} = \frac{E_{density}}{\Delta t} = \frac{I\Delta V}{2m} \tag{1.2}$$

with m mass of the device, C the resulting value of capacitance, ΔV the maximum rated voltage and I the maximum current that the component is able to deliver.
The higher the power density, the faster the device is able to deliver a large quantity of charges towards the selected load; the higher the energy density instead, the longer the device is able to power the load without recharging.

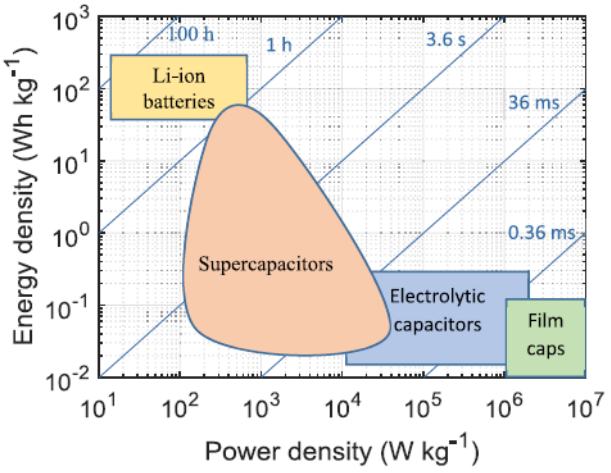

Figure 1.1: Ragone plot rating the various technlogies.[2]

These two are very desirable characteristics in most applications and therefore the closer the placement of the device is in the upper-right corner of the graph, the better its overall performance.

1.2 Energy storage devices

Since many ways to store energy are possible, the classification we will apply comprehends only electronic and electrochemical devices like batteries, capacitors and supercapacitors. Each one exploits different mechanisms in order to store charges and a brief examination about individual characteristics will be conducted in the following.

1.2.1 Batteries

Batteries are made by multiple electrochemical cells, connected in series or parallel depending on voltage and current requirements. The key to understanding a battery therefore lies in the working mechanism of a single cell, which is able to convert chemical into electrical energy and viceversa through redox reactions. When a material is oxidating electrons are lost, while reduction means elctron gain.
An electrochemical cell is made of 3 components (see **Fig. 1.2**):

- *Anode (in this case, negative electrode)*: it's the elctrode that gives up electrons to the load, and that is oxidized in the process.
- *Cathode (in this case, positive electrode)*: it's the elctrode that receives elec-

trons from the external circuit, and is therefore reduced while the reaction happens.

- *Electrolyte*: it's the liquid or sometimes solid-state material that acts as the ionic conductor of charges (from electrons to ions) between the two electrodes.

The process of charging and discharging a battery involves the flow of current through a wire connected to a load or power source, and the movement of charged particles inside the cell. When the battery discharges, electrons flow from the negative terminal, through an external load, to the positive terminal. Inside the cell, negatively charged anions move toward the negative electrode, while positively charged cations move toward the positive electrode. Oxidation (loss of electrons) occurs at the negative electrode, and reduction (gain of electrons) happens at the positive electrode. The processes reverse when charging the battery.
The core concept is that during discharge, the battery loses energy as electrons flow from negative to positive, and during recharging, energy is stored. The anode and cathode switch roles depending on whether the battery is charging or discharging [4].

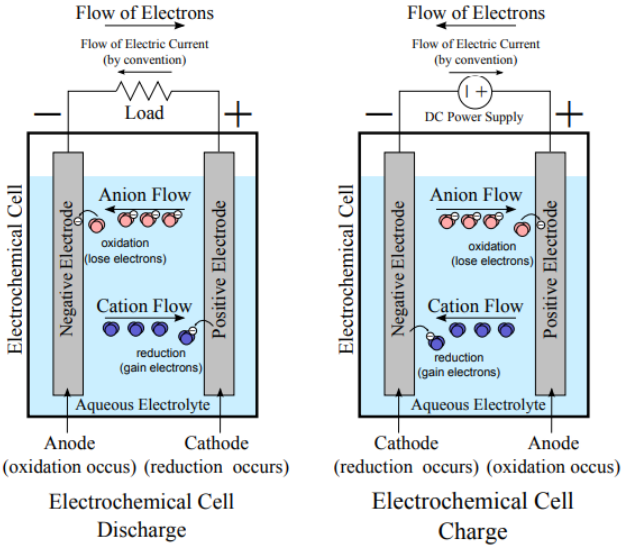

Figure 1.2: Charge and discharge process of an electrochemical cell. [4]

One important aspect in the working mechanism of batteries is the exploitation of faradaic reactions. These processes describe the way in which ions react with electrodes: during discharge the ions contained in the electrolyte are intercalated into the anode/cathode and diffuse into the electrode's material itself. This can also trap charges, causing damage to the device, which in the long run stops working.

That's why most rechargeable batteries today are guaranteed for a specified number of cycles.

A battery electrode can be easily identified by its cyclic voltammetry (an investigation technique that will be better described later). As we can see in **Fig. 1.3**, the current peaks happen at specified voltages that correspond to the intercalation potential, changing based on multiple factors. This also explains why a battery is able to keep a constant voltage during discharge, contrary to a capacitor.

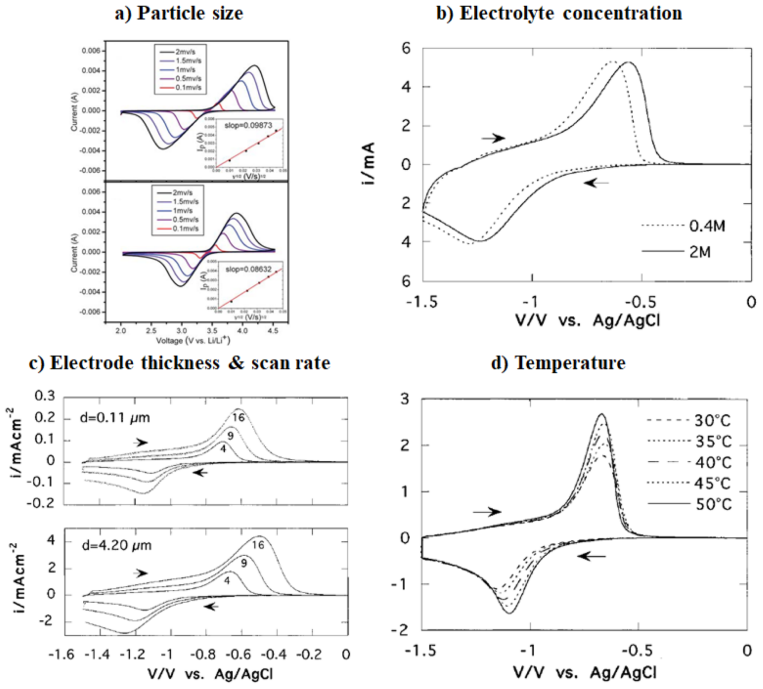

Figure 1.3: Changes in a battery CV due to particle size of active materials, temperature, electrolyte concentration, thickness and scan rate. [17]

1.2.2 Capacitors

Capacitors are passive elements widely used in electronics. They are composed of two parallel plates with surface A separated by a dielectric material with thickness d (as in **Fig. 1.4**).

Depending on technology the polarity of the plates can be inverted or is fixed, and their applications vary from producing latency to filtering out frequencies in telecommunications. Because of their ability to release charge faster than any other device (observe **Fig. 1.1**), they are not suitable for powering up other devices. While batteries have more or less constant voltage during usage, capacitors have an

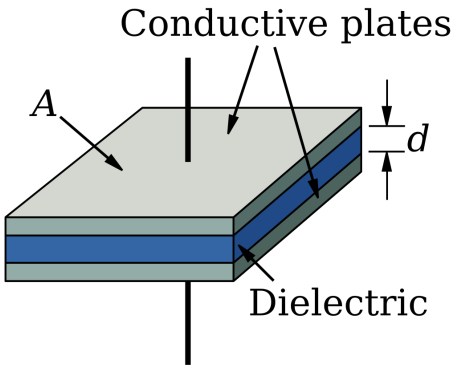

Figure 1.4: Parallel plate capacitor representation. [43]

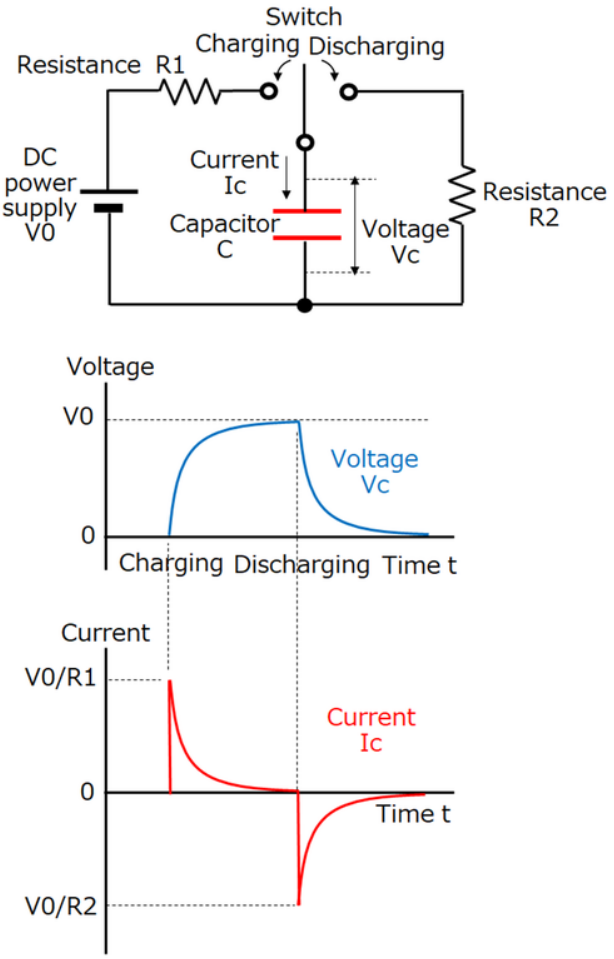

Figure 1.5: Charging and discharging curve of a capacitor through two different resitors. [29]

exponential voltage decrease while discharging (see **Fig. 1.5**), preventing most ICs from functioning correctly due to above-threshold power supply requirements.
Capacitance is calculated based on device geometry and relative dielectric constant of the medium:

$$C = \frac{\epsilon_r A}{d} \tag{1.3}$$

Other important parameters for performance evaluation and design are: maximum rated voltage, equivalent series resistance (which is a non-ideality indicator) and tolerances.

1.2.3 Supercapacitors

Supercapacitors (SCs) are electrochemical devices able to reach far higher capacity than standard silicon-based capacitors. As we can see by the Ragone plot (**Fig. 1.1**), they are by far the most flexible technology, able to combine together high power and energy density. A lot of effort is currently being put researching materials and ways to exploit their features as efficiently as possible. This work is no different, trying to find a good sustainability-performance combination in an emerging technology. An in-depth description of these devices will be given in **Sec. 1.4**.

1.3 Solar energy harvesting

Renewable energy harvesting refers to the process of capturing and converting natural energy sources into usable power. While a plethora of green sources is available to exploit, the largest and most promising is without a doubt solar energy. In fact, around $\sim$1000 W/m^2 worth of photons strike the Earth's surface continuously: with a pessimistic view, considering only 35% of sunlight getting through the atmosphere and only measuring radiation falling onto land masses, the sun generates roughly 23k TW per year; to put it into perspective, the yearly world energy consumption in 2009 was 15 TW (expected to double in 2050) [30]. As we can see from **Fig. 1.6**, solar power greatly surpasses all other finite and renewable sources as well, making it the most interesting option for large-scale energy harvesting.

A comprehensive overview of all solar energy harvesting methods and technologies is beyond the scope of this discussion. However, it is important to note the evolution of photovoltaic systems since the 90s. Early developments focused on monocrystalline, polycrystalline, and amorphous silicon cells, each offering progressively higher efficiencies. More recent advancements, such as perovskite-based solar cells and tandem cells, which use multiple materials to capture a broader spectrum of sunlight, have set new efficiency standards. That said, in the following we will briefly describe the behavior and working mechanism of a dye-sensitized solar cell (DSSC), since it's the chosen technology coupled with the designed storage unit.

1.3.1 Review on Dye-Sensitized Solar Cells

DSSCs are an extensively researched subject for their potential in terms of large scale production as well as cheapness and availability of materials for their construction. The number of publications slowed down during the years because of the strict device stability needed for the exposure to strong illuminating outdoor conditions, as well as the rise of perovskites as the top-efficiency technology. Recently the discussion on DSSCs has been revamped because of the much higher conversion effectiveness

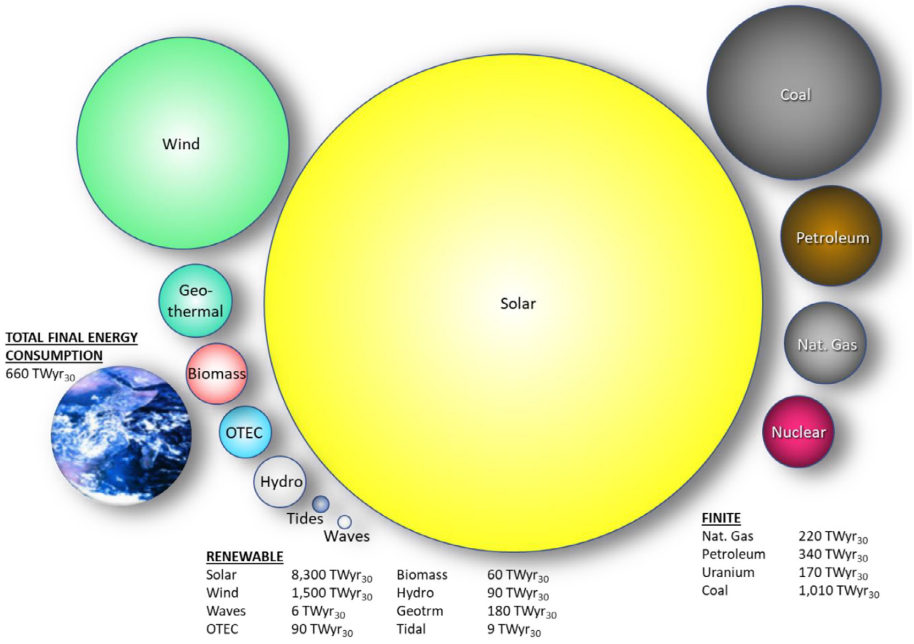

Figure 1.6: Estimate of finite and renewable planetary energy reserves (TW-yr, 2022). Total recoverable reserves are shown for the finite resources. Yearly potential is shown for the renewables. [30]

demonstrated while working under diffused and indoor light.

The structure of a DSSC can be broken down into three major elements:

Photoanode, or photoelectrode: this is a thin film (tenths of μm) made of a n-type semiconductor, most applications use interconnected titanium dioxide (TiO_2) nanoparticles, with sub-micrometric diameter. The surface of these nanoparticles is coated with a monolayer of dye molecules that absorb light. Animportant characteristic of the semiconductor is porosity, since a large internal surface area allows more dye to attach, maximizing light absorption. This film is deposited onto a transparent conductive oxide (TCO) coated substrate (glass or plastic). The nanoporous TiO_2 ensures that each dye molecule has contact with both the TiO_2 and the electrolyte.

Electrolyte: it fills the pores of the TiO_2 film and the gap between the photoanode and counter electrode. It contains a redox couple, typically iodine (I^-) and triiodide (I_3^-), dissolved in an organic solvent. The electrolyte plays a key role in regenerating the oxidized dye and shuttling ions between the electrodes, facilitating continuous operation of the cell. It also enables ionic conduction to balance the charges during the cell's operation.

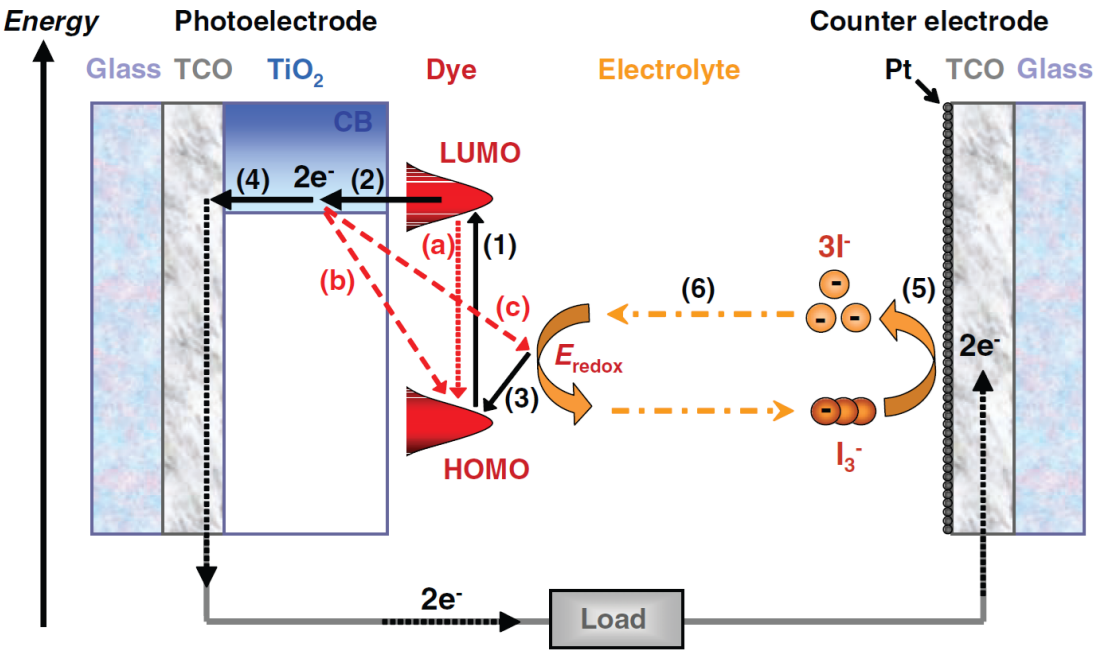

Figure 1.7: Illustrated working mechanism of DSSCs. [14]

Counter electrode: it consists of a TCO glass substrate, coated with a catalyst for the redox reaction; usually platinum particles. The counter electrode collects the electrons returning from the external circuit and facilitates their reaction with the redox couple in the electrolyte to complete the internal circuit of the DSSC.

The choice of materials for DSSCs is strictly dictated by how the energy levels align between the different components.
As we can see from **Fig. 1.7**, the process starts at the photoanode, where light absorption takes place. When a photon ($h\nu$) hits a dye (S) molecule, it excites an electron from the dye's highest occupied molecular orbital (HOMO) to its lowest unoccupied molecular orbital (LUMO) (Step 1 in the figure, S^*). This excited electron is then injected into the conduction band (CB) of the TiO_2 semiconductor (Step 2). From there, the electron diffuses through the TiO_2 film and reaches the transparent conductive oxide (TCO) layer, eventually moving towards the external circuit (Step 4). This flow of electrons through the external load generates electrical power.
Once the electron leaves the dye, the dye molecule is left in an oxidized state (S^+). The dye is regenerated by accepting electrons from the redox couple in the electrolyte, typically iodine (I^-) ions (Step 3). The electrons that traveled through the external circuit eventually return to the cell at the counter electrode, which is coated

with a platinum (Pt) catalyst. Here, triiodide (I_3^-) in the electrolyte is reduced back to iodine ions (I^-) by accepting these returning electrons (Step 5). The cycle is then completed as the iodine and triiodide ions move through the electrolyte, maintaining the charge balance and enabling continuous operation of the DSSC (Step 6).
This process can be summarized, using the numbers in **Fig. 1.7**, as follows:

Photoanode:

$$S + h\nu \rightarrow S^* \quad \textit{light absorbed} \quad (1)$$

$$S^* \rightarrow S^+ + e^- \ (TiO_2) \quad \textit{electron injection} \quad (2)$$

$$2S^+ + 3I^- \rightarrow 2S + I_3^- \quad \textit{dye regeneration} \quad (3)$$

$$2e^- \ (TiO_2) \rightarrow 2e^- \ (TCO_{PE}) \rightarrow \text{Load} \rightarrow 2e^- \ (TCO_{CE}) \quad \textit{current generation} \quad (4)$$

Counter electrode:

$$I_3^- + 2e^- \rightarrow 3I^- \quad \textit{reduction} \quad (5)$$

Electrolyte:

$$I_3^- \ (PE) \rightarrow I_3^- \ (CE) \quad \textit{ionic transport} \quad (6)$$

Where $h\nu$ represents the photon absorbed by the dye, and the subsequent electron flow through the external load provides the electrical output of the DSSC.

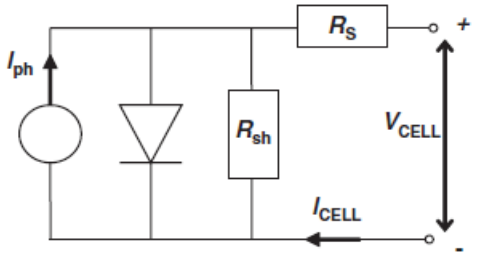

Figure 1.8: Basic diode equivalent circuit for a solar cell. [14]

Different models are used in literature to describe these devices as accurately as possible; in the context of this particular work, solar cells act more as a current generator and while it is important to understand the simplest equivalent circuit (**Fig. 1.8**) to comprehend its limitations, the following description will be only scratching the surface of the complexity hidden behind this device's design. The shape of a DSSC IV curve can be reproduced using the following equation:

$$i_{\text{CELL}} = i_{\text{ph}} - i_0 \left(e^{\frac{q_e(V_{\text{CELL}} + i_{\text{CELL}} R_s)}{n k_B T}} - 1 \right) + \frac{V_{\text{CELL}} + i_{\text{CELL}} R_s}{R_{\text{sh}}} \tag{1.4}$$

where i_{ph} is the generated photocurrent, i_0 is the dark current of the diode, k_B is the Boltzmann constant, T is the temperature in K and R_s and R_{sh} are the series and shunt resistances of the cell [14]. These parameters can be obtained from fitting the measured curve with **Eq. 1.4**.

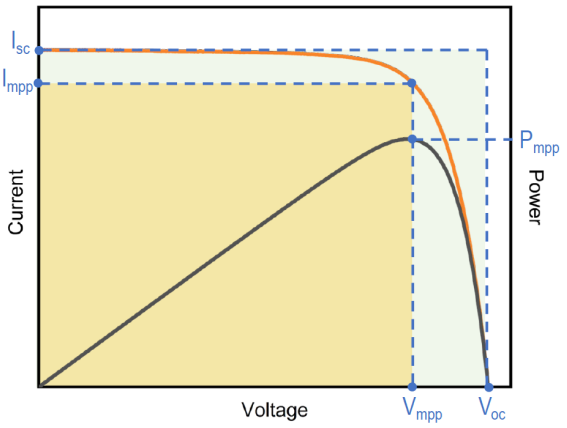

Figure 1.9: Example of typical DSSC IV curve.

From the actual IV curve (an example can be seen in **Fig. 1.9**) it is possible to obtain complementary information regarding DSSC usage and efficiency, such as:

- I_{sc}, or short circuit current, which is the maximum current that flows in the device when no voltage is applied to it.
- V_{oc}, or open circuit voltage, which is the maximum voltage showing at the two terminals of the device when no current is flowing.
- P_{mpp}, or maximum generated power, is the point in which the V·I product reaches its maximum.
- FF, or fill factor, is a rough estimation of the ideality of the solar cell: it is calculated as the ratio between the smaller area indicated by I_{mpp} and V_{mpp} and the larger one, or simply by dividing the P_{mpp} for the product of V_{oc} times I_{sc}.
- η, or photo-conversion efficiency, which measures the effectiveness of the device in converting radiation into electrical power, calculated as $\eta = \frac{P_{mpp}}{P_{in}}$, where P_{in} is the incident power due to light radiation.

Having covered the key aspects of DSSCs, let us now shift our focus onto the main subject of this work: supercapacitors.

1.4 Review on Supercapacitors

The purpose of this section is to describe the electrochemical mechanisms and the materials involved in the energy storage process of supercapacitors.
The basic structure of a supercapacitor is similar to an electrochemical cell, with two electrodes composed by a current collector with some active material on top, a solid or liquid electrolyte and a separator or membrane in-between to avoid short circuits. The main difference with a battery is that the active compund on top of the current collector is porous: the porosity increases greatly the area of the electrode thus making the surface A of the equivalent parallel plate capacitor very high. Energy is stored using the electric field that is created at the electrolyte-electrode interface, also reducing the distance d between equivalent plates. The two effects combined significantly boost the capacity of our device, as we can understand from **Eq. 1.3**.

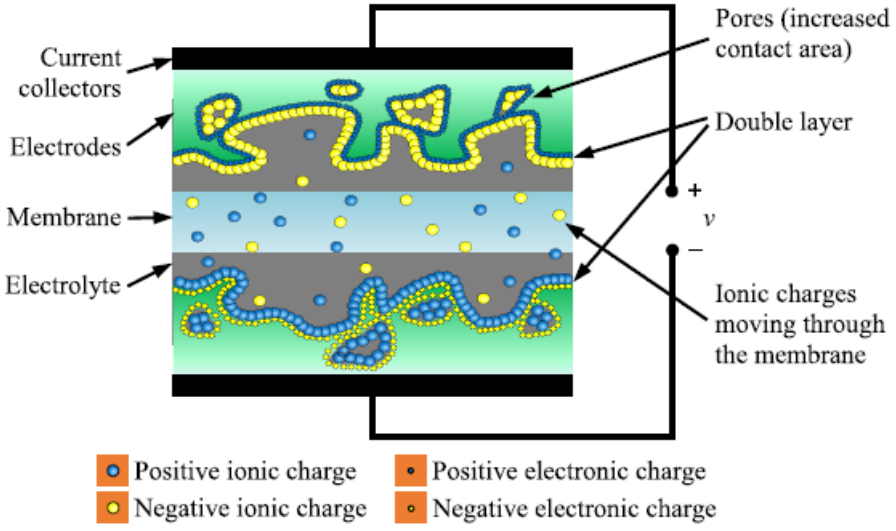

Figure 1.10: Representation of supercapacitor structure.[2]

In **Fig. 1.10** we can see a commonly used structure for a SC. The active material composing the electrode is clearly porous, while the membrane is intended to be ion-conductive, to favor the passage of different ions in one direction; most supercapacitors are in fact polarized. While charging ions align near the oppositely charged electrode as represented, and get released as the device discharges.
Another important concept to grasp is the voltage stability window of the device, which is determined based on electrolyte and electrode's material. An helpful visualization of the principle is observable in **Fig. 1.11**. The graph in question is a diagram stating the stable electrochemical window (vs Standard Hydrogen Elec-

trode) of water depending on pH compared to values of redox reactions potentials of electrodes for aqueous potassium-ion batteries (APIBs). While this is specific to aqueous systems, it offers valuable insight into the voltage limitations imposed by electrolytes. A compound will exhibit a stable potential (open circuit potential - OCP) within the electrolyte, and depending on its position relative to the evolution limits, it will have a greater or lesser voltage range as either a cathode or anode.
This also means that in order to exploit the whole capability of the device it is necessary to carefully choose the electrode and electrolyte to design anodic and cathodic voltage window (**Fig. 1.12**). A large difference between the two could lead to complications in charge balancing, which consists in ensuring that the voltage across each cell stays balanced and safe during charging and discharging.

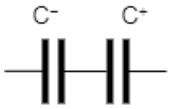

In fact, since both electrodes represent an electrostatic double layer on their own, the true ideal model of a supercapacitor is portrayable as two series capacitors. A device assembled coupling two electrodes will therefore have a total C equal to the series capacitance of the two separated electrodes. The total ΔV will be the sum of the two voltage windows and, assuming coulombic efficiency equal to 100%, the charge will be equally distributed between the two.

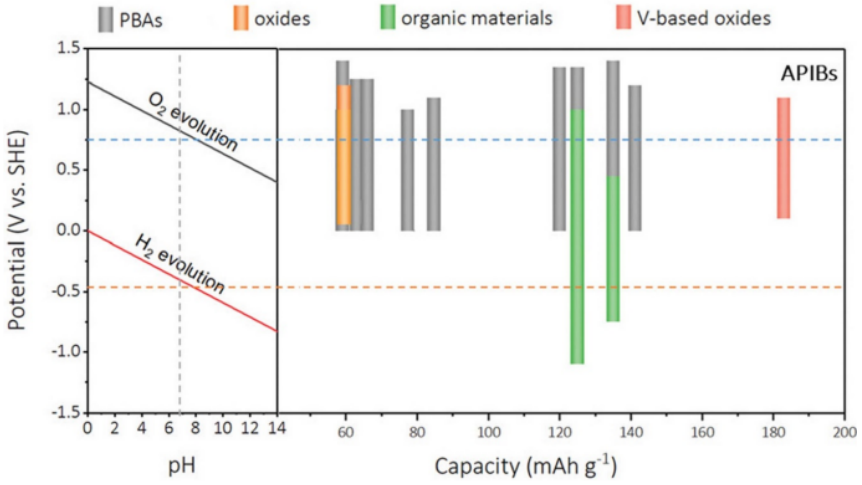

Figure 1.11: Stable electrochemical window in aqueous electrolyte with different pH values and redox potential of electrode materials for APIBs.[44]

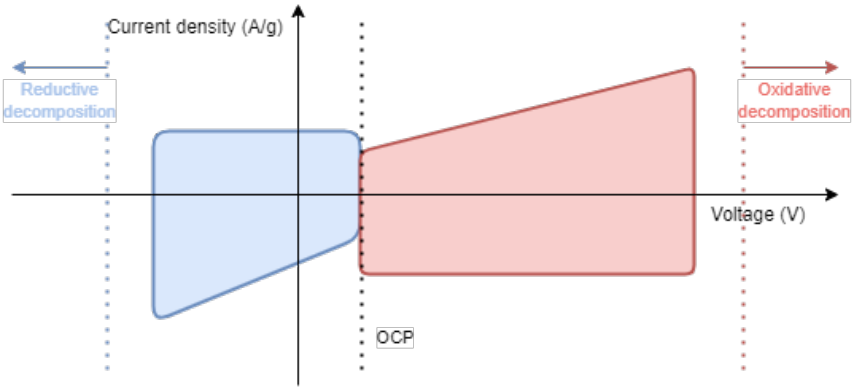

Figure 1.12: An example of anodic and cathodic voltage window of two electrodes taken separately and then connected to form a device.

1.4.1 Key components of a supercapacitor

Current collector

The current collector is typically made from conductive materials and primarily functions as a contact point to access the active material and its stored charge. Conductive materials are defined by their intrinsic property known as resistivity, which increases with temperature due to the rise in phonon energy, leading to a higher probability of electron scattering. Additionally, these materials are effective thermal conductors and tend to expand with increasing temperature.
One of the challenges in electrode design is the interface between the current collector and the active material. A high contact resistance at this interface can significantly contribute to the overall series resistance, impacting the performance of the device.

Active component or storage element

Given that a SC electrode has to have high conductivity, high surface area, chemical stability, high temperature resistance and high porosity, it is usually made by a mixture of components. The main contributor to the capacitive nature of the electrode is a carbon-based highly porous material (in the case of EDLCs, see later) or metal oxide/conductive polymer (for pseudo-capacitive and faradaic electrodes, also see later) [15]. Both of them need a step of functionalization that creates the microporosities in the former and electrochemically activates the latter.
To enhance conductivity of the active material, a conductive agent is usually added to the mixture, like carbon-black (CB) or acetylene-black (AB). Moreover, to increase mechanical properties and adhesion of the electrode, a binder is usually introduced, like PVDF (polyvinylidene fluoride) or CMC (carboxymethyl cellulose). For

both additions, a balanced trade-off in their concentration within the active material must be achieved to ensure both low series resistance and high stability throughout the device's lifespan.
There are two ways to obtain an electrode from the mixture: either using a solution with an appropriate solvent and then coat the current collector by doctor-blade, or compressing the various compounds with an adequate pressure.

Electrolyte

An electrolyte is a material that conducts electricity through the movement of ions. These ions are typically derived from salts that dissociate into their respective cations and anions. When a potential is applied, the ions migrate from the bulk of the solution to the electrode surfaces to balance the charge imbalance induced on the material. This ion movement creates a flow of charges within the solution. The choice of electrolyte, which will be discussed later, is crucial as it significantly influences the final device's characteristics.

Membrane or separator

Not much research has focused on developing well-engineered separators, despite advancements in improving supercapacitor (SC) electrodes. The main purpose of separators is to isolate the two electrodes; if poorly designed they can negatively impact SC performance by increasing cell resistance, and in the worst-case scenario, they could cause short circuits. Key factors in choosing suitable separators for SCs include preventing electron transport between electrodes, chemical resistance, permeability to electrolyte ions with minimal ionic resistance, ease of wetting by electrolytes, and mechanical resistance to changes in volume and pressure.
Initially, natural materials like ceramics, glass, and cellulose paper were used as separators in SCs. However, polymer-based separators have since become more prevalent due to their low cost, excellent flexibility, and high porosity. These polymer separators are typically classified into two types: fibrous structures and monolithic networks with defined pores [15].

1.4.2 Types of SC based on energy storage mechanism

Since a lot of materials have been used in SC design, many energy storage mechanisms have been explored, and knowledge of these process is needed to understand them.

Generally speaking, capacitance value can be calculated easily using the following

equation:

$$C = \frac{\Delta Q}{\Delta V} \tag{1.5}$$

with ΔQ which is the total charge accumulated at the electrolyte-electrode interface, and ΔV is the applied voltage at the device's terminals.

A more useful parameter in SC's characterization is the specific capacitance, which is defined as:

$$C_s = \frac{\Delta Q}{\Delta V \Pi} \tag{1.6}$$

with Π being mass, volume or footprint of the electrode, which corresponds to gravimetric (F/g), volumetric (F/cm^3 or F/mL) and areal capacitance (F/cm^2), respectively. In this work, we have used mAh/g as it is more useful for mass balancing directly; at the end we'll provide also F/g.

Double layer behavior

The electrostatic double layer capacitor (EDLC) exploits the accumulation of charge at the electrolyte-electrode interface. As a voltage source is connected to the terminals of the device, ions in the electrolyte get attracted to the conductive surface of the electrode. The greater the surface of the electrodes, the more charge is possible to store. This phenomenon is typical of carbon fibers, powders and felts; it is called double layer because two layers are effectively created at both electrode's surfaces (see **Fig. 1.10**). Also, since charges are electrostatically stored, the total capacity of the device depends on applied voltage[2].

As we can observe in **Fig. 1.13**, they are identified by a linear voltage behavior when charged with constant current which results in a rectangular cyclic voltammetry (if the device is ideal). These electrodes are generally characterized by fast kinetics, low energy densities and high power capabilities. Finally their cyclability is very high, allowing millions of cycles, because of the non-destructive principle on which the working mechanism relies.

Pseudo-capacitive behavior

Pseudo capacitance results instead from very fast and reversible faradaic reactions, similar to the ones described for batteries. The difference is in the fact that these reactions happen only at the surface of the interface with the electrode. The capacitance in this case is the result of a peculiar thermodynamic relationship among the voltage change and charge acceptance extent [2].
This SC technology has higher specific capacitance and energy density as well. Because of the different phenomenon exploited though, the resulting device has lower

power density and weaker cyclability. It has to be said that the majority of supercapacitors fall into the pseudocapacitive category because o fmarginal reactions taking place because of functional group presence [2].
From what we can see in **Fig. 1.13**, pseudo-capacitance's CV and GCD is a mixture between capacitive and faradaic behavior, with mostly linear response when charging at constant current and some peaks in the cyclic voltammetry due to redox reactions happening.

Faradaic behavior

Faradaic storage mechanism is based off redox reactions inside the electrode crystalline structure (operated by metal ions). Diving a little deeper in the working principle, we have intercalation/deintercalation of metal cations (most of the time) coupled with redox reactions in the electrolyte compensating for electron loss and gain. By involving phase transformations and alloying reactions [2], the cyclability of the device worsens but the energy density is quite higher.

It is important to note that the same material can deliver pseudo-capacitive or faradaic behavior depending on how it is manufactured. Since it is an attention-worthy material, one should highlight that current variation during manganese oxide deposition can lead to one or the other kind of response [9, 10].

1.4.3 Types of SC based on electrode choice

Another distinction we can identify is between the electrode choice for a single device; there are three main cases, namely:

Symmetric device

In this case, the same active material (exploiting double layer capacitance) is used for both cathode and anode, this is the simplest choice but has limitation due to device's voltage window, that being generally not-symmetric (starting from the open circuit potential) could lead to a strong asymmetry in electrodes' masses to compensate for the reduced voltage swing on one of the two. That said, EDLC it's the most mature technology, generally cheaper and requires low maintenance. Their $E_{density}$ is low, with values reaching 5 $Whkg^{-1}$, while $P_{density}$ is around 9 $kWkg^{-1}$ [2].

Asymmetric device

Two different active materials with capacitive behavior are used for the two electrodes; beside the discomfort of having to characterize two materials in the same environment while ensuring compatibility, this configuration allows total voltage

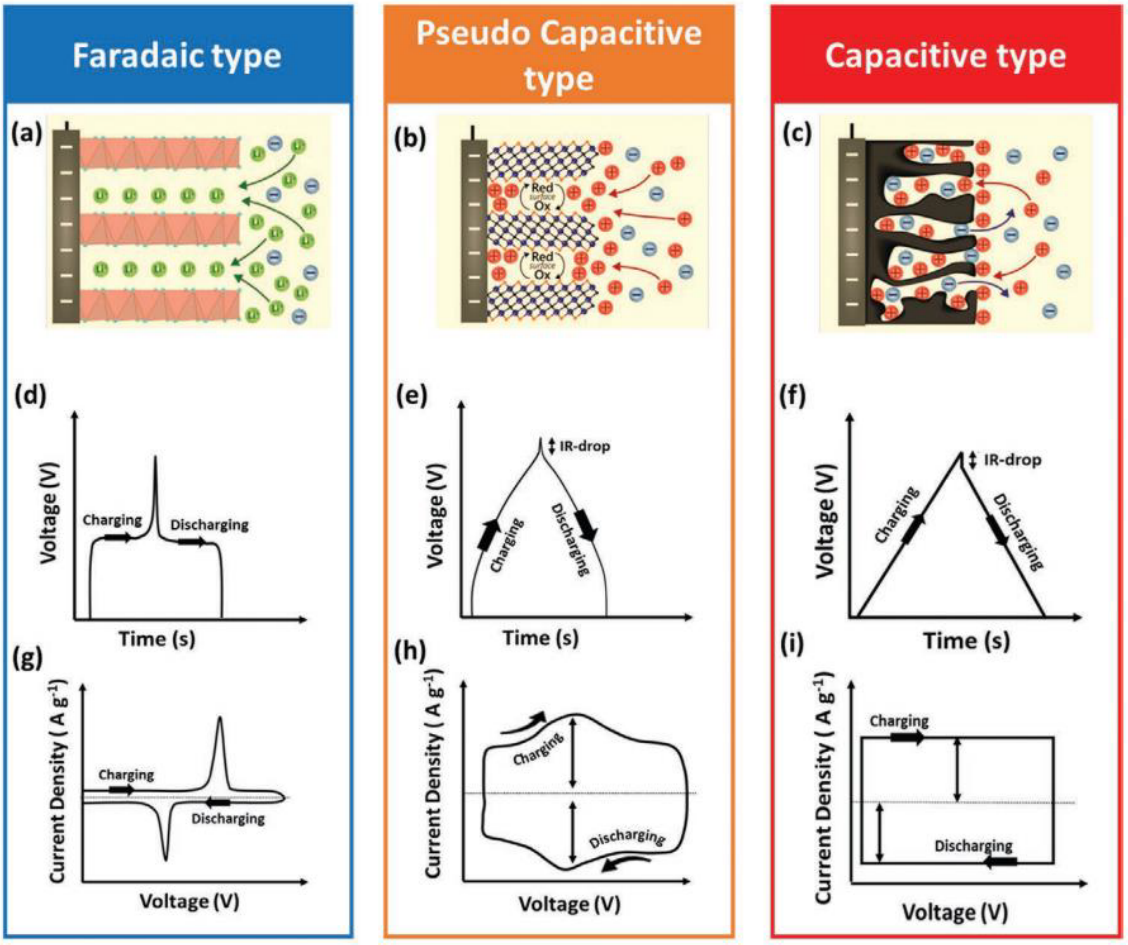

Figure 1.13: Energy storage mechanisms (a-c), Galvanostatic charge/discharge or GCD (d-f) and Cyclic voltammetries or CV (g-i) of supercapacitor technologies [28].

swings higher than the evolution voltage of the electrolyte in the final device [13]. This happens because different materials have distinct potential inside a stable pH environment when taken separately, and the two ΔV obtained are summed up when the device is assembled. This ensures weaker cyclability but better energy density. For example, 30.4 $Whkg^{-1}$ and 5 $kWkg^{-1}$ for a MnO_2 Nanowire/Graphene and Graphene Asymmetric SC were obtained [45].

Hybrid device

A faradaic and capacitive electrode are put together, producing one of the most promising technologies both in terms of power and energy density. This technology tries to take the best of both worlds, by fusing together the fast power delivery of an

EDLC with the steady energy release of a battery-like electrode. The combination of EDLC and faradaic mechanisms can maintain a voltage just high enough to stay above the threshold needed to power low-power electronic devices, even at low residual charge. A lot of research is ongoing regarding these devices, that also show good cyclability. Early results reach 100 $Whkg^{-1}$ and 4.5 $kWkg^{-1}$ [2].

1.4.4 Electrolytes for electrochemical SCs

Organic

Organic solvents like ACN (acetonitrile) or PC (propylene carbonate) coupled with salts (large ionic molecules) are used to achieve high voltage devices. Micropores ($\sim$ 1 nm diameter) are not suitable for large ion diffusion, thus lack of small pores is preferred in these applications. In fact, decomposition voltage of these solvents can be as high as 2.2-3 V, resulting in higher power and energy densities. The drawbacks of using such compounds include the complexity involved in assembling the device, as little to no humidity is allowed to prevent performance degradation. Additionally, there are safety concerns about ACN, which is currently known to be both toxic and flammable. Development of new and safer solvents is undergoing.

Aqueous

Water is often paired with small acid molecules hydroxides or sulfates to obtain a proper electrolyte. Given the dimension of ions, these time micropores are the go-to choice. While H_2O is a safe option, the salts dissolved inside of it can be harmful, therefore water-based electrolytes are not always the best solution. While having the benefit of not requiring particularly complex processing methods, dissociation voltage of water is around 1.23 V, resulting in significantly less power and energy density than organic solvents.

Ionic liquids

Room-temperature ionic liquids were initially seen as alternatives to aqueous electrolytes, but are now recognized as promising substitutes for solid electrolytes. They offer a wider operating voltage window than organic electrolytes, leading to higher energy density. Additionally, they are less toxic, have higher thermal stability, and lower volatility, which allows for higher operating temperatures.

1.4.5 SC parameters and non-idealities

Evaluation of SC performance comes mostly from a specific set of parameters that are going to be defined shortly; some of them are shared with electronic capacitors.

- C or C_s, *Capacitance/Specific capacitance*: main parameter that determines the ability of the device to hold charge.
- R_{ESR}, *Equivalent series resistance*: a simple but more correct electrical model of a SC includes a resistance connected in series to the ideal capacitor (drawn below), which models non-idealities of the device [50], and can be seen in **Fig. 1.13** whenever the I-R drop is highlighted in GCD techniques. Generally EDLCs have the lowest R_{ESR} out of all the SC technologies.

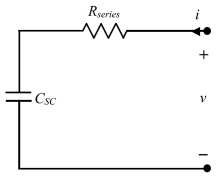

- V_{max}, *Maximum rated voltage*: the maximum voltage that can be applied at the two terminals of the device; usually the threshold is due to the evolution potential, that depends on the chosen electrolyte.
- I_{leak}, *Leakage current*: if left disconnected, SCs have a general tendency to self-discharge due to non-idealities. This phenomenon is measured through the leakage current, that is an indication of how fast the device loses accumulated charge on its own.
- η_{coul}, *Coulombic efficiency*: it's simply the ratio between the charge discharged by the SC to the total charge that was initially stored. An efficiency close to 100 % indicates minimal losses during charge/discharge cycle. Mathematically:

$$\eta_{coul} = \frac{Q_{discharge}}{Q_{charge}} \cdot 100\% \tag{1.7}$$

- η_{energy}, *Energetic efficiency*, or energy efficiency, refers to the ratio of the energy released during discharge to the energy supplied during charging. It provides a measure of how effectively the supercapacitor converts and retains the electrical energy supplied to it. It is typically lower or equal to coulombic efficiency because it accounts for both the charge retention and the voltage drop due to internal resistance (IR drop) and other energy losses within the supercapacitor.

$$\eta_{energy} = \frac{E_{discharge}}{E_{charge}} \cdot 100\% \tag{1.8}$$

1.5 Thesis objective

The objective of this work is to design an hybrid supercapacitor, exploiting carbon aerogel obtained from processing agricultural waste as its capacitive electrode, while employing a battery-like material based on Lithium ion intercalation as the faradaic electrode. Hybrid configuration has been chosen both for its potential as most flexible technology, and for the possibility of supplying energy to low-power devices, eventually coupling it with an adequately-sized solar cell for a battery-free, low maintenance system. In the future, the hope is to eventually power up small electrolyzers operating CO_2 reduction, thereby contributing to the development of sustainable energy solutions.

1.5.1 Choice of sustainable materials

The focal point of this work is to highlight sustainability of energy storage devices, therefore the choice of a lithium salt in combination with an aqueous electrolyte, that is non-flammable and environmentally benign, not to mention easily disposable, is both advantageous and necessary.
As a starting material for the carbon aerogel the choice fell onto rice husk, which is an abundant, inexpensive and biodegradable resource.
Finally, the faradaic electrode preference is dictated by cost and availability of elements. While the main constituents of current Lithium-based electrodes are cobalt, nichel and copper, the market is transitioning onto more environmentally friendly compounds, like magnesium, sodium, potassium and sulfur, which are naturally present in biomass and recyclable as well [19]. In light of these considerations, lithium manganese oxide ($LiMn_2O_4$) was ultimately selected, as it offers a balance of performance, cost-effectiveness, and reduced environmental impact.

1.5.2 Electrode production and characterization

The synthesis of the carbon aerogel was developed by P. Atanasio at Sapienza University in Rome, and will be explained in detail in the Materials and methods section. Both electrodes were constructed using a doctor blade coating method, which involves mixing the components forming the active compound in a liquid solvent, in order to be subsequently spread onto the current collector's surface. As mentioned above, the mixture is made of active material, binder and conductive agent; optimal weight percentage was found in literature and in an upcoming article of Polito's DISAT research group. The elctrodes thus made were then characterized in a 3-electrode configurationby means of standard investigation techniques for supercapacitors, such as Cyclic Voltammetry (CV), Galvanostatic Charge/Discharge (GCD) and Electrochemical Impedance Spectroscopy (EIS) which will be described

later.

1.5.3 Assembly of the final device and considerations

After all the characterizations, the device will then be assembled together and performances will be compared to evaluate possible improvements and feasibility of the device outside of a research laboratory. The SC will also be placed in the Ragone plot to be measured against other research and commercial products already available.

Chapter 2

Materials and methods

2.1 Instrumentation

2.1.1 3-electrode measurements

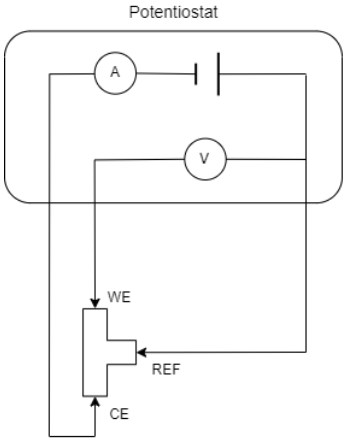

Figure 2.1: Schematic representation of a 3-electrode measurement using a potentiostat.

Most of the following measurements have been performed using the 3-electrode configuration. This kind of evaluation minimizes possible errors in performance and capacitance determination [50], isolating voltage and current control. As we can see in **Fig. 2.1**, the potential of the electrode under test or working electrode (WE) is referred to a stable reference (REF), which is usually a redox couple compatible with the electrolyte choice, guaranteeing a stable potential, also not influenced by operating conditions. A current is also applied between the working and counter

electrode (CE); the CE isn't easily polarizable and usually has high surface area while being chemically stable in direct contact with the electrolyte. For the experiments, Swagelok T-cells were utilized, which are depicted schematically in **Fig. 2.2**. These cells are very useful for what concerns repeatability of the tests, and they were used in combination with high surface area carbon electrodes as both reference and counter-electrode [32]. These are realized using a mixture of activated carbon, carbon black and polytetrafluoroethylene (PTFE), using ethanol as solvent. With heating and planetary stirring ethanol is slowly evaporated, promoting a dough-like consistency that is thinned by means of a rolling pin while still moist. Once a uniform thickness is achieved, 12–mm diameter disks are cut to fit the Swagelok cells, and left to dry in an oven. This approach resulted in a stable quasi-reference as well as poorly polarizable CE given its higher surface area w.r.t. electrodes under test. Finally, fiberglass is used as separator to keep the two electrodes from touching each other. It is noteworthy to say that a good amount of pressure between the two opposed metal contacts generally benefits the investigation, promoting performance and accuracy of the results.

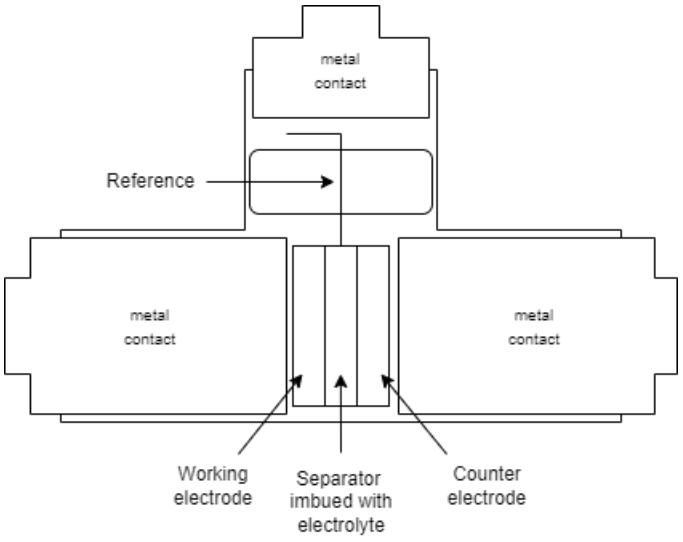

Figure 2.2: Visulization of the internal organization of a Swagelok cell.

2.1.2 BioLogic Potentiostat/Galvanostat VMP-3e

The BioLogic VMP-3e is the main workstation used in this work to conduct experiments. The main investigation techniques mentioned above have been mostly performed using this instrument (CV, GCD and EIS). Measurements allow for ± 1 A and modifiable voltage range of maximum ± 10 V; frequency measuements can go as high as 1 MHz. The possibility of having multiple channels is also very useful for

conducting many tests at once. The software managing all these operations is called EC-LAB.

2.1.3 MSK-SFM-3 Ball Miller

The High-Speed Vibrating Ball Mill (HSV-BM) MSK-SFM-3 is suitable for grinding and mixing a variety of materials, making it ideal for laboratory use when preparing ultra-fine powders and micro-sized materials. This equipment is highly efficient, compact, lightweight, and cost-effective. The mill is capable of grinding or mixing solid particles of various sizes and materials, as well as suspensions and pastes, using both dry and wet methods. In our case, the BM has been used to pulverize effectively the carbon aerogel, in order to produce a more homogeneously-sized particulate that would possibly yield a better slurry. It has been used with a milling tank with an inert gas atmosphere, in order to avoid oxidation of the carbon [42].

2.1.4 FESEM

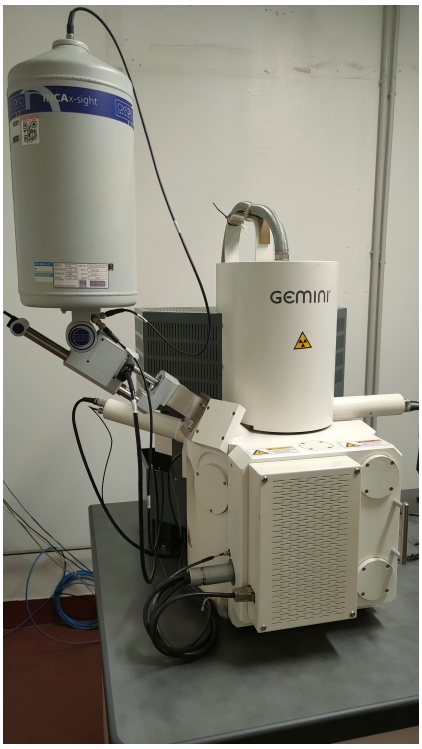

Figure 2.3: Politecnico's Field Emission Scanning Miscroscope.

The Field Emission Scanning Electron Microscope (FESEM) in **Fig. 2.3** is an advanced electron microscope capable of studying surfaces at resolutions down to the

nanometer scale. Unlike optical microscopes, FESEM uses electrons instead of photons, allowing for much higher resolution.
In FESEM, the material's surface is studied using high-energy electron beams with shorter wavelengths, which, according to Rayleigh's criterion, enable higher resolutions than optical microscopes. The electron source typically consists of an extremely sharp tungsten tip (with a diameter of 10^{-7} to 10^{-8} m), functioning as the cathode. It faces primary and secondary anodes, usually made of metallic grids. A potential difference between 0.5 and 40 kV is applied between the two. A high vacuum, around 10^{-8} Torr, is necessary inside the chamber to prevent any gas from ionizing and causing electrical discharges between the anode and cathode, while maintaining a long mean free path for the electrons.
Once emitted, the electron beam is shaped by the Lorentz force through magnetic fields generated by coils surrounding the beam or by electrostatic forces from charged plates. Each component has a specific purpose:

Condensing coils: These determine the thickness of the beam. A thinner beam correlates with better resolution but higher noise, while a thicker beam results in lower resolution but less noise.

Spherical aberration plates: These eliminate beam coalescence. They consist of two pairs of parallel metal plates, with the first pair aligned with the Z-axis and perpendicular to the X-axis, and the second pair also parallel to the Z-axis but perpendicular to the Y-axis. Adjusting the charge on these plates can widen or narrow the beam on the X or Y axes, achieving a perfectly circular cross-section.

Scanning coils: These deflect the beam across the sample, performing line-by-line scans to reconstruct the image. Faster scanning allows for real-time imaging but with less signal, resulting in higher noise and less sharp images.

Lenses: A series of lenses, composed of coils, focus and collimate the beam. The objective lens, the last one the beam passes through before hitting the sample, works at a short distance from the sample and focuses the beam onto it. A more focused beam provides a sharper image at the expense of depth of field.

When the beam strikes the sample, interactions between the material and the electrons in the beam lead to the emission of secondary electrons with various angles and energies. These hit a scintillator, whose signal is amplified and converted into an optical image on a screen.
For a sample to be suitable for FESEM analysis, it must possess several key characteristics. First, it must be sufficiently conductive to avoid charging under the

electron beam. If charging occurs, the accumulated negative charge would repel the beam electrons, distorting the image. To prevent this, a thin conductive metal layer (such as gold or platinum) is sometimes deposited on the sample to avoid charge accumulation. Secondly, the material must be able to withstand the vacuum of the chamber without contaminating it (e.g., by releasing gases or volatile substances) or deteriorating.
For the purposes of this work, the FESEM has been used to visually inspect samples and detect microscopic features and possible problems.

2.1.5 EDX Spectroscopy

Element detection using electron microscopy (EM), particularly through energy dispersive spectroscopy (EDS), is a technique often associated with Field Emission Scanning Electron Microscopy (FESEM). Despite its specialized nature, EDS remains somewhat underutilized in both diagnostic and research settings. This method allows for the identification and analysis of elements within a sample by detecting the X-rays emitted when the sample is bombarded with electrons.
Three primary methods are used in EM for element detection: wavelength dispersive spectroscopy (WDS), electron energy-loss spectroscopy (EELS), and energy dispersive spectroscopy (EDS), the latter being the most commonly used and often referred to as electron probe X-ray microanalysis (EDX).
EDX works by detecting the characteristic X-rays emitted from a sample after it is struck by an electron beam. When the electrons collide with the atoms in the sample, they can dislodge inner-shell electrons, causing the atoms to emit X-rays as they return to their ground state. These X-rays have energies that are specific to the elements from which they originate, allowing the EDX system to generate a spectrum that identifies the elements present in the sample and quantifies their abundance based on the peak size in the spectrum [34].
Despite its capabilities, EDX has several limitations. It cannot distinguish between ionic and nonionic species, and it requires samples to be analyzed under vacuum conditions, which can complicate specimen preparation. Additionally, X-ray spectrometry can be affected by inter-element interference, particularly peak overlap, which can complicate the analysis. EDX is most effective for detecting elements with atomic numbers greater than 10, with detection limits around 0.1 mmol/kg of dry specimen. The spatial resolution for this technique ranges from about 10 nanometers to a few micrometers. However, detection limits can be higher for heavy elements due to increased background noise.
EDX spectroscopy has been expolited in this work to analyze the elements composing certain samples, in particular evaluating the various phases of the aerogel synthesis.

2.1.6 Raman Spectroscopy

Raman spectroscopy is a technique named after physicist C. V. Raman, primarily used to identify vibrational characteristics of molecules, though it can also detect rotational and other low-frequency modes within systems. It is widely employed to provide a molecular "fingerprint," allowing for the identification of different substances. This method is based on the inelastic scattering of light, known as Raman scattering. A single wavelength of light, typically produced by a laser in the visible is directed at the sample, though X-rays can also be used. When the laser interacts with molecular vibrations or other excitations, the energy of the photons is altered, either increasing or decreasing. These energy shifts reveal details about the molecular vibrations present. Although similar information can be gathered through infrared spectroscopy, the two methods are often complementary. In practice, a sample is exposed to a laser beam, and the scattered light is collected by a lens and passed through a monochromator. The monochromator filters out elastically scattered light (Rayleigh scattering) at the laser wavelength using filters like a notch filter, edge pass filter, or band pass filter. The remaining scattered light is then analyzed by a detector, providing valuable information about the intensity and type of bond inside a compound. Nowadays it is possible to predict Raman spectra of crystalline structures, and the technique is particularly useful in the case of carbon based-materials because the G (1580 cm^{-1}) and D (1350 cm^{-1}) peaks can give information on crystalline quality and defects in the lattice, respectively. It was performed on our carbon aerogel before and after ball milling, to have graphical indications of changes.

2.2 Materials

The reagents utilized for the realization of our project are:

- Pulverized carbon aerogel, obtained from rice husk through various passages; which together with carbon black (C65), Hydroxypropyl cellulose (HPC) and deionized water (DIW) will compose the slurry that will be applied on the Titanium current collector. All these compounds will act as the negative electrode of the designed SC.
- Lithium Manganese Oxide ($LiMn_2O_4$), which will serve as the active material in a slurry similar to the one used for the negative electrode but with slight variations in the weight percentages of the components. This mixture will be applied as the positive electrode in the SC.
- An aqueous electrolyte, prepared using DIW with a specific salt. During experiments we tested multiple salts, including Potassium hydroxide (KOH),

Lithium hydroxide (LiOH) and Lithium sulfate (Li_2SO_4).

- YP-50F activated carbon powder mixed with ethanol, that acted as our quasi-reference and counter electrode in 3-electrode configuration testing. The counter electrode was contacted using a 12 mm diameter Titanium disk with 50 μm thickness. As reported above, glassfiber imbued with the selected electrolyte was interposed between WE and CE.

2.3 Aerogel synthesis

The following passages have been designed by P. Atanasio in his PhD thesis "Advanced carbon-based nanostructured materials for energy storage devices". They are reported in this work because they were performed in order to prepare the compounds for testing and assembly of the final device. Reagents utilized will be listed as the processes are explained.

2.3.1 Starting material and refinement

The starting material is rice husk (RH), which is composed mostly by cellulose ($\sim$ 38% wt), lignin ($\sim$ 22% wt), hemicellulose ($\sim$ 18% wt), silica ($\sim$ 20% wt) and other inorganic components. The raw material is grinded using a miller to produce a very fine dust. The obtained powder **Fig. 2.4** is volatile and a mask combined with careful handling is required during production and weigh. A total of 12.804 g of RH dust was obtained and subsequently processed.

Figure 2.4: Obtained RH powder weight.

Although other literature claims lignin carbon aerogels are manufacturable, it wasn't possible to exploit lignin as a carbon source in our case. The first phase of the

process therefore consists in the elimination of lignin (bleaching) and other organic components that we don't want in our final product.
In order to do this, a laboratory flask of 500 mL volume was used to mix and heat up a solution containing DIW with acetic acid (CH_3COOH) and sodium chlorite ($NaClO_2$) dissolved in it, together with the RH dust. The flask was chosen in order to leave enough space for vapours to leave the solution and react without causing too large pressure, while allowing the refrigerant on top of the flask to cool them and keep the reaction going.
The required volume of solution is calculated based on the total mass of the reactant, and is equal to 17 mL/g. Considering the starting mass, the calculated value was around 220 mL of solution, that are close to 220 g of DIW mass, given its density is $\sim$ 1 g/mL. That being said, the needed ratio between water and acetic acid has to be 3.36 g/L. Since this process has to be repeated 4 times in order to remove most of the lignin, 1 L of solution was prepared beforehand.
For what concerns the sodium chlorite proportion, it had to be 1.7% of the total mass of the solution, therefore:

$$220g : 98.3\% = NaClO_2|_g : 1.7\% \tag{2.1}$$

which resulted into a total of 3.805 g of sodium chlorite for every repetition of the process. Sodium chlorite is added everytime to the solution instead of preparing it beforehand because chlorine tends to reduce fast, losing reactability needed for the step. The solution is stirred until homogeneity is reached before usage.

Once the dust and the solution of DIW, CH_3COOH and $NaClO_2$ are in the flask, a way to heat up uniformly a curved glass has to be found. To solve the issue a bath of glycol was exploited, carefully positioned on a heating and stirring pad, as in **Fig. 2.5**. The choice fell on glycol because it has a boiling temperature higher than water, reaching higher temperatures without the risk of evaporation. To ensure a uniform reaction, a magnetic stirrer was placed in the glycol bath, and another was positioned in the flask to heat up the liquid effectively.
The flask is heated up to 80 °C and temperature is regulated using a controller that measures it directly inside the glycol and a mild stirring is utilized (500 for the pad in use). The whole process lasts one hour, and as already said, has to be repeated 3 to 4 times to be effective. Note how a cooling system utilizing water is also present at the top of the flask (**Fig. 2.6**).
In-between the iterations of this process, the solution contained by the flask is filtered using a micrometric filter, that separates the RH-derived compound from the solution which now contains the expelled lignin. Especially the first and second time, the process is really slow and requires a lot of time to be completed. The filter

Figure 2.5: The glycol bath and flask used in the setup, note the yellow-ish color of the solution, indicating chlorine reduction (process end).

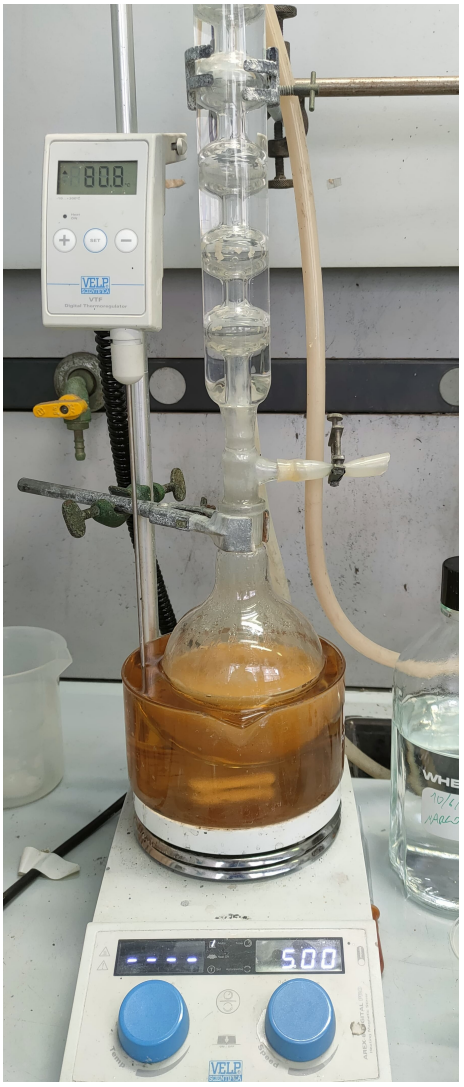

Figure 2.6: The heating and stirring setup used for lignin removal.

utilized is also made of paper, so that eventual scraping when retrieving the material does not result in contamination, but only more material processed (**Fig. 2.7**).

When the fourth iteration is completed, the resulting material is placed in an oven at 120 °C overnight to dry out, then weighed to determine the percentage of removed material. The remaining weight was found to be approximately 8.5 g. Based on the previous weight percentages, we can conclude that lignin and a significant portion of hemicellulose was removed.

Figure 2.7: Filtering setup with a cold trap.

Now we pass onto the removal of silica (SiO_2), which is a significant part of the starting material ($\sim 20\%$). This implies the usage of sodium hydroxide ($NaOH$) in a 1M solution with water; the process is carried out in the same setup, using 8 mL of solution per gram of sample. Although the process removes silica, it's important to note that the potential for utilizing both silica and carbon-based compounds has been already explored in literature, and could lead to a more efficient employment of RH as a sustainable resource [41].
Given the amount of material left, the necessary volume of solution is 68 mL, which have been prepared using a 100 mL volumetric flask to be more precise. Considering the molar mass of sodium hydroxide equal to $M_{NaOH} = 39.997$ g/mol, only 4 g of compound were needed.
For this instance the needed temperature is 102 °C, and while the setup and time of reaction remains identical, the starting time is measured from the moment reflux begins, which is the phenomen that occurs when water starts to evaporate from the solution, condenses due to the refrigerant, and is returned back into the solution. Difficulties were encountered in mixing the solution with a magnetic stirrer. The stirring parameter on the pad was increased significantly, ut led to minimal mixing, possibly due to an overall higher solution density.

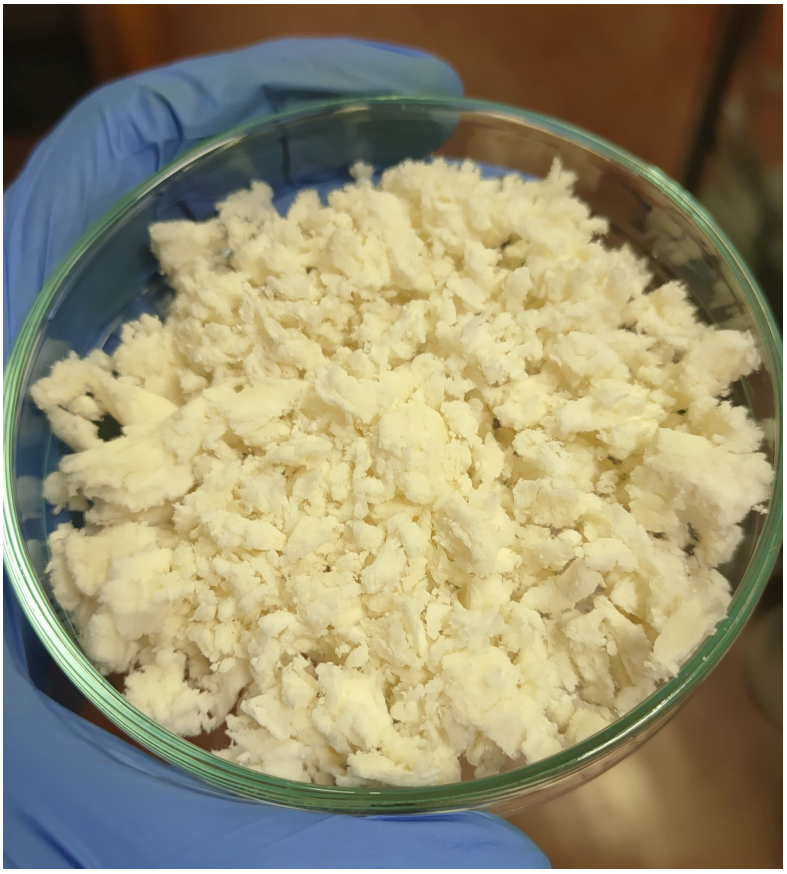

Figure 2.8: After refining RH dust, the cellulose appears noticeably whiter than before.

The final step before starting to process the refined material involves filtering the sample again to completely remove the sodium hydroxide. This process is labor-intensive, requiring continuous filtration with approximately 1 liter of distilled water until the filtrate achieves a neutral pH. It's important to note that distilled water has a pH around 5, not 7.
The sample is once again kept in an oven at 120 °C to dry out throughout the night. The resulting material is shown in **Fig. 2.8**, it's mostly cellulose and hemicellulose and was estimated to weigh around 5.17 g. Up until now, the process has taken up 3-4 days of work.

2.3.2 Gelification

The next step consist in the transformation of the cellulose thus obtained into a gel, a non-fluid colloidal network that is expanded throughout its volume by means of a

fluid, in this specific case a solution of urea and sodium hydroxide [25].
The needed percentage of reagents for the solution is:

7% NaOH 12.5% Urea 80% Deionized water

Considering 70 mL (70 g) of water, the needed quantities are 6.5625 g of sodium hydroxide and 10.9375 g of urea. The solution is stirred until homogeneity is reached; if not to be utilized immediately, it is wise to freeze it.
At this point we have to find a good container with a cyilindric bottom, since it is convenient to have the aerogel in the shape of a button. The choice fell onto 50 mL beakers, and in each of them was put an amount of cellulose equal to 0.6 g. Only 3.6 g of cellulose was processed in this way, but the process is scalable depending on application needs.

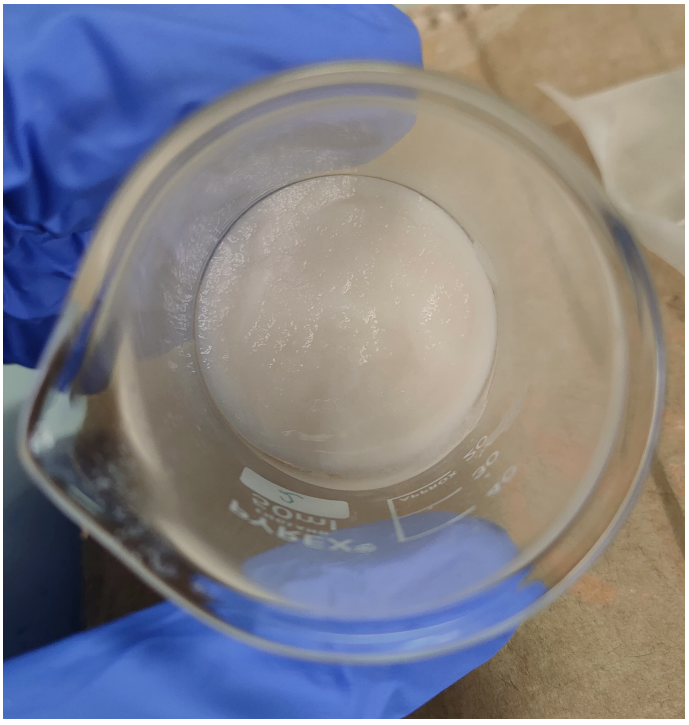

Figure 2.9: Appearance of the gel once formed inside the beaker.

During the procedure cellulose has to absorb the urea and NaOH solution at low temperatures to form the gel. Given that cellulose has to be 7% in weight of the total reagents in the beaker and the estimated density of the solution is 1.05 g/cm^3, 7.6 mL will be needed for every container. The beakers are positioned in a slightly deep tray containing ice, and put onto a stirring pad; each one of them has a magnetic stirrer inside to promote uniformity of gel formation. During this phase it is important that the temperature remains constant, and the melting ice has to be

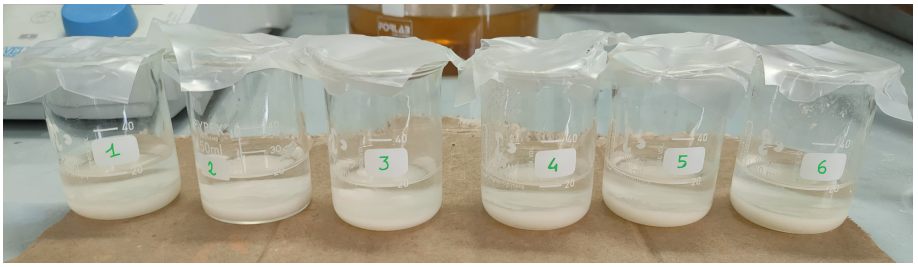

Figure 2.10: Water regeneration process.

eventually substituted. The whole routine lasts for a couple of hours, but usually some liquid is left at the end as well. To make sure saturation is reached, the tray is subsequently positioned in the glycol bath at 50 °C under a chemical hood for the night, to facilitate absorption or evaporation of the excess solution. The result is provided in **Fig. 2.9**.
The beakers containing the now well-formed gel have to undergo a process of regeneration, which consists in substituting the solution exploited to form the compound with DIW. This is why it's important to choose a glass container with much more volume than needed, allowing for faster exchange of $[OH^-]$ ions at least in the first few baths in deionized water. In fact, once the gel is considered dry, a certain amount of distilled water is added to each beaker (starting with approximately 35 mL, which will be gradually reduced). The water is changed every hour (initially even more frequently), taking care not to break down the gel or remove too much of it while changing the water that absorbed the ions with fresh water, until neutrality is reached (**Fig. 2.10**). This process corresponds ensures removal of sodium hydroxide from the sample, but additional washes are necessary to eliminate the remaining urea. To verify this, a conductivity test should be performed. The overall time needed for gelification of the cellulose is around 4-5 days.

2.3.3 Freeze-drying

Freeze-drying, also known as lyophilization, is one of the possible approaches, together with supercritical drying, when producing an aerogel. The starting material is the obtained gel, that has to be frozen beforehand (-50 °C); this solidifies the remaining water inside the sample. The frozen material is then placed in a vacuum chamber, where the pressure is reduced, and heat is applied. This causes the ice to sublimate, meaning it transitions directly from a solid state to a gas state without becoming liquid. While this happens, the vapor is removed from the chamber through a pump and a condenser 2.11.
Once enough time has passed and the procedure is finished, the final product retains much of its original shape avoiding possible collapses of the structure due to the

passage to the liquid phase that would normally happen, ending up with cellulose aerogel (**Fig. 2.12**), weighing a total of 2.84 g.

Figure 2.11: The chamber utilized to freeze-dry the samples.

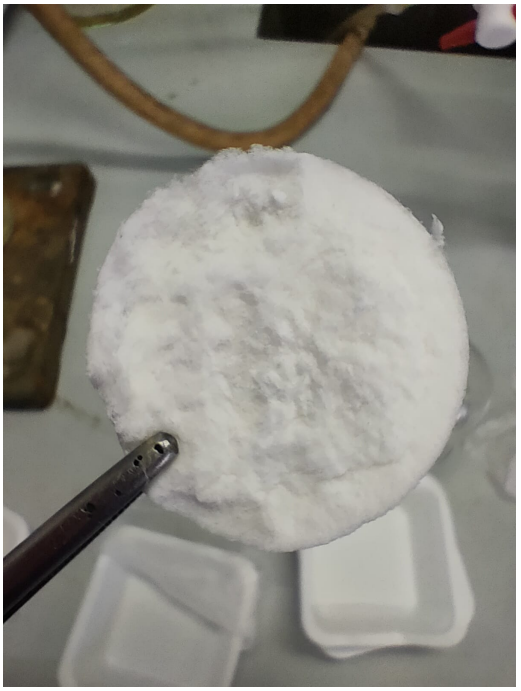

Figure 2.12: Cellulose aerogel appearance.

2.3.4 Pyrolisis

The last step in order to obtain the carbon aerogel is to heat up the cellulose up to 800 °C for a couple of hours continuously fluxing nitrogen to provide an inert atmosphere and expel possible byproducts. A cold trap has been utilized in this setup to prevent fumes from exiting and to control the flux of nitrogen as well. The oven for this purpose utilizes a thermocouple and a current controller to reach the desired temperature (**Fig. 2.13**). The final result of the whole process can be seen in **Fig. 2.14**, with a total mass of 432 mg.

Since three of the samples were not deformed that much, it was possible to evaluate shrinkage of the material after treatment in the oven, the values are reported in cm

Figure 2.13: The oven with the trays utilized to insert cellulose aerogel inside the tube.

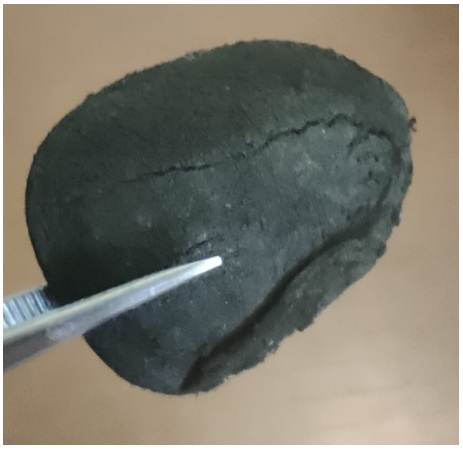

Figure 2.14: Carbon aerogel final appearance.

and are all listed in **Table 2.1**. Shrinkage percentage has been calculated using the formula:

$$\text{Shrinkage} = \frac{\text{Dimension} - \text{New dimension}}{\text{Dimension}} \cdot 100\% \tag{2.2}$$

2.3.5 Efficiency evaluation and investigations

To complete the study of the resulting carbon aerogel, the efficiency of the process was estimated by comparing the mass change during various phases. The process, as

Sample	Diameter	Height	New Diameter	New Height	Shrinkage
1	3.58	0.60	2.46	0.38	31.3%
2	3.55	0.43	2.59	0.32	27.0%
3	3.48	0.51	2.24	0.33	35.7%

Table 2.1: Comparison of sample dimensions before and after treatment, including the shrinkage factor.

it stands, has 5% of the total mass of the starting material transformed into carbon aerogel. Considering abundance and cheapness of the resource and the fact that silica can also be extracted from it, this is a well-received result.

In the following few pages, EDX spectroscopy and SEM images of the various phases of the procedure are reported. For what concerns EDX, on the x-axis we have the energy levels in keV, each peak corresponding to a specific element, with the position of the peak indicating the characteristic energy of X-rays emitted by that element. The y-axis shows the counts per second per electronvolt (cps/eV) instead. It measures the intensity of the X-ray signal at each energy level, which correlates to the abundance of the element in the sample. A table for each spectrum is also present, indicating quantitative data on the elements detected.
Note that chromium (Cr) detection in EDX spectra is due to the conductive coating applied to some of the samples to avoid image distortion caused by accumulation of charges of the non-conductive material analyzed. From the spectra in **Fig. 2.15** and **2.16** we notice the evident lack of silicon after its removal with sodium hydroxide, which confirms the effectiveness of the treatment. While not much changes between the latter and the spectrum after freeze-drying, the proportion of carbon in the last one has increased significantly, now making up 99% of the sample, indicating that it is the predominant element composing the final product (**Fig. 2.17** and **2.18**).
Last but not least, the change in surface area along with the formation of filaments due to the aerogel structure development is observable in **Fig 2.19, 2.20,2.21** and **2.22**. All of the images go from a 500x to a 50kx zoom.

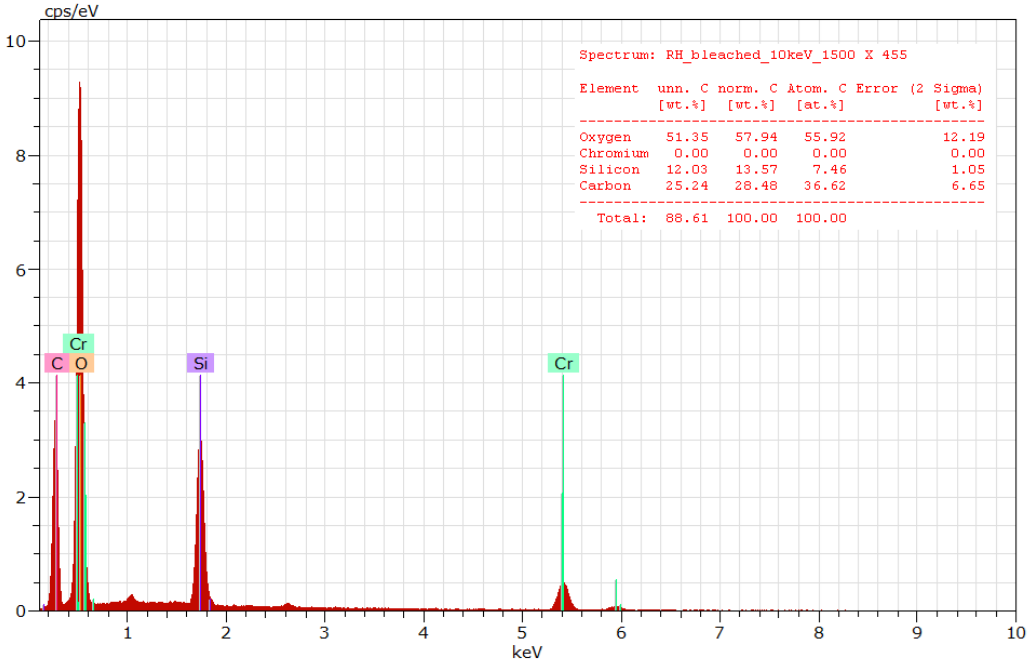

Figure 2.15: Spectrum of the sample after the treatment for lignin removal.

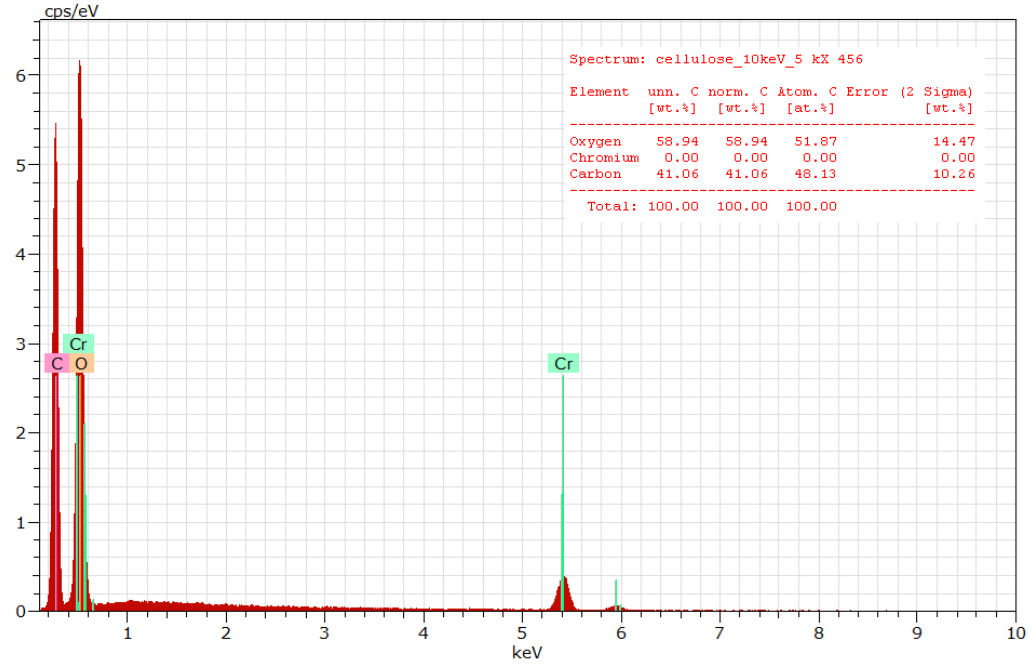

Figure 2.16: Spectrum of the sample after the treatment in NaOH.

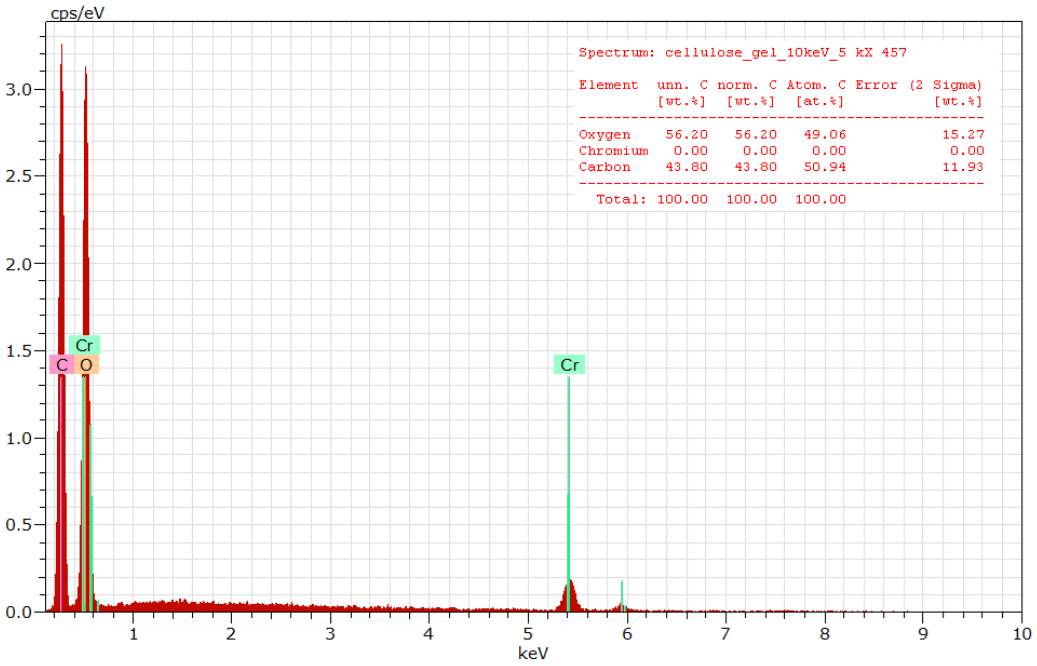

Figure 2.17: Spectrum of the freeze-dried gel.

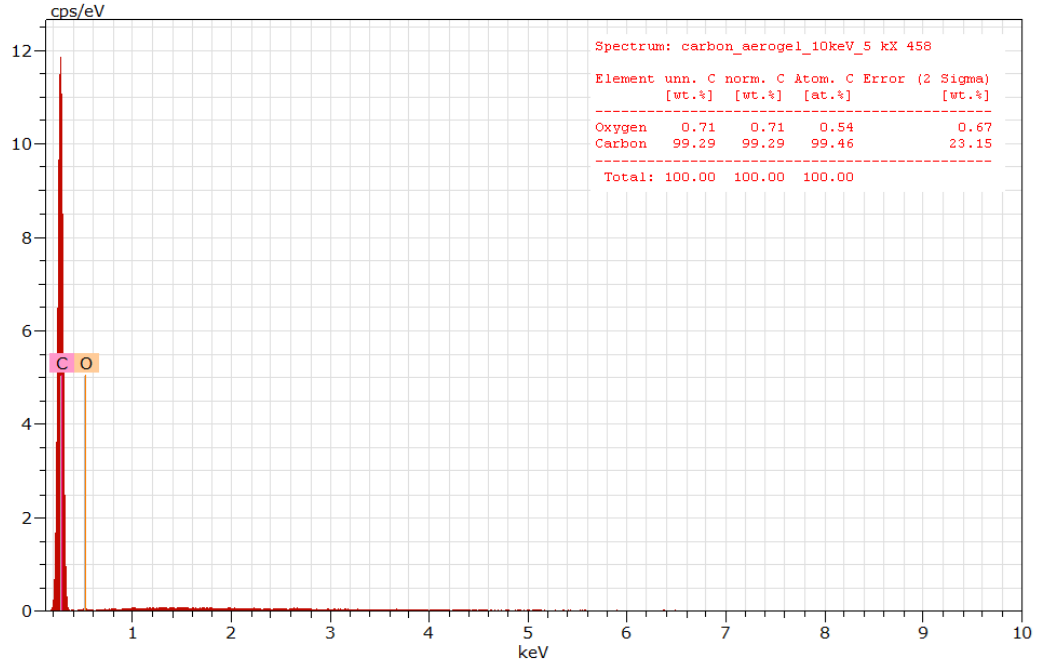

Figure 2.18: Spectrum of the final product.

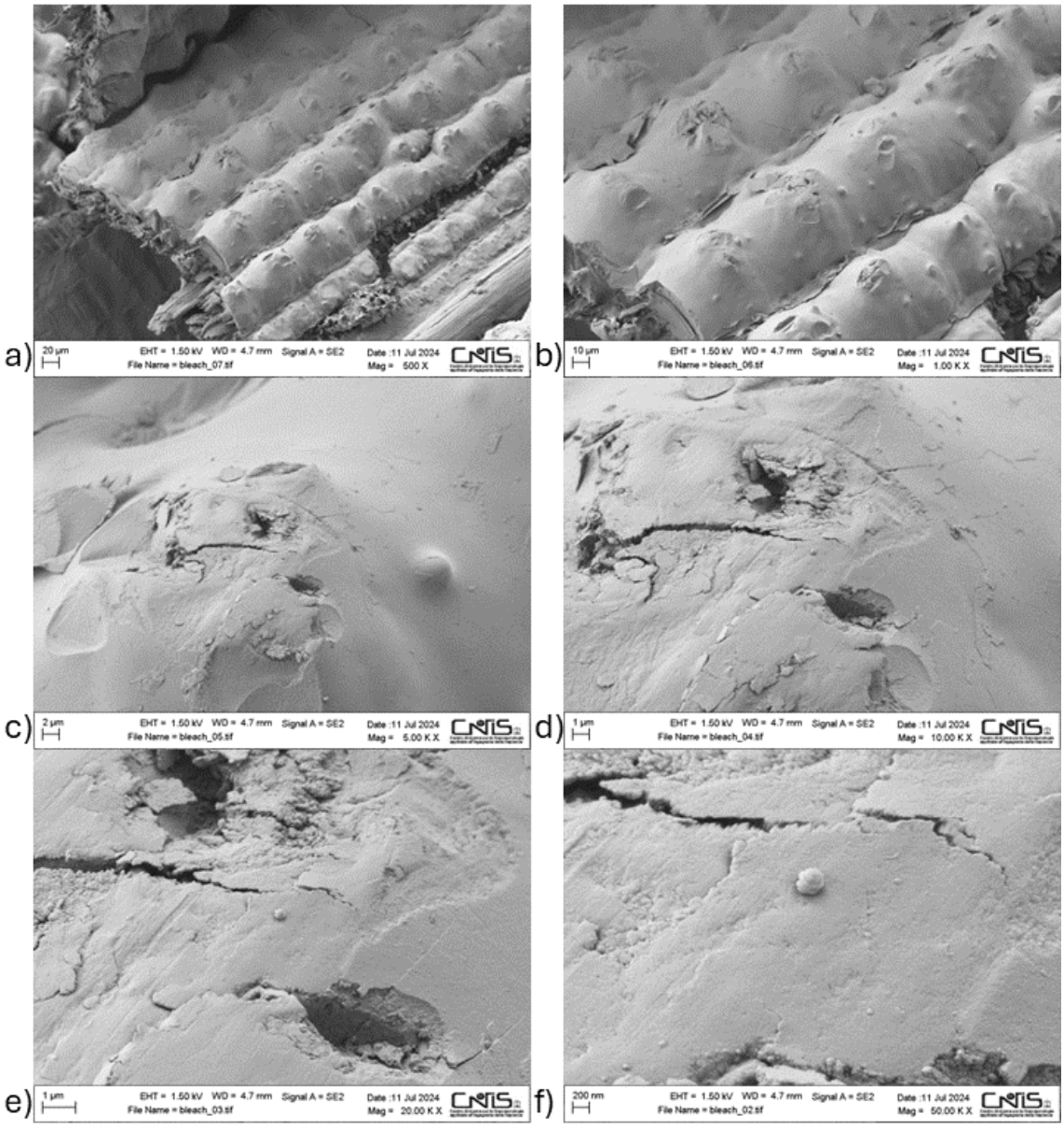

Figure 2.19: Various zooms of the bleached sample surface: (a) 500x (b) 1000x (c) 5kx (d) 10kx (e) 20kx (f) 50kx.

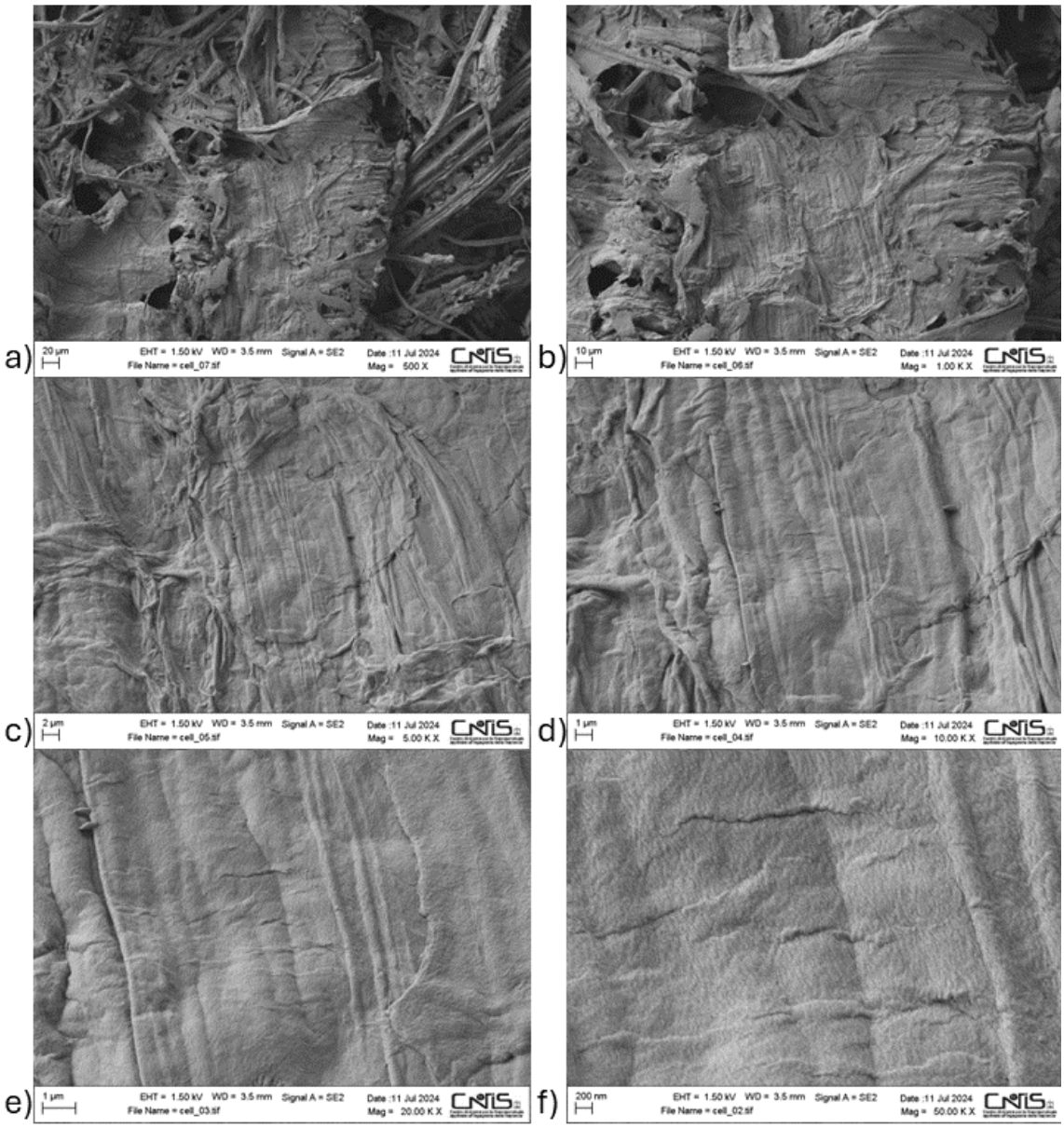

Figure 2.20: Various zooms of the refined cellulose: (a) 500x (b) 1000x (c) 5kx (d) 10kx (e) 20kx (f) 50kx.

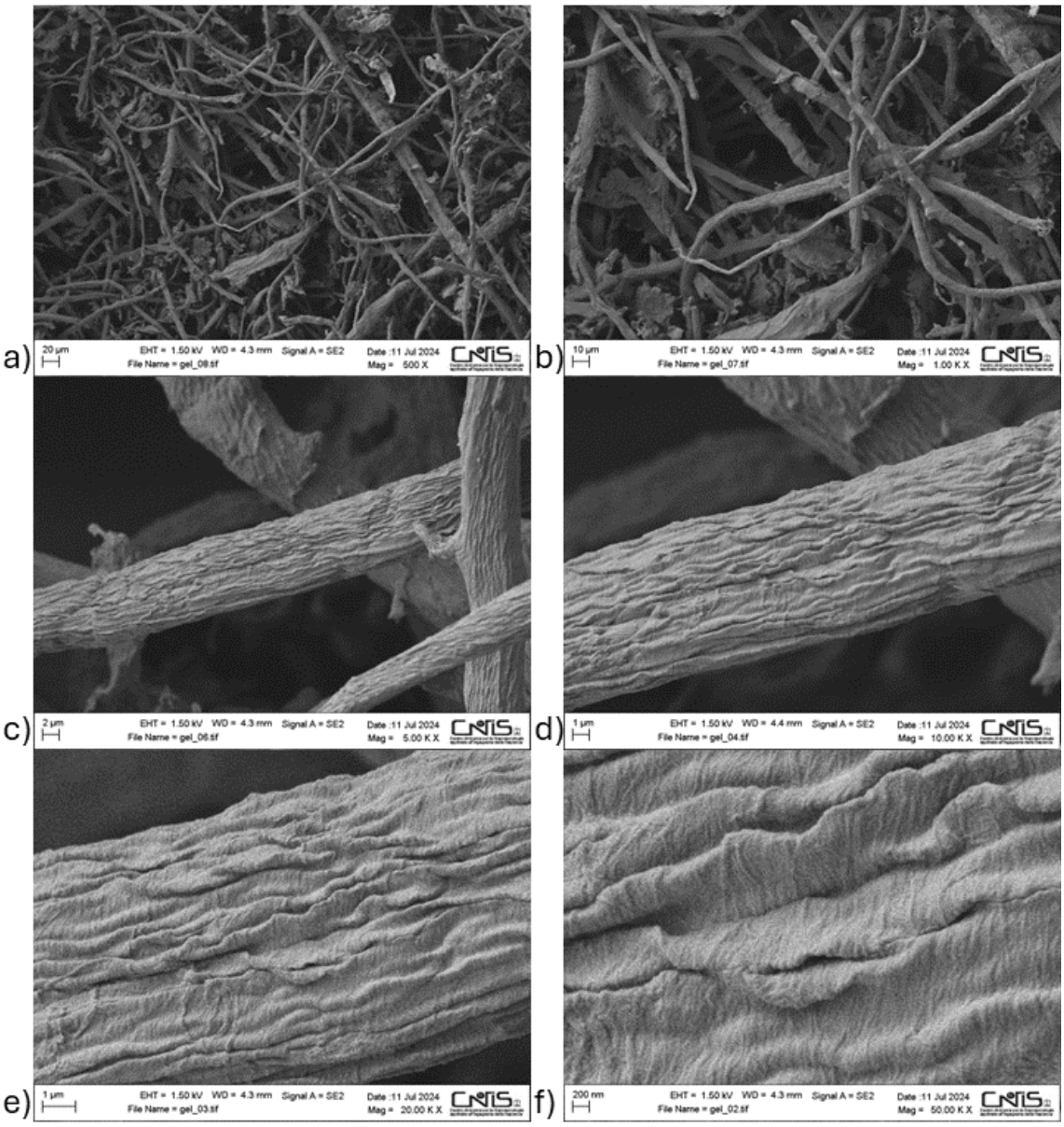

Figure 2.21: Various zooms of the cellulose aerogel: (a) 500x (b) 1000x (c) 5kx (d) 10kx (e) 20kx (f) 50kx.

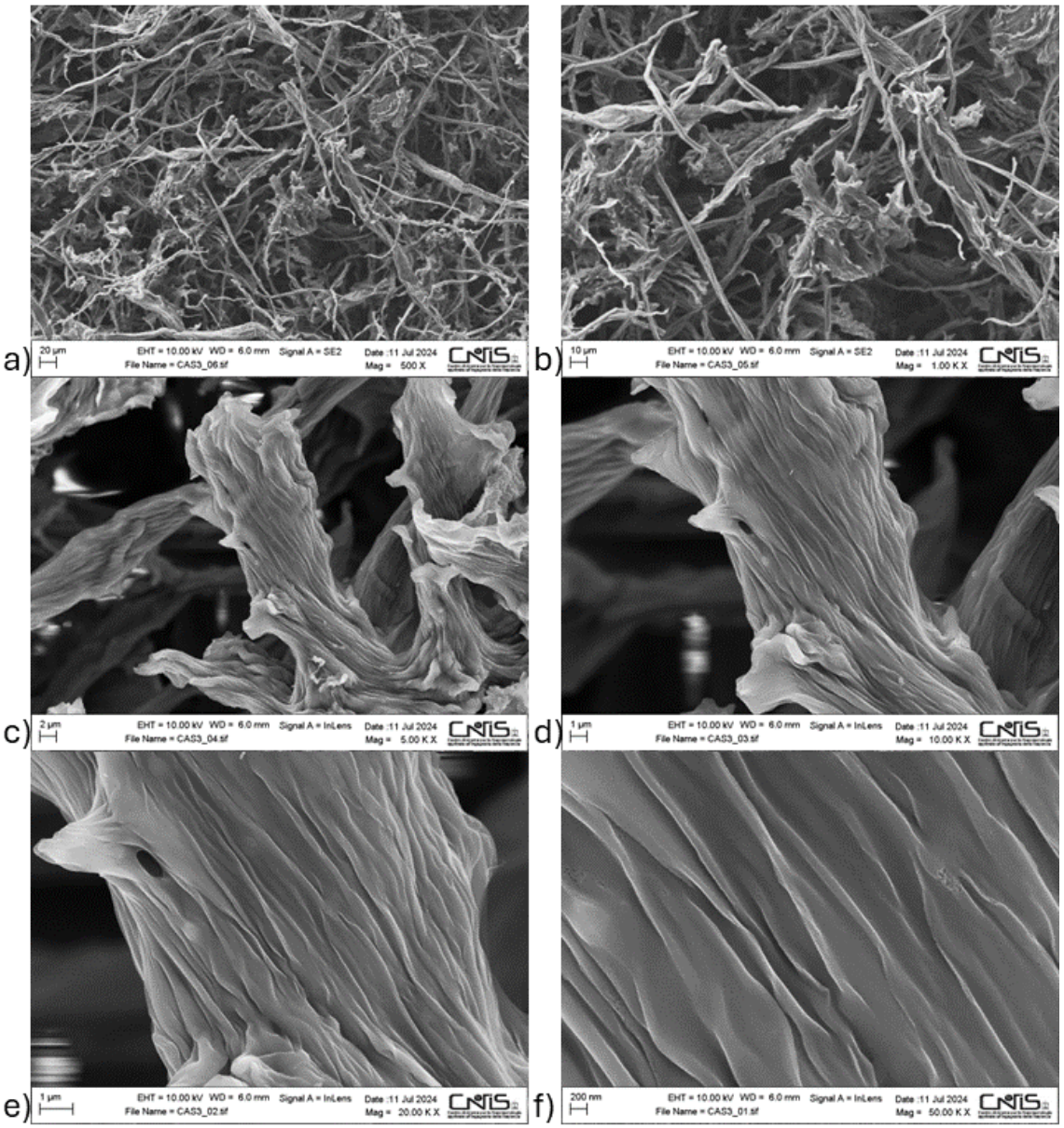

Figure 2.22: Various zooms of the final carbon aerogel: (a) 500x (b) 1000x (c) 5kx (d) 10kx (e) 20kx (f) 50kx.

2.4 Slurry preparation

Now to pass to the preparation of the slurries that will form the electrodes of the final device. The procedure consists in mixing the components gradually and in a specific order. A bunch of slurries were made for testing and reference, and different binders were exploited to create them, like PVDF and HPC. The procedure is substantially the same, the only thing that seems to vary is the time needed to reach a satisfactory homogeneity of the liquid-like substance.
To prepare the slurry, the needed equipment is a stirring pad, a stirrer and a glass container. The solvent for the liquid phase depends on the type of binder, this work utilized Dimethyl Sulfoxide (DMSO) for PVDF and deionized water for HPC. While in literature the most used solvent for PVDF is N-methyl-2-pyrrolidone (NMP) [37], because of its toxicity and the fact that it is easily absorbed into the body through topical contact and by inhalation, not to mention that the European Chemical Agency has classified it under the Substances of Very High Concern (SVHC); the choice fell onto a more environment-friendly substitute.
The conventional electrodes employing DMSO were prepared using activated carbon YP-50F, C65 carbon black and PVDF with a standard mass ratio of 80:10:10 [27]. For the HPC electrodes, we have to distuinguish between EDLC and faradaic. For those exploiting highly porous carbon the mixture was optimized using a mass ratio for active material (either YP-50F or crushed carbon aerogel), C65 carbon black and HPC of 85:10:5. For the $LiMn_2O_4$ electrode instead, the ratio was modified to 70:25:5. Solvent addition is based on its ability to break down the binder properly instead; tipically 1 mL of DMSO is able to dissolve 20 mg of PVDF, while 1 mL of of DIW dissolves 10 mg of HPC.
To begin the mixture preparation, the solvent is added to the container, and as it is slowly stirred on the pad, the binder is gradually incorporated. The stirring speed is increased and after a while the solute is not visible anymore, so C65 is added to the solution, again slowing down to increase stirring speed later. When the liquid is mostly homogeneous, the active material is finally added. The result of the process is shown in **Fig. 2.25**. Normally, at least 500 mg of total reagents (solvent not included) compose the slurry, allowing for easy handling and higher tolerance for human error.
Once prepared, the slurry is used to coat a current collector, an adequately cut 50 μm-thick Titanium foil **Fig. 2.23**. This is done exploiting doctor blade technique: a flat, adjustable blade is positioned above the substrate; the liquid material is deposited in front of the blade and as the blade is moved across the surface, it spreads the liquid evenly, leaving a uniform layer behind. Since a circular shape for the Swagelok t-cells is desirable, an adesive mask is used on top of the Titanium, which is held in place on a microscope slide for easier handling **Fig. 2.24**. The thickness is therefore controlled by the adesive tape, which was used in a double configuration,

adding up to more or less 120 μm (60 μm per layer of tape). To finish the procedure, the electrode is left under a chemical hood, where the solvent evaporates, and the mixture loses its liquid phase.
To make sure the slurry stuck to the Titanium, the surface was polished beforehand to make it rough and promote adhesion. One final important point to mention is that solvent tends to evaporate from the slurry unless hermetically sealed; this meant that older mixtures were able to achieve higher mass loading on later-developed electrodes, which opened discussion for surface-to-volume ratio difference between small and big masses.

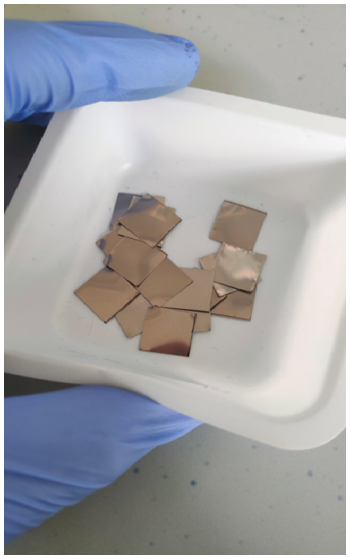

Figure 2.23: Ti current collectors used for electrode characterization.

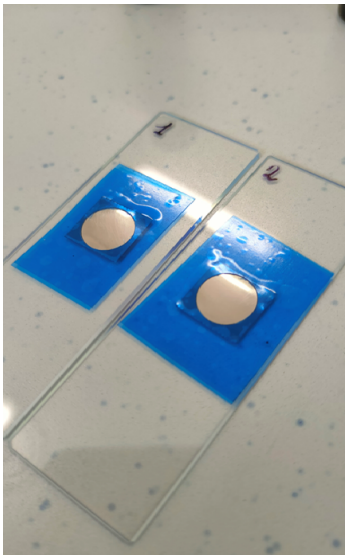

Figure 2.24: Masking of the Titanium before coating.

Figure 2.25: Slurry appearance in its glass container.

2.5 Characterization methods

2.5.1 Cyclic Voltammetry (CV)

Cyclic voltammetry (CV) is a widely-used and versatile technique in electrochemistry, useful for analyzing electron transfer processes within electrochemical systems. In the context of supercapacitors (SCs), it helps evaluating ion dynamics at the electrode/electrolyte interface, measuring capacitance, determining the appropriate electrochemical stability window (ESW), and identifying faradaic reactions. During CV, a linear voltage sweep is applied between the reference and working electrodes,

and the resulting current is recorded over a fixed a potential range that can be either fixed or changing, depending on the needed investigation. The resulting plot offers valuable insights into reactivity and mass transport behavior in response to the applied voltage.
The ΔV is adjusted at a defined scan rate, changing current intensity flowing from counter to working electrode depending on speed. By considering measurement parameters like voltage limits and scan rate, and by graphically integrating the area under the curve (i.e., the area of the voltammogram), the specific capacitance can be calculated using the following equation [16]:

$$C_s = \frac{\int_{V_1}^{V_2} i \, dU}{\nu \, \Delta U \, m} \tag{2.3}$$

In this equation, i represents the current, $\Delta U = (V_2 - V_1)$ denotes the potential window defining the integral, ν is the scan rate, ΔU is the ESW, and m is the mass of the active electrode material.

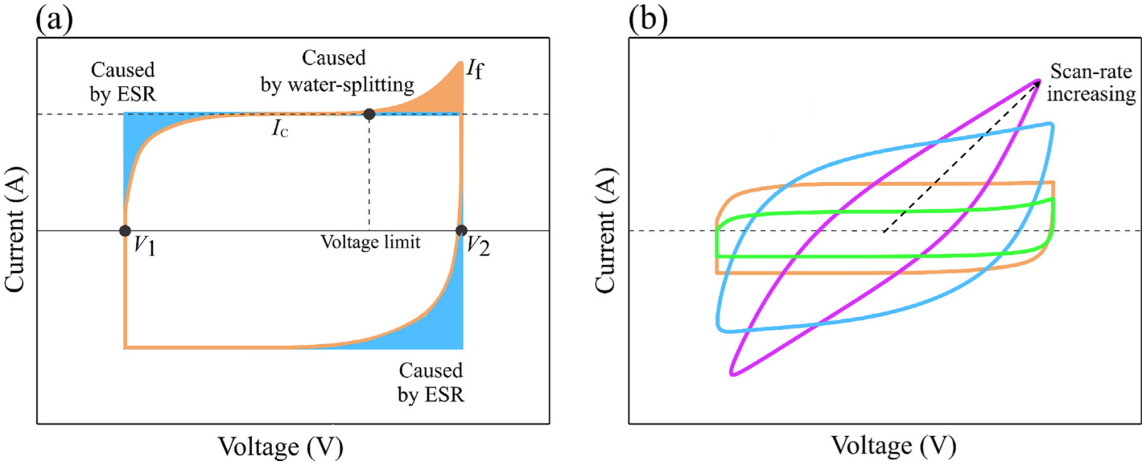

Figure 2.26: (a) Theoretical profile of a CV curve highlighting the specific contributions. (b) CV curves at various scan rates to illustrate the variations in shape. [16]

Eq. 2.3 allows us to observe the influence of scan rate on capacitance. High scan rates can significantly impact the capacitance by excluding redox processes, leaving only the capacitive charge-storage mechanism. Conversely, when the scan rate is close to zero, the time constant due to interface phenomena ($\tau = RC$) becomes more favorable for faradaic processes, allowing for the observation of both faradaic and capacitive mechanisms in the overall electrochemical process.
For supercapacitors, the CV curve typically exhibits a quasi-rectangular current vs.

voltage profile. Theoretically, using an RC model, the capacitive current (I_C) from the CV profile shown in **Fig. 2.26(a)** can be described by the following equation [16]:

$$I_C = C_{EDL}\nu\left(1 - \exp\left(\frac{-\Delta U}{R_{ESR}C_{EDL}\nu}\right)\right) \tag{2.4}$$

Here, R_{ESR} is the equivalent series resistance, and C_{EDL} represents the electrical double-layer capacitance. It is also worth mentioning that when the system undergoes irreversible faradaic reactions (such as water splitting) the I-V curve changes. This is normal in the first cycles of any SC, especially at slow scan rates. In fact, after assembly the porous structure has yet to be permeated by the electrolyte, and faradaic side reactions happen as well, limiting the coulombic and energetic efficiency of the electrode/device. The example reported in **Fig. 2.27** shows the increase in η_{coul} during multiple cycles at low scan rates in the same voltage window, revealing the phenomena just described.

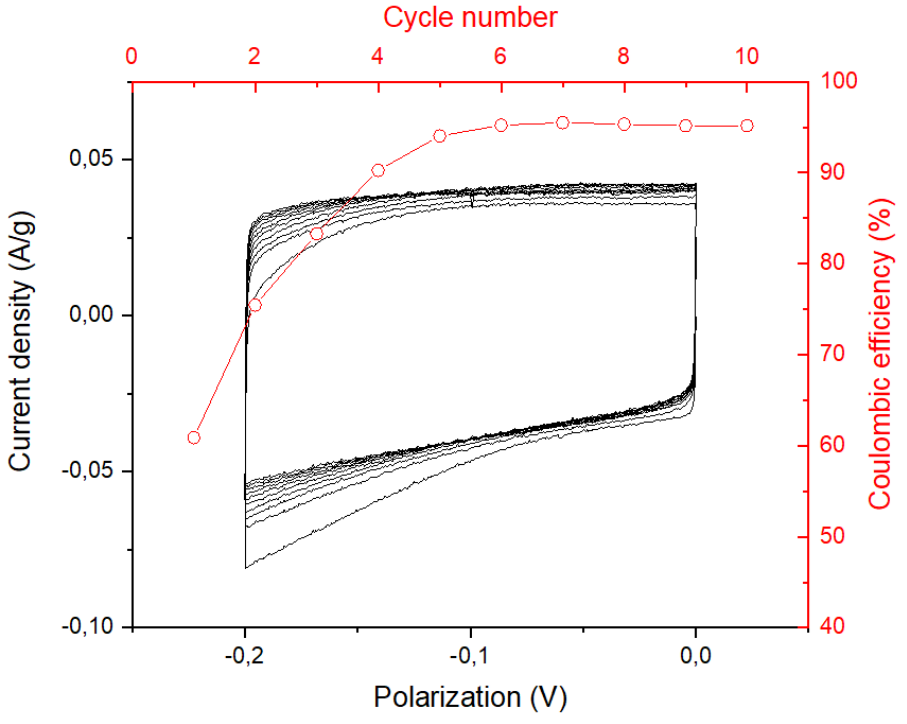

Figure 2.27: An enhancement of the effects of faradaic side reactions happening in the first cycles at slow scan rates.

As we can see from **Fig. 2.26(a)**, non-idealities in the device change its shape,

subtracting charge (ESR) or utilizing additional energy for electrolyte dissociation. The scan rate impacts the curve as well: being an RC circuit, the faster the signal, the harder for the capacitor to react and charge in time (seen also how big it is), revealing a curve that tends to a plain resistor characteristic.

Electrochemical stability window (ESW)

This is perhaps the first test to evaluate performance of an electrode/device. In this investigation, coulombic efficiency is evaluated to determine the maximum voltage difference in which the device is able to work. In this way, we can determine the maximum voltage rating of the SC to avoid early failure and allow maximum cyclability. The generally accepted minimum efficiency while functioning is 98%, but it can be lower depending on scan rate.

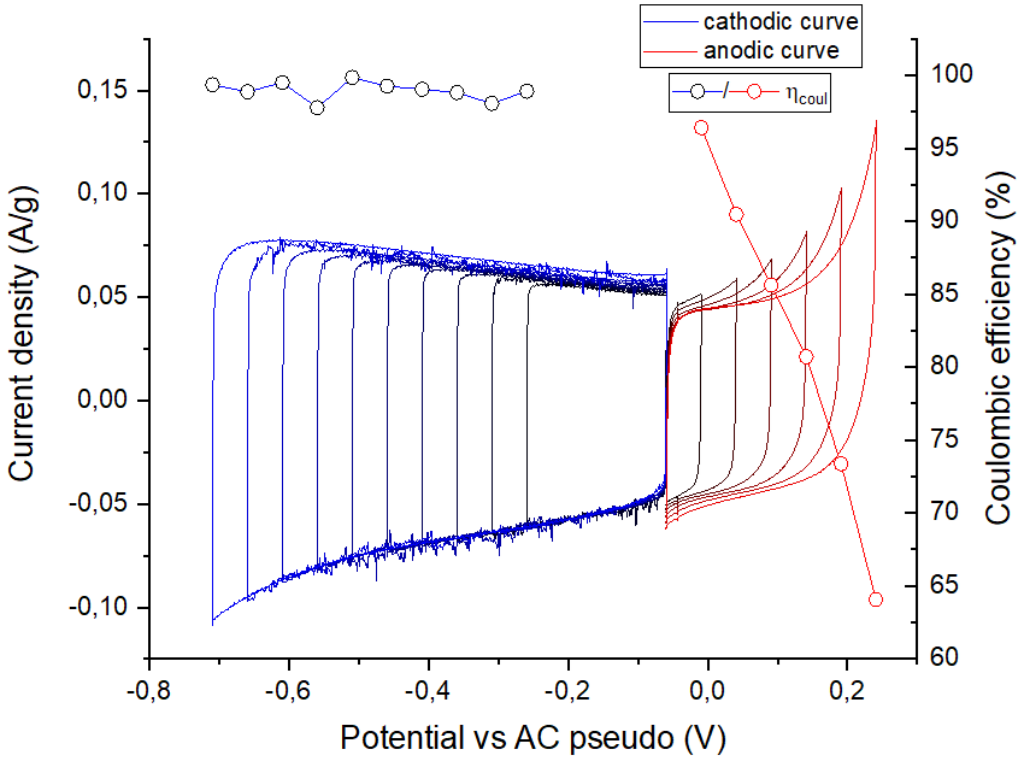

Figure 2.28: The electrochemical stability window search using CV. The scan rate used was 1mV/s, which is considered low enough to allow for faradaic reactions to happen.

After assembly,the device is left floating for a while, until electrochemical equilibrium is reached and the working electrode approaches a stable potential vs reference. This

voltage is called open circuit potential (OCP) and it is a condition that has to be achieved before the execution of any test. The experiment starts at the OCP and an anodic and cathodic scan are performed; for the anodic scan an higher and higher positive potential is applied, and viceversa for the cathodic one. Depending on settings it may be wise to prepare two different electrodes to test for anodic and cathodic scan, since device performance could be altered if irreversible reactions have already taken place.
An example can be seen in **Fig. 2.28**, where an activated carbon powder (similar to carbon aerogel) mixed with PVDF and C65 was tested in basic environment (KOH 1M aqueous electrolyte) to see why carbon-based electrod are mostly used as negative electrodes, and also to set a reference for how the carbon aerogel electrode should work. Notice how the anodic efficiency curve goes towards low values very fast, indicating irreversible reaction (oxygen evolution) happening; a tell-tale sign is also the increasingly higher peaks of current, which do not have a correspondent one while discharging. Since it was just a fast test, the cathodic limit was not reached, but the point about porous carbon structures in basic environments was already proven.

Rate Capability test

CV can be also utilized for cyclability tests, while determining capacitance change at higher scan rates. With a fixed ESW, multiple CVs are executed at several scan rates; the different curves appear much like the ones in **Fig. 2.26(b)**. The same device mentioned above has been tested in this way for an arbitrary $\Delta V = 0.5$ V and the results are shown in **Fig. 2.29**. The higher the scan rate, the more challenging it becomes for the device to fully charge, and most of the power will be dissipated by the ESR, lowering η_{coul}.

2.5.2 Galvanostatic Charge/Discharge (GCD)

GCD is a transient technique that complements the CV in its ability to determine parameters for SCs, such as energy storage capacity, ESR, equivalent distributed resistance (EDR), cycling stability, rate capability, and coulombic efficiency. In GCD analysis, a constant current is applied during both the charging and discharging phases while monitoring the voltage. Ideally, the capacitance remains stable over time and is solely dependent on the applied potential. Under these conditions, the charge and discharge profiles appear linear, and the voltage across the supercapacitor (U_{SC}) can be described by:

$$U_{SC} = \frac{t \cdot i}{C} \tag{2.5}$$

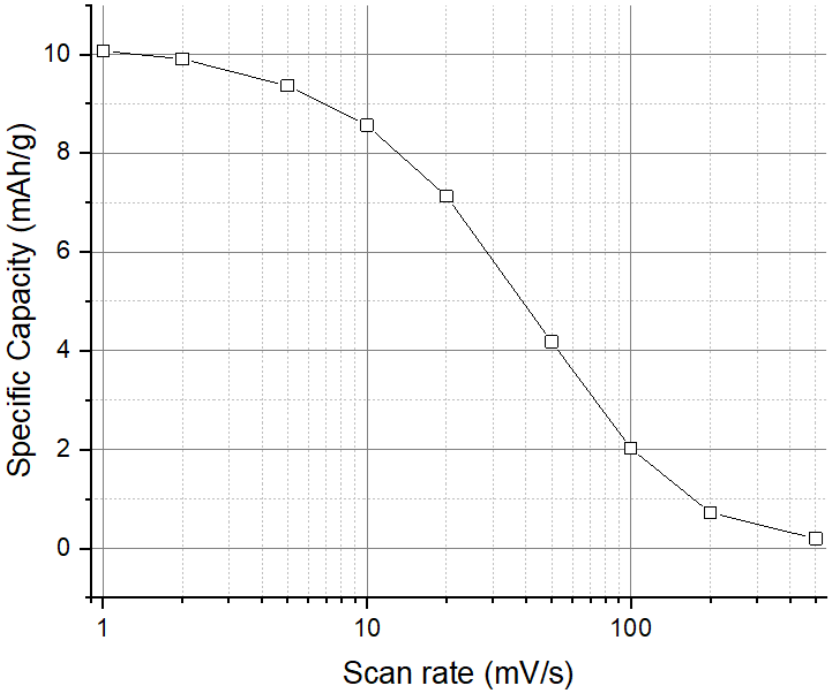

Figure 2.29: Specific capacity change at different scan rates, the values were checked using different methods, giving the same result.

However, in supercapacitors, the response may be non-linear depending on the charge storage mechanisms, a deviation observable in pseudocapacitors and hybrid systems. Besides the charge storage mechanisms, the GCD profile is also influenced by the applied current. At high current densities, faradaic processes are reduced due to insufficient time for mass transport, leading to ion storage predominantly at the electrical double layer (EDL), resulting in a nearly linear profile even in pseudocapacitive device. Similar to low scan rates in CV, GCD profile at low current densities will reflect the combination of electrochemical processes occurring in the device [16].
The capacitance of the SC can be accurately determined from the GCD curve. For an SC where charge storage occurs only at the EDL, the capacitance can be expressed as:

$$C = \frac{i \cdot \Delta t}{\Delta U} \tag{2.6}$$

where Δt is the time interval for discharging, and ΔU is the voltage change after subtracting the initial voltage drop observed at the beginning of the discharge curve

from the ESW (as shown in **Fig. 2.30(a)**). For GCD measurements resulting in non-linear curves, capacitance can be calculated by integrating the area under the discharge profile using the equation:

$$C = \frac{q}{U_{SC}} = \frac{2i \int U\, dt}{\Delta U^2} \tag{2.7}$$

The initial voltage drop observed at the start of the discharge in GCD plots corresponds to the contributions from ESR (including electrolyte resistance, cable resistance, and electrode resistance) and EDR (representing ion resistance in accessing the 'outer' pores of the electrode) [16]. The difference between these resistances is graphically illustrated in **Fig. 2.30(a)**. The ESR and EDR can be calculated using the following equations, respectively:

$$R_{ESR} = \frac{\Delta U_{ESR}}{2i} \tag{2.8}$$

$$R_{EDR} = \frac{\Delta U_{EDR}}{2i} \tag{2.9}$$

where ΔU_{ESR} and ΔU_{EDR} are the voltage drops caused by ESR and EDR during the discharge in the GCD curve, respectively. As depicted in **Fig. 2.30(b)**, increasing the applied current leads to a greater voltage drop.

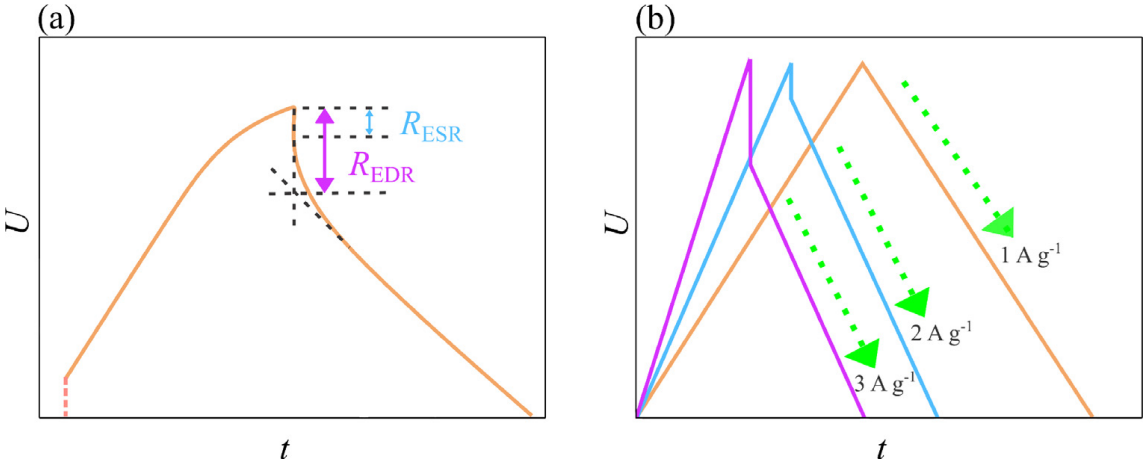

Figure 2.30: (a) Parameters of the galvanostatic curve used to determine the ESR and EDR. (b) GCD profiles with different gravimetric currents. [16]

Usually the constant current exploited for charging and discharging the device can be chosen with two criteria: either the gravimetric one, in which the current depends on

the electrode mass loading, or using C-rates (especially useful for pseudo-capacitive and faradaic electrodes). These are currents that theoretically charge the device in a specific period of time. The C rate corresponds to full charge in one hour, 2C in half an hour, while C/2 means a two hour charge. These rates exploit the theoretical capacity of the material, and it's therefore only an estimation of charge time. They can be calculated following Faraday's law of electrolysis [6]:

$$QM = mFz \tag{2.10}$$

where Q is the charge , M and m are the molar mass and the mass of the chosen compound, respectively; z is the number of electrons involved in the reaction, and F is Faraday's constant.

Capacitance retention (cyclability test)

A very long CGD can be performed to test the capacitance retention of the device. This experiment consists in charging and discharging the device at a current rate that exploits its full capacity thousands of times, to see how well it is able to keep its characteristics after prolonged use. An example is provided in **Fig. 2.31**.

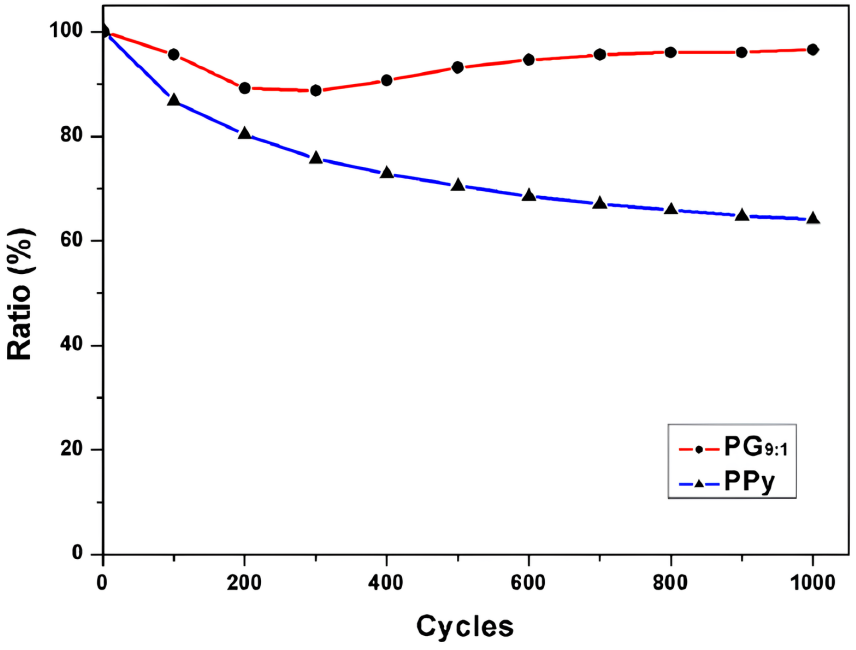

Figure 2.31: In this example the retention ratio of two different electrodes are reported, from the 1st to the 1000th cycle.[48]

One crucial factor to consider is the duration for which the device remains at its maximum voltage rating. This condition is particularly stressful for the device and is where the likelihood of irreversible reactions is highest.

2.5.3 Electrochemical Impedance Spectroscopy (EIS)

EIS is a non-invasive technique aimed at discriminating electrochemical, electrical and physical processes taking place in a system. This is especially useful when different phenomena possess time constants far apart one from the other, as it becomes easier to pinpoint and interpret the various parts of the resulting plot.
The test itself consists in a sinusoidal perturbation around the point of equilibrium of the system (OCP), either by applying an AC voltage (potentiostatic, PEIS) or an AC current (galvanostatic, GEIS) while simultaneously measuring the device response in current or voltage, respectively. The perturbation is applied in a wide range of frequencies, usually spacing from 1 mHz to 1 MHz. The measured response is translated into impedance data, meaning real and imaginary parts are evaluated for each frequency separately. Notably, EIS can lead to an equivalent electrical circuit of the device under test, consisting of passive components and distributed elements. The extracted data is evaluated through three different graphs: the magnitude and phase Bode plots and the Nyquist plot; starting from these, and through the use of a specialized software, an equivalent circuit model can be created.
A deep knowledge of the system under investigation is required to fully comprehend the insights that EIS can provide; to establish a foundation, the responses of the simplest circuital elements are presented in **Fig. 2.32**. When the circuit under test (CUT) contains only a resistor, the Nyquist plot shows a point on the real axis, the magnitude Bode plot is constant and equal to the value of R1, and the phase plot is constant as well and equal to zero, since no imaginary part is present.
When the CUT is only a capacitor, the real impedance is equal to zero, while the imaginary part equals -j/ωC, therefore the Nyquist plot is a line growing higher towards imaginary negative values the lower the frequency of the stimulating signal. The Bode magnitude plot is instead a line with slope equal to -1, and the phase is constant at 90 °C, since in a capacitor voltage and current are out of phase with $\pi/2$. It is important to note that in electrochemical cells the capacitive element usually has a phase difference different from $\pi/2$, and in order to model them, a constant-phase element (CPE) substitutes the ideal capacitor.
When the CUT is only an inductor, the situation is somewhat complementary to the capacitor case; the Nyquist plot is a line growing higher towards positive values the higher the frequency (jωL), the phase is constant and equal to -90 °C, and the magnitude plot is a line with slope 1.
More complex cases are reported as well; a resistor and capacitor in series have simi-

lar Nyquist plot to the capacitor one, just shifted toward the real value of the resitor R1. The high frequency behavior is dominated by the resistor, since C1 becomes basically a short circuit, while the low frequency behavior is mostly capacitive.
The situation is reversed for the parallel configuration of the same two elements (see **Fig. 2.33**); while the Nyquist plot appears as a semicircle. More combinations involving resitors and capacitive elements are reported as well, involving similar considerations on Nyquist and Bode plots.

Now that we have described an electrochemical cell as an equivalent electrical circuit, we can dive deeper into the 3-electrode configuration (**Fig. 2.1**), which is set to evaluate 3 parameters [20]:

> R_u, or *uncompensated resistance*, which is the ohmic resistance of the electrolyte and depends on the distance of reference and working electrodes;
>
> C_{dl}, or *double-layer capacitor*, that symbolizes the charge/discharge of the electric double layer;
>
> R_p, or *polarization resistance*, defined as the slope of the voltage/current curve $\Delta V/\Delta i$ at steady state measurements.

An electrochemical cell with a redox couple can be schematized as in **Fig. 2.34**. The total current passing through the electrolyte will be the sum of the current responsible of charge accumulation on the double layer i_C, and the current related to faradaic processes i_F. To model the diffusion and kinetics of the redox elements, Z_F is introduced; it is an impedance composed by R_{ct}, the charge transfer resistance, taking into account the kinetics of reactions and assuming no absorption of species into the working electrode, and Z_W, or Warburg impedance, which considers the diffusion of electrochemically active species to the surface of the electrode.

The resulting Z' (real part) and -Z" (imaginary part) are equal to [20]:

$$Z' = R_u + \frac{R_{ct} + \sigma\omega^{-1/2}}{(\sigma\omega^{1/2}C_{dl} + 1)^2 + \omega^2 C_{dl}^2 (R_{ct} + \sigma\omega^{-1/2})^2} \tag{2.11}$$

$$-Z'' = \frac{\omega C_{dl}(R_{ct} + \sigma\omega^{-1/2})^2 + \sigma^2 C_{dl}^2 \sigma\omega^{-1/2}}{(\sigma\omega^{1/2}C_{dl} + 1)^2 + \omega^2 C_{dl}^2 (R_{ct} + \sigma\omega^{-1/2})^2} \tag{2.12}$$

where ω is the angular frequency and σ is a parameter related to temperature, diffusion, concentration of redox species and number of electrons exchanged.
Eq. 2.11 and **2.12** indicate that for low frequencies, where the double layer impedance is very high, the behavior reduces to that of a straight line, crossing the real axis at Z' = R_u + R_{ct} - $2\sigma C_{dl}$; while the variation of Z' vs Z" at high

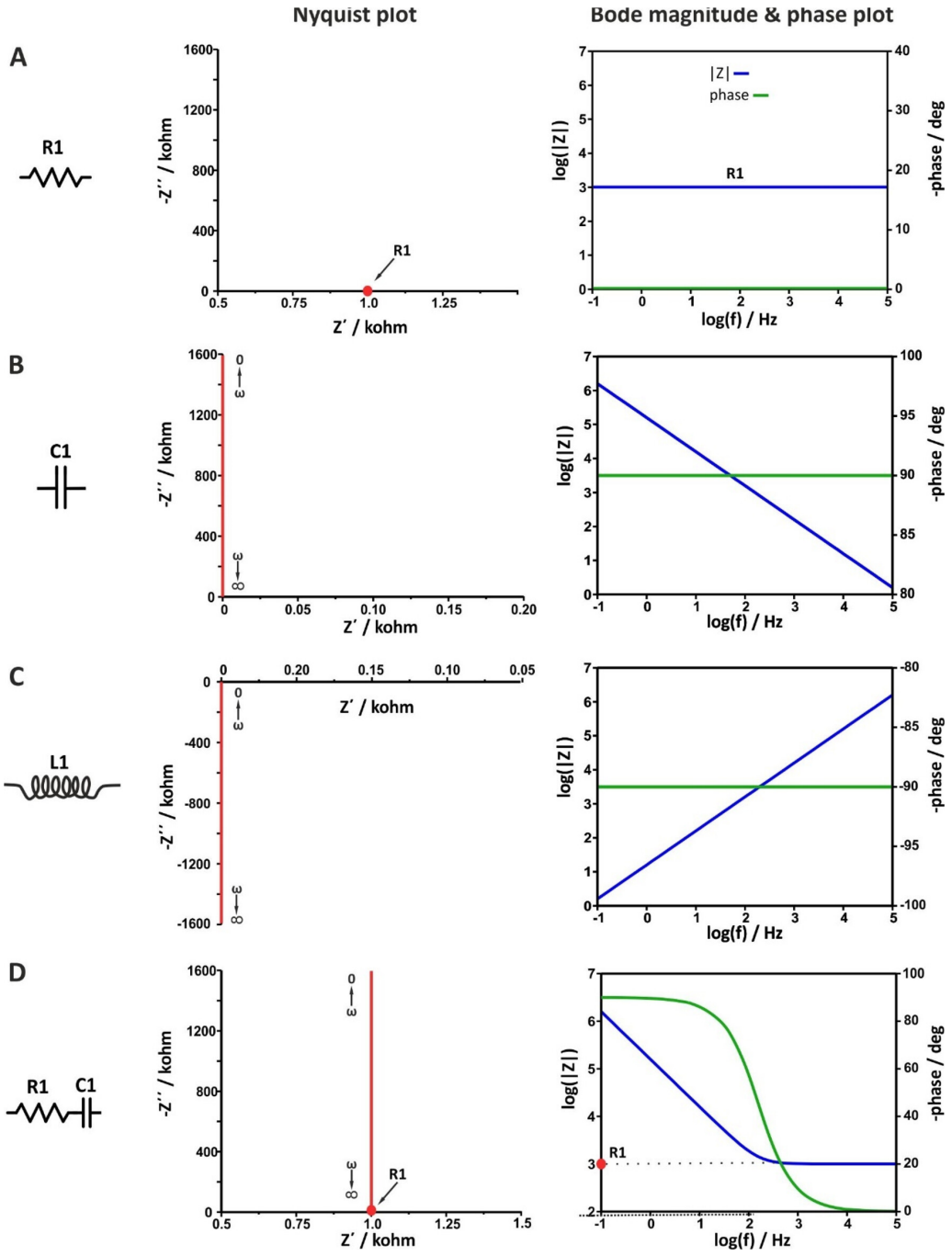

Figure 2.32: Nyquist, Bode magnitude and phase plots of some model circuits, with R1 = 1 kΩ [20]

frequency considering $R_{ct} \gg Z_W$, results in a circle with diameter equal to R_{ct} (see

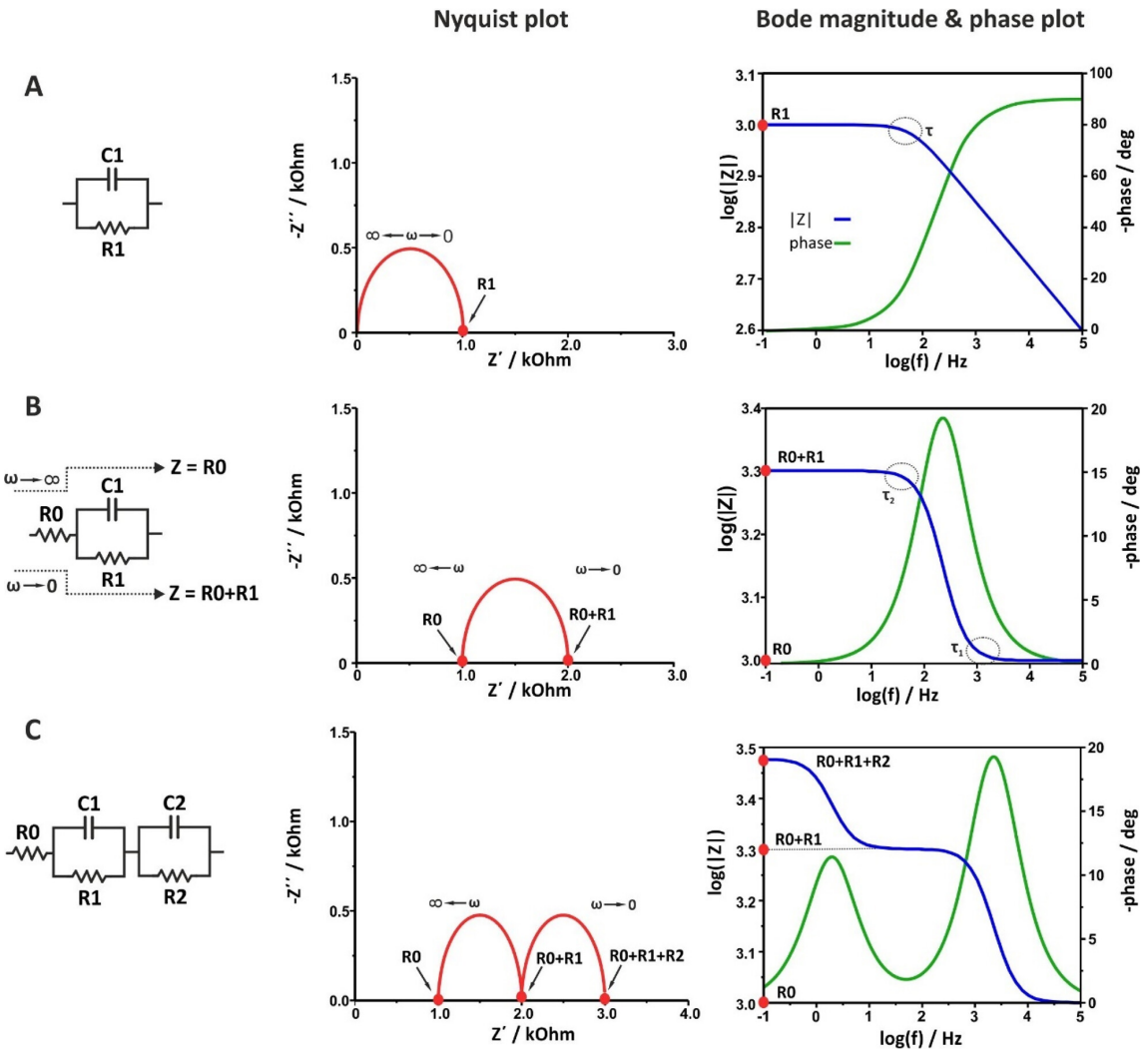

Figure 2.33: Nyquist, Bode magnitude and phase plots of yet other sample circuits, with R0 = R1 = R2 = 1 kΩ. [20]

Fig. 2.34). In real applications, the Nyquist plot of an electrochemical cell will be a mixture of the two behaviors. It is important to say that in carbon-based EDLCs, where R_{ct} becomes small in comparison to R_u and Z_W, it can be harder to have a well defined semi-circular region. At the same time the value of the double layer capacitor can be interpreted by looking at the Nyquist plot because it can considerably distort the form of the semicircle.
As already mentioned, an electrochemical cell can show non-ideal capacitive behavior in the EDL; this is mostly due to the surface roughness of the electrode, which locally varies its properties [20]. This led to the development of the Constant

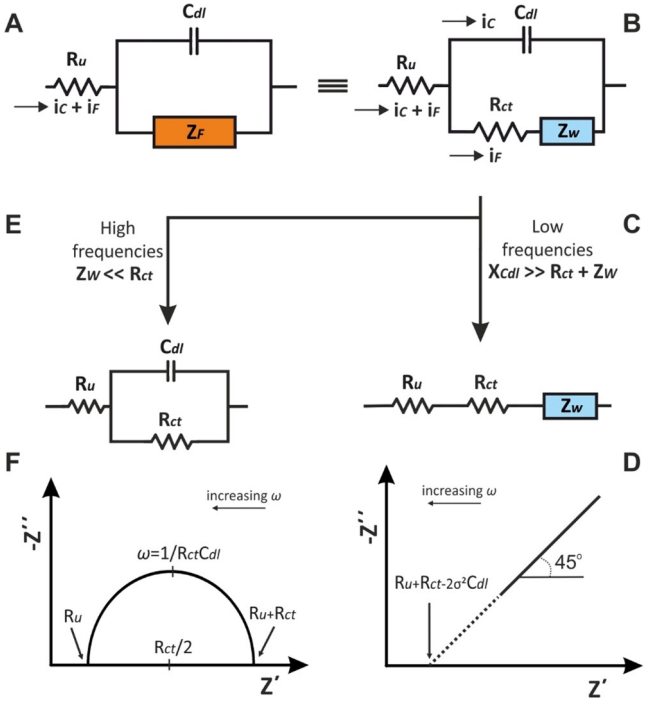

Figure 2.34: Representation of Randles circuit with low and high frequency behavior. [20]

Phase Element (CPE), which more accurately represents these imperfections. The impedance can be modeled using the CPE as follows:

$$Z_{CPE} = \frac{1}{Y_0(j\omega)^n} \tag{2.13}$$

where Y_0 is the parameter containing the capacitance information and n is a constant ranging from 0 to 1; n is also related to the tilt angle Θ of the Nyquist plot (**Fig. 2.35**) that is due to the non-ideality of the capacitor element.

For what concerns mass transfer, we have to come back to the Warburg impedance Z_W shortly. As we have been able to demonstrate, this impedance is characterized by a 45° slope in the Nyquist plot at low frequencies, which indicates semi-infinite linear diffusion of the redox species near the electrode [20]. In this scenario, the concentration gradient decreases over time as the species diffuse away from the electrode. For semi-infinite diffusion, the Warburg impedance Z_W can be modeled using a transmission line analogy, where resistors and capacitors simulate the diffusion resistance and capacitance per unit length. However, in many practical situations, the diffusion is limited by physical boundaries, creating a finite diffusion region of length

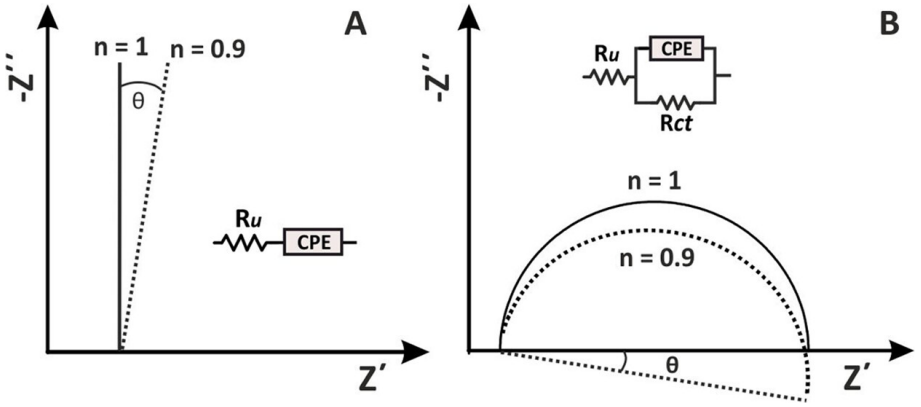

Figure 2.35: CPE behavior change vs normal capacitance (n=1). [20]

L. This region might be bounded by a permeable or impermeable material, depending on the system. When diffusion is bounded, the impedance behavior changes, reflecting the time-dependent nature of the diffusion process until the species reach the boundary. After a certain time dt the system transitions to a state where the diffusion appears semi-infinite again, until the diffusing species reach the other side of the diffusion region. This transition depends on whether the boundary allows the species to pass through or not, which significantly affects the concentration gradient and, consequently, the impedance characteristics (see **Fig. 2.36**).

When the boundary is *transmissive*, meaning that the species can pass through it or is permeable, the diffusion layer is modeled by a transmission line of finite length, terminated by an interfacial resistance R_{int}. The impedance of this system is given by:

$$Z_{\text{o}}(\omega) = \frac{1}{Y_{\text{o}}\sqrt{j\omega}} \tanh\left(B\sqrt{j\omega}\right) \tag{2.14}$$

where Y_{o} is the diffusion-related parameter, and B is a term that relates to the thickness δ of the diffusion layer:

$$B = \frac{\delta}{\sqrt{D}} \tag{2.15}$$

Here, D is the diffusion coefficient of the species.
If the boundary is *reflective*, the species cannot pass through, resulting in a different impedance behavior. In this case, the concentration gradient stabilizes, leading to a constant impedance response at low frequencies. The corresponding impedance is modeled as:

$$Z_T(\omega) = \frac{1}{Y_{\text{o}}\sqrt{j\omega}} \coth\left(B\sqrt{j\omega}\right) \tag{2.16}$$

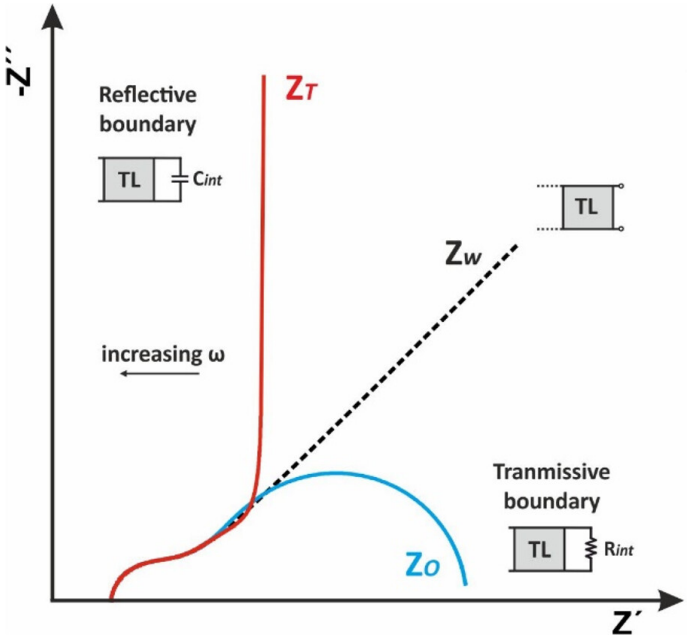

Figure 2.36: Nyquist plot showing the different impedance characteristics of T.L. terminations. [20]

This equation is similar to that for the transmissive boundary, differing only by the hyperbolic cotangent function, which reflects the inability of species to cross the boundary.

Porous electrodes exhibit a more complex impedance behavior due to the presence of pores, which affect how ions and molecules move within the electrode material. De Levie first introduced a comprehensive model for porous electrode impedance, which considers the pores as cylindrical structures of uniform diameter.
De Levie's model treats the porous electrode as a uniform transmission line (see **Fig. 2.37**), where the impedance is influenced by the interaction between the pore structure and the surrounding electrolyte solution. The equivalent circuit consists of resistances r_1 and capacitances C distributed along the length of the pores.
When redox-active species are present, a Faradaic impedance Z_F is introduced in parallel to the transmission line model, which further complicates the impedance response (see **Fig. 2.37**). This setup is crucial in systems where redox reactions occur within the pores, affecting both the diffusion and charge transfer processes.

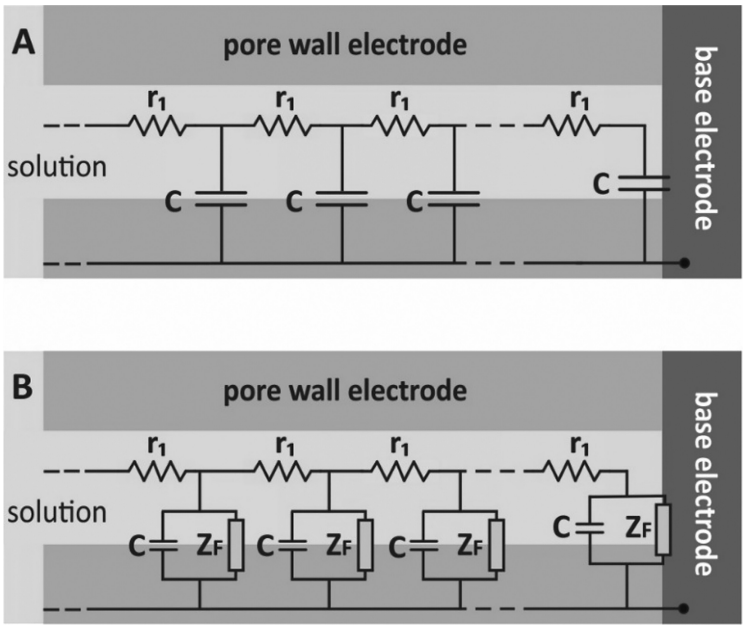

Figure 2.37: De Levie's model for porous electrodes: (A) without redox species, (B) with redox species. [20]

Chapter 3

Results and Discussion

All the following tests, unless explicity specified, were done using a Swagelok T-cell in the 3-electrode configuration described in **Sec. 2.1.1**, as most of them required the characterization of a single electrode to analyze its characteristics.

3.1 Activated carbon performance

3.1.1 ACCBPVDF-801010

As mentioned previously, in order to have a good reference regarding a carbon electrode's performance, a slurry was prepared using 500 mg of solid material: activated carbon YP-50F (80 wt%), carbon black C65 (10 wt%) and PVDF (10 wt%) (abbreviated ACCBPVDF-801010) diluted in 2.5 mL of DMSO (20 mg/mL solubility for PVDF in DMSO was roughly estimated).
Multiple electrodes were prepared right after the mixture was ready, as in previous tries it had occurred that for this particular recipe the slurry degraded rapidly in the course of one to two weeks.
Early experiments were conducted using KOH 1M, since the preliminary data available from La Sapienza exploited this particular basic environment.
One of the first tests to run, as already explained, is a CV to better understand the electrochemical stability window of the electrode. A cathodic and anodic test with two different electrodes both immersed in a KOH 1M aqueous electrolyte were performed to verify that carbon-based EDLC in alkaline conditions work better as cathodes than anodes.
The familiar graph in **Fig. 3.1** is a visualization of this first test. Every curve represents the 10^{th} iteration of the same voltage window scan, and the coulombic efficiency of every potential was calculated on this last cycle. The potential interval

was increased of 0.5 V per curve, so to have a large amount of data and a reasonable period of time accounted for the whole procedure (∼1 day). All data was collected using a scan rate of 1 mV/s, allowing faradaic side reactions to occur during the initial cycles. Coulombic efficiency was calculated as in **Eq. 1.7**, integrating the current in time to find out the total charge accumulated while charging and discharging.

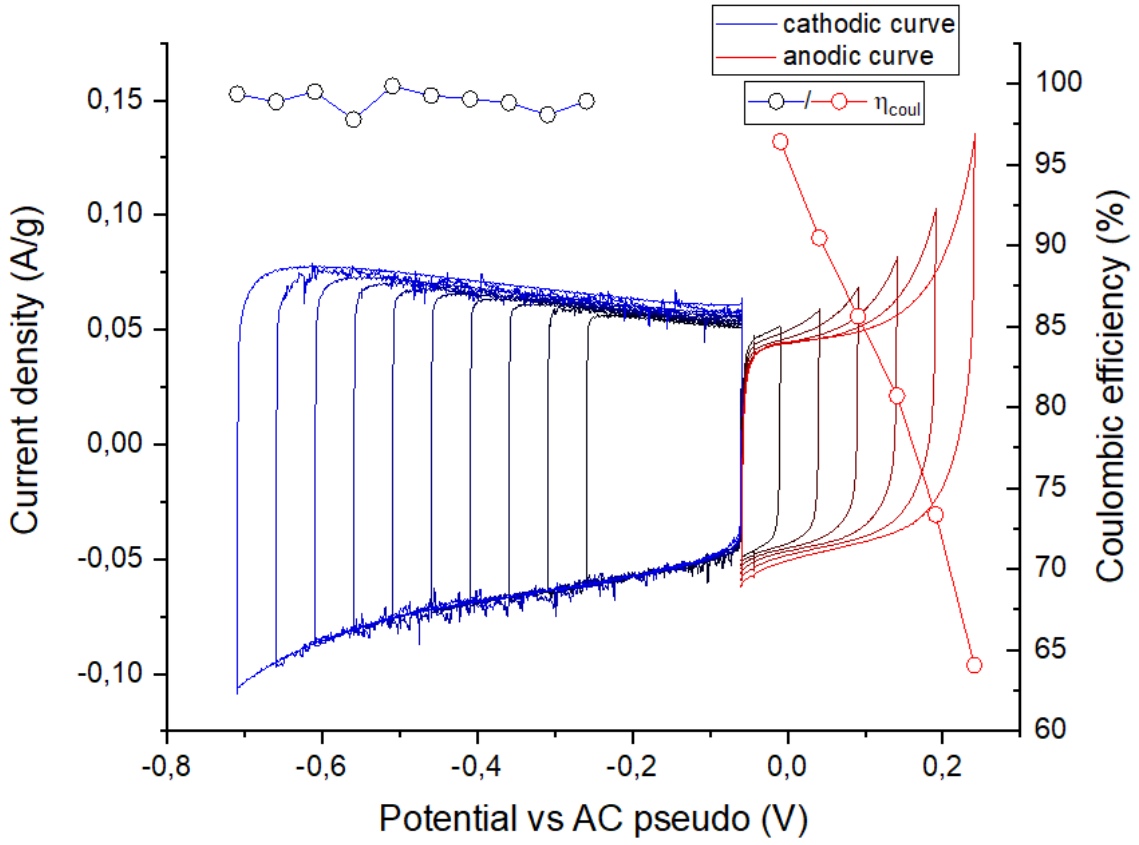

Figure 3.1: The electrochemical stability window search of ACCBPVDF-801010 in KOH 1M, investigated at 1 mV/s. The graph clearly demonstrates that carbons in a basic medium should be utilized as cathodes.

As expected, the represented curves are compatible with EDLC behaviour, so the amount of charge that will be possible to accumulate on the single electrode will be directly proportional to the applied voltage, although it is important to mention that not always charge vs potential plots have a constant slope in electrochemical cells, thus the capacitance is not constant. Coulombic efficiency values clearly indicate a high stability during cycles only for the cathodic scan. As for the anodic scan, already at 100 mV over the OCP, η_{coul} drops to 90%, meaning part of the

energy given to the system is utilized to dissociate the aqueous electrolyte. Cycling in this region brings a slow but steady degradation of the electrolyte, which will eventually break down the device. It is possible to observe that the cathodic limit of the potential window wasn't reached instead, as the efficiency would have had a steep decline from a certain point, similar to the one seen for the anodic scan.

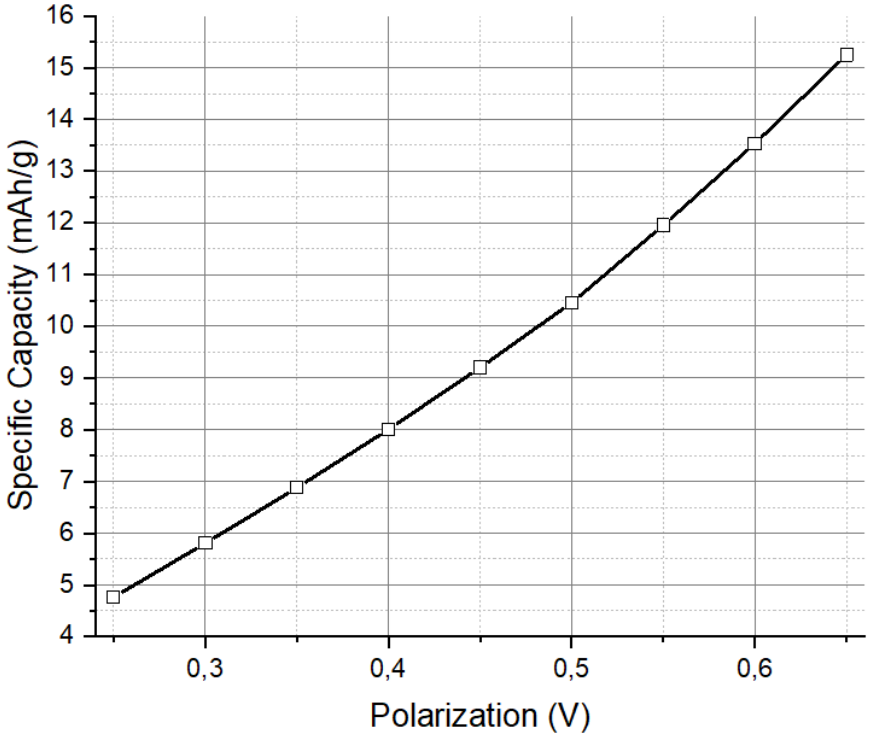

Figure 3.2: Specific capacity obtained from the IV curves above, only for the cathodic scan in KOH 1M.

In **Fig. 3.2** the specific capacity value in mAh/g obtained for the cathodic curves showed in **Fig 3.1** is represented. These have been calculated using:

$$C[\text{mAh}] = \frac{Q[\text{C}]}{3.6} \tag{3.1}$$

where 3.6 is the conversion factor between the two, given that 1 Ah equals to 3600 C. The obtained capacitance has been then divided by the weight of the dried mixture deposited on top of the Ti electrode, obtaining the specific capacity.
This gives evidence of the fact that with an increasing interval of potential, the capacitance of the electrode increases as well. This statement ceases to be true

when we hit the cathodic or anodic limit, because the amount of charge the device is able to store remains more or less the same, while the potential window increases (**Eq. 1.5**).

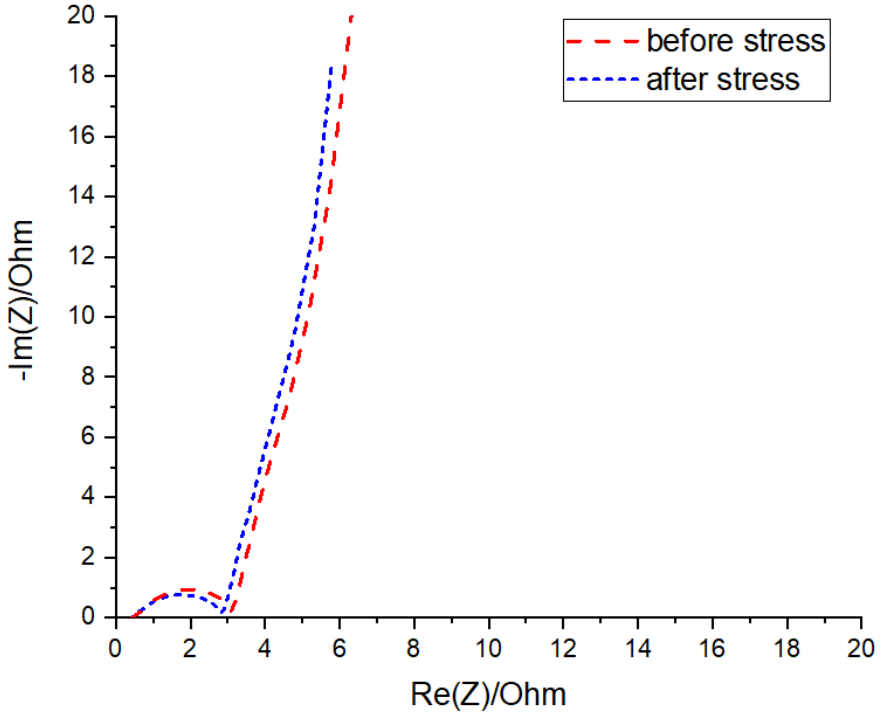

Figure 3.3: ACCBPVDF-801010 Nyquist plot at OCP in KOH 1M, with detail on high frequency.

By comparing the two curves in **Fig. 3.3**, we notice that there is only a slight decrease in the semicircle's radius; this is possible upon cycling, but the internal resistance of the device is not much altered. From the graph it is also possible to estimate the series resistance (R_{ESR}) of the device, which in this case is below 1 Ω (roughly 0.4 Ω); notice the fact that most carbon-based electrodes will have a very low R_{ESR} w.r.t. other configurations using the same electrolyte.

A preliminary GCD with ACCBPVDF-801010 in KOH 1M and a reduced potential window (430 mV) was done during this stage in order to have a more complete picture and possibly validate the numbers already obtained. The different capacitance values were measured from the experimental voltage curves (**Fig. 3.4**), reported for several gravimetric current rates; going forward C rates will be found instead (see **Eq. 2.10**). The specific capacity obtained is reported in **Fig. 3.5**, and is comparable with the quantity previously found for similar potential window specs while executing

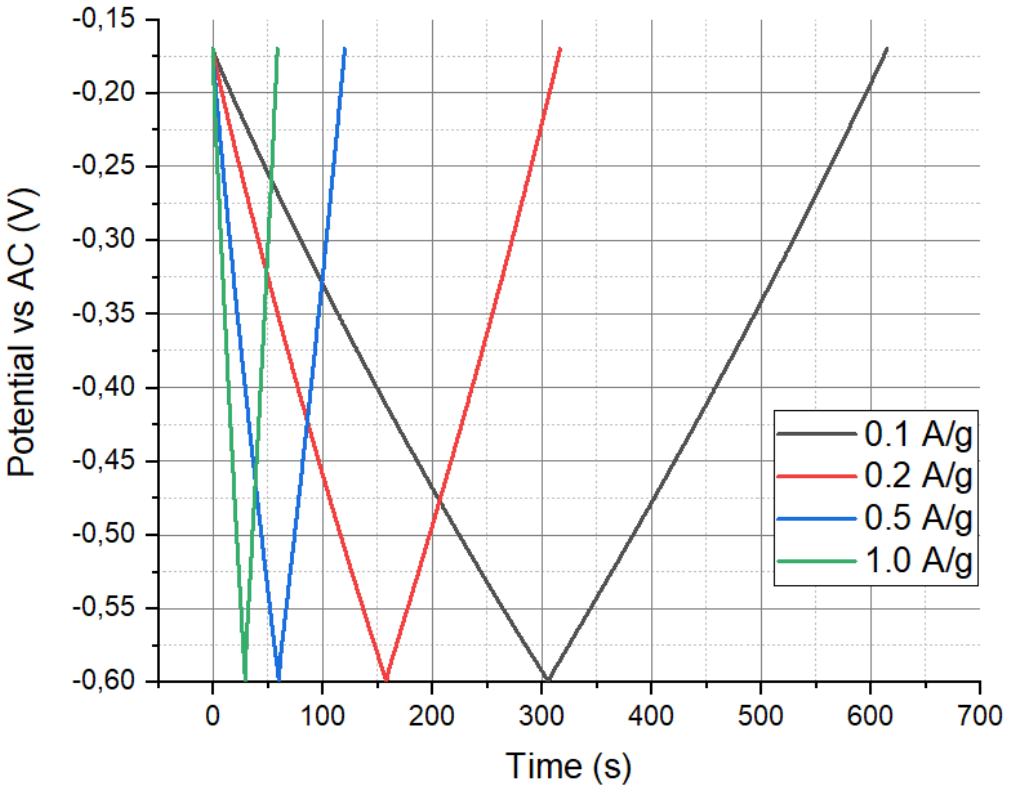

Figure 3.4: Charge and discharge curves for constant gravimetric current rates of ACCBPVDF-801010 in KOH 1M.

CVs (**Fig. 3.2**). The two electrodes utilized in the different procedures also reported comparable R_{ESR}, in this case being around 2.4 Ω. This was estimated through the I-R drop in the potential vs time graph (**Fig. 3.4**), the variation for such low values of resistance can be attributed to oxidation of the Swagelok cell's electrodes or even pressure difference when assembling the device in 3-electrode configuration.

Finally a CV at different scan rates in a reduced window (500 mV) was performed to familiarize better with all the techniques at disposal, in particular 1, 2, 5, 10, 20, 50, 100, 200, 500 mV/s were investigated, each repeated 10 times. This gave compelling insights on charge accumulation mechanism: as we can observe in **Fig. 3.6**, the shape of the I-V changes greatly with scan rate variation. The shape slowly tends to a straight line, representing the more and more dominant resistive behavior. This is in accordance with the equivalent model mentioned in **Fig. 2.34**, since a capacitor at increasing frequency will see its impedance diminishing until it becomes a short circuit; in this specific case, this is due to the time constant of the EDL mechanism, faster potential swings mean only some of the ions that participate

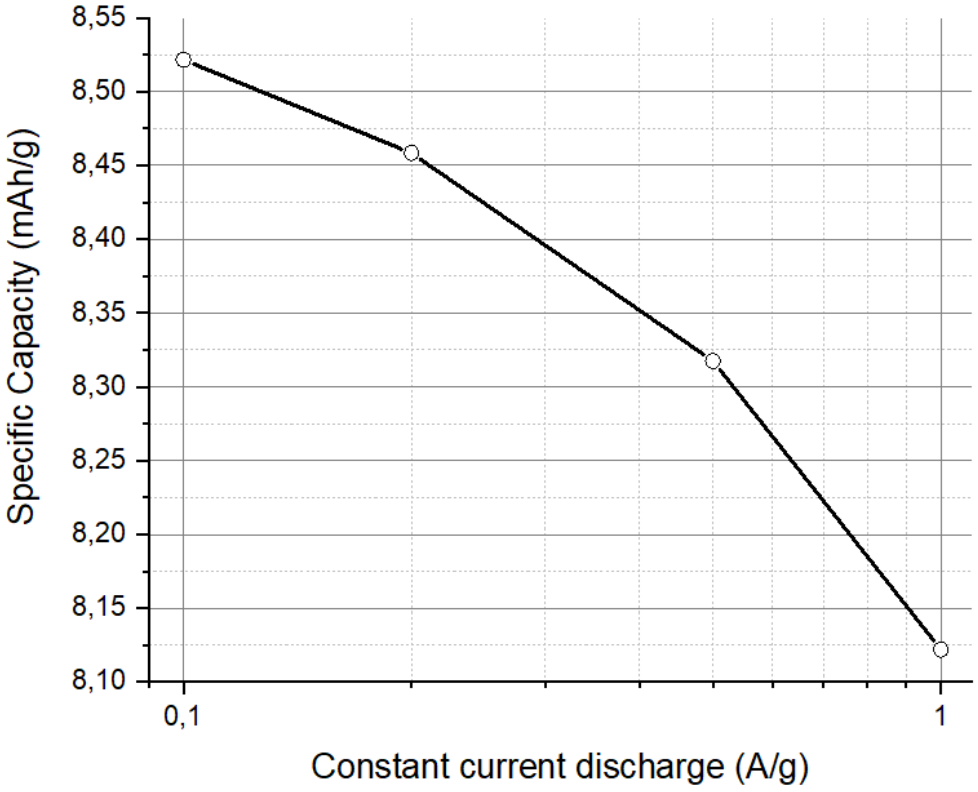

Figure 3.5: Capacity variation at different gravimetric current rates. The difference is unfortunately not as appreciable as expected; to see a decline in capacitance, much faster rates would need to be achieved.

in charge accumulation are able to reach the surface of the electrode, thus reducing the area delimited by the curve. A detail on the first (slower) cycles makes the original rectangular shape of the curves more visible (**Fig. 3.7**).

It is also possible to see how the faradaic side reactions lose their influence on faster scan rates by following the η_{coul} trend: since their time constant is slower, all the charge is generally accumulated and released, provinding coulombic efficiency close to 100%. The only exception happens for far too high scan rates (basically 1 Hz sine wave), when the current dissipated on the R_{ESR} starts being comparable to the charge accumulated in the device.
Specific capacity was calculated again by integrating the current in time, obtaining similar values to the ones already found; the decrease validates the aforementioned statements (**Fig. 3.8**).

The starting point of this work was actually to build a symmetrical SC using only

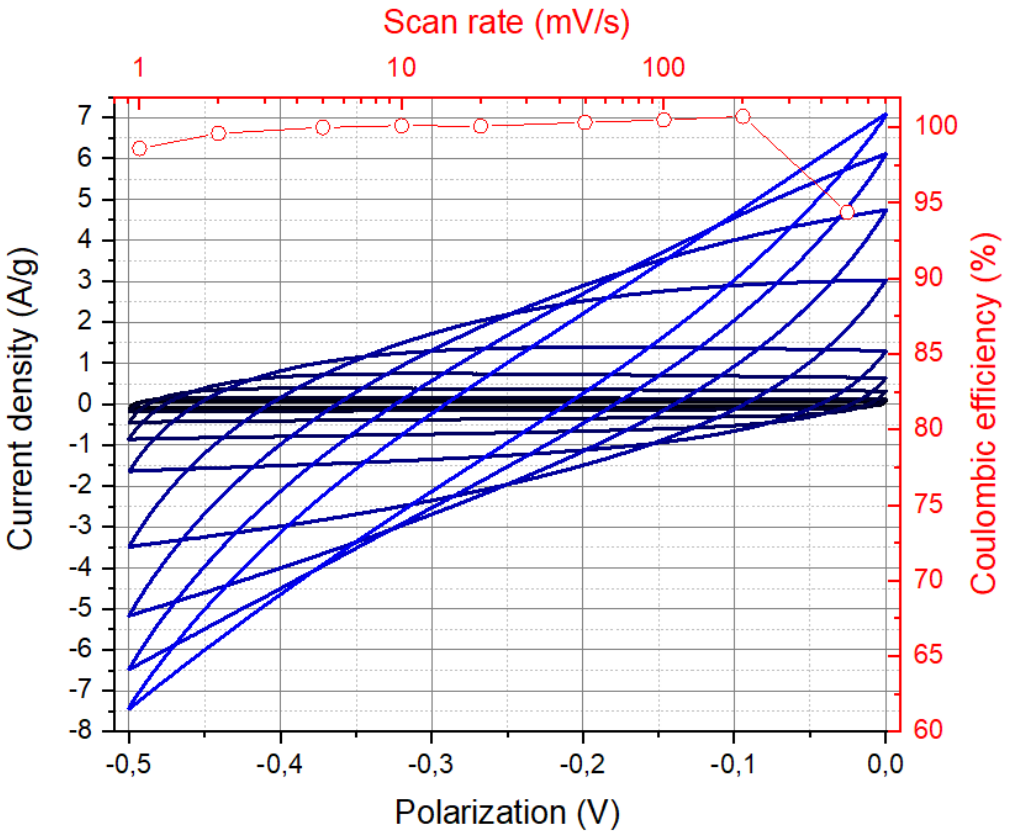

Figure 3.6: CVs of ACCBPVDF-801010 in KOH 1M operated at different scan rates, with indicated coulombic efficiency.

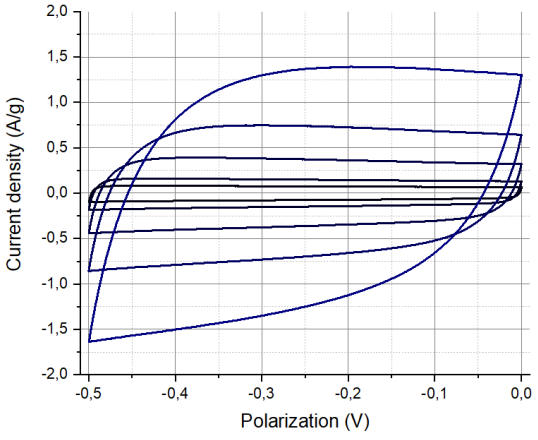

Figure 3.7: Detail of the slower CVs.

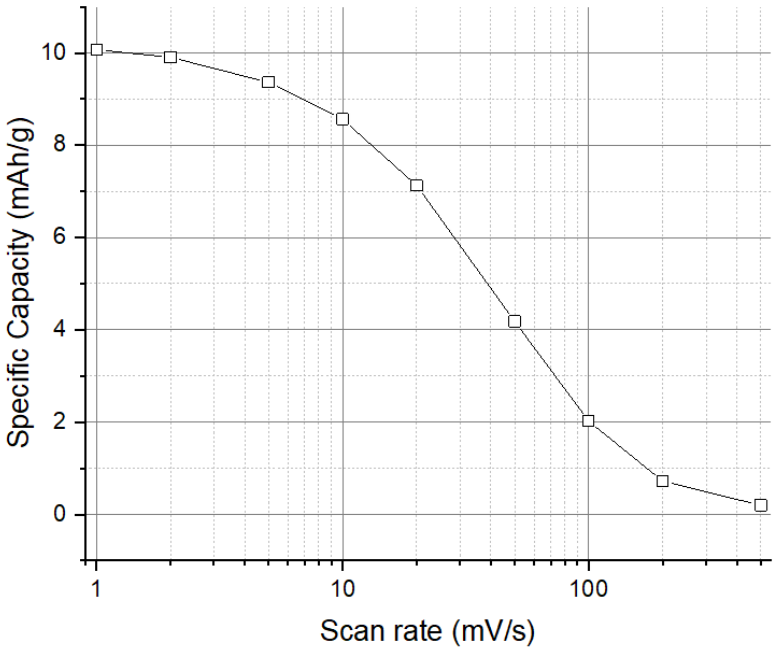

Figure 3.8: Specific capacity change at different scan rates.

aerogel, but given the results obtained in these very first tests with AC, the mass balancing of the final device would have required an unfeasible ratio. Carbon in basic environment has in fact shown a pretty evident tendency toward oxygen evolution upon small polarization (**Fig. 3.1**). An hybrid design was therefore proposed including lithium manganese oxide: given the intrinsic compatibility of the compound with lithium ions [23], KOH 1M was substituted by LiOH 1M in the design. An ESW test was performed once again on the AC electrode, this time in LiOH 1M, which reported only a slight decrease in performance, as R_{ESR} was measured to be around 1.5 Ω; the maximum specific capacity value reached 12.4 mAh/g (vs 15.2 obtained in KOH) for the selected window (0.65 V), and the R_{ct} is one order of magnitude higher, reaching 30 Ω (3 Ω in KOH).

3.1.2 ACCBHPC-85105

With a view on a more sustainable product, the active mixture was changed to include hydroxypropyl cellulose (HPC), a different binder chosen as the substitute of PVDF, with which obtaining an homogeneous solution with the compounds described above was difficult, as it degraded faster than we would have hoped. HPC is water-soluble, can be used in combination with aqueous electrolytes and the necessary wt% is 5% as opposed to 10% of PVDF, thus hypothetically favoring the capacitive behavior of the electrode. The mixture was prepared with 500 mg of total mass, according to the following proportions: activated carbon YP-50F (85 wt%), carbon black C65 (10 wt%) and HPC (5 wt%) (abbreviated ACCBHPC-85105), dissolved into 2.5 mL of DIW.
In the course of these tests we registered an unexpected decrease in capacitance and in coulombic efficiency.

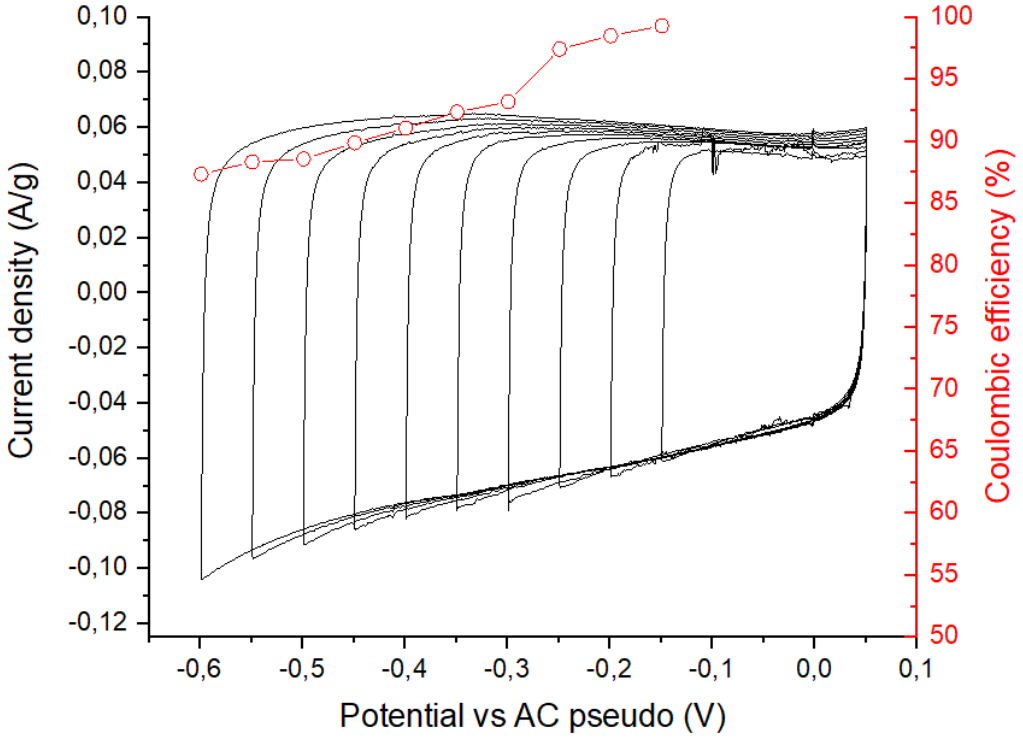

Figure 3.9: ACCBHPC-85105 in LiOH 1M voltage window search, investigated at 1 mV/s with specified coulombic efficiency.

As we can see in **Fig. 3.9**, beside the first few cycles, η_{coul} drops relatively fast to sub-optimal values; this should not happen while inside the water stability window, unless the ability of the material to hold charge is degrading, which would be revealed

by a plateau in the specific capacity trend. This wasn't the case (**Fig. 3.10**), but rather the oxygen present inside the electrolyte from continuous exposure to our atmosphere was producing high residual currents. This has been observed previously [52], and fluxing the electrolyte with an inert gas has been proven to be a good way to remove it.

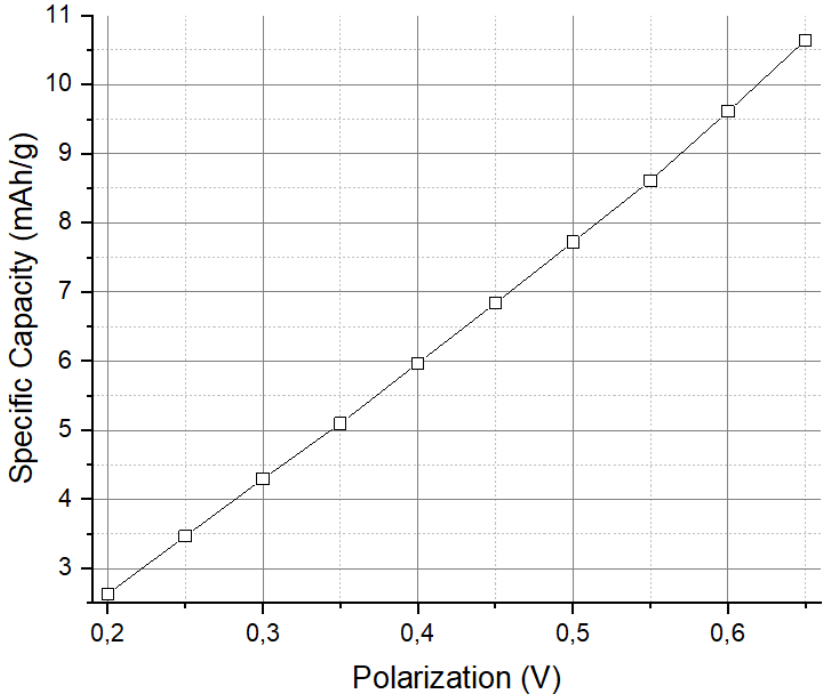

Figure 3.10: Specific capacity variation on window increase, the maximum value is around 10.6 mAh/g, which is fairly lower than the previously found 12.4 mAh/g.

So another test was performed with the same setup, the difference being that the electrolyte was fluxed with nitrogen for an hour before utilization. The maximum potential applied was also increased to see how far it was possible to push the electrochemical stability window. The results can be seen in **Fig. 3.11**, showing much better efficiency than the last graph reported, changing nothing but the electrolyte condition. It also appears that we are near the cathodic limit for the considered material in LiOH 1M, as the efficiency drops to fairly low values after applying more than 0.7 V potential. Specific capacity shows a good improvement as well, reaching 14.5 mAh/g for 0.65 V (**Fig. 3.12**), reflecting the wt% increase in active material we were expecting. Therefore the electrolytes from this point on will always undergo nitrogen fluxation before utilization.

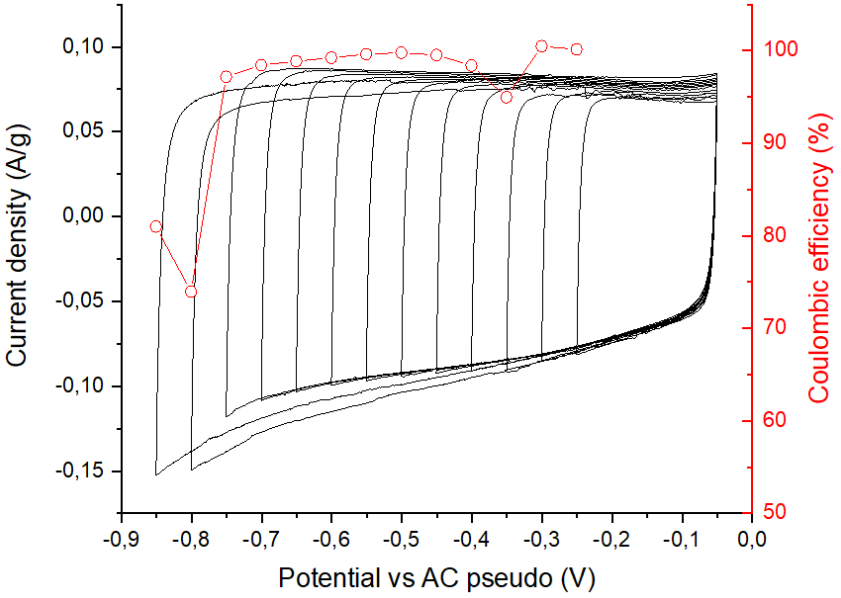

Figure 3.11: Electrochemical stability window for the ACCBHPC-85105 in LiOH 1M, investigated at 1 mV/s, this time without the influence of oxygen, thanks to nitrogen fluxation.

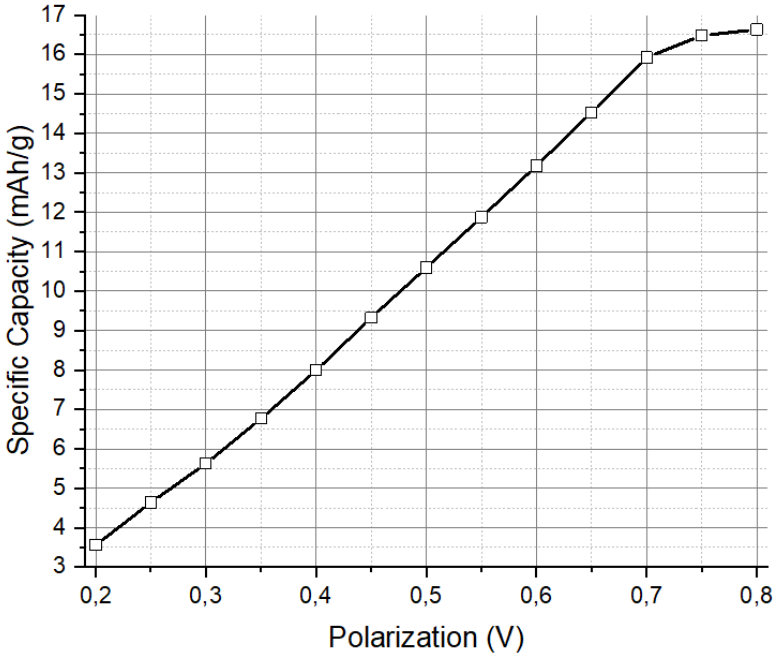

Figure 3.12: Specific capacity variation on window increase with degassed electrolyte, results are now more in line with expectations.

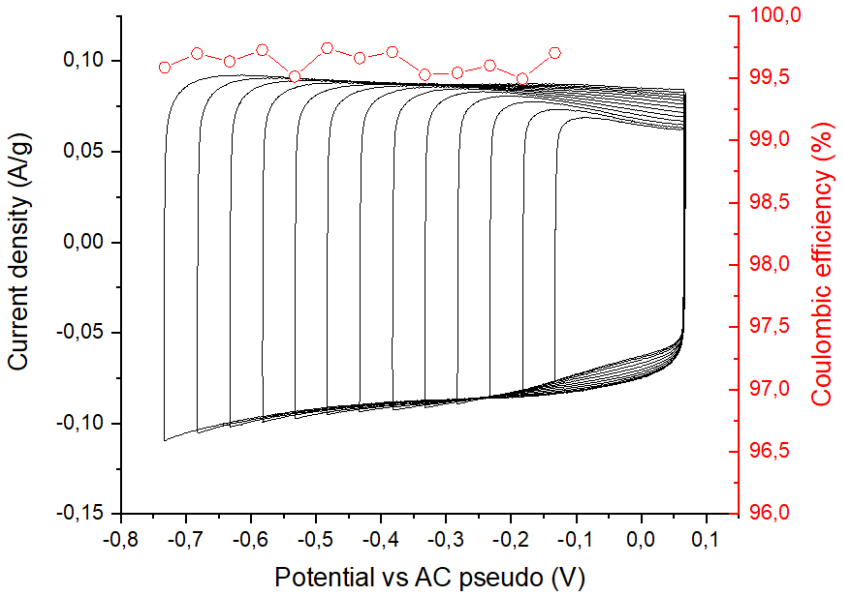

Figure 3.13: Electrochemical stability window of ACCBHPC-85105 in Li_2SO_4 2M, investigated at 1 mV/s with specified coulombic efficiency.

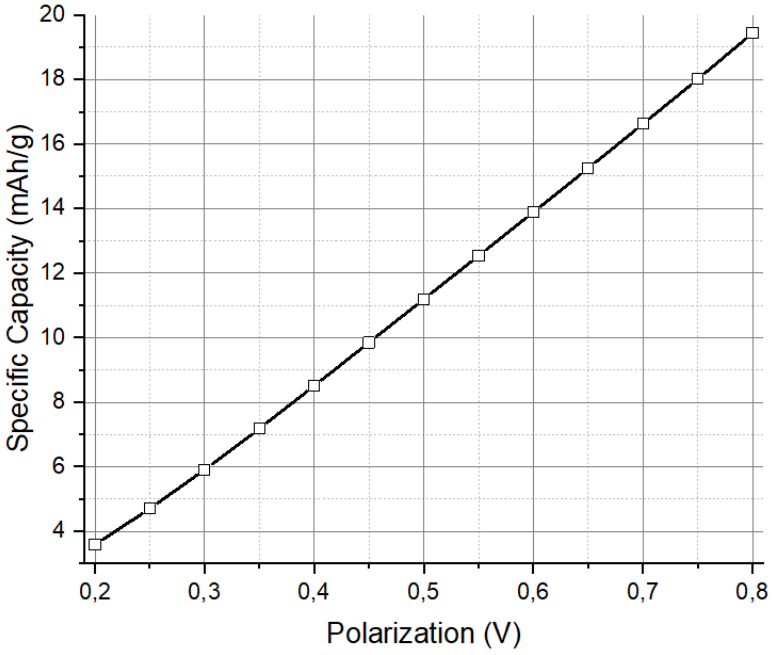

Figure 3.14: Specific capacity variation on window increase.

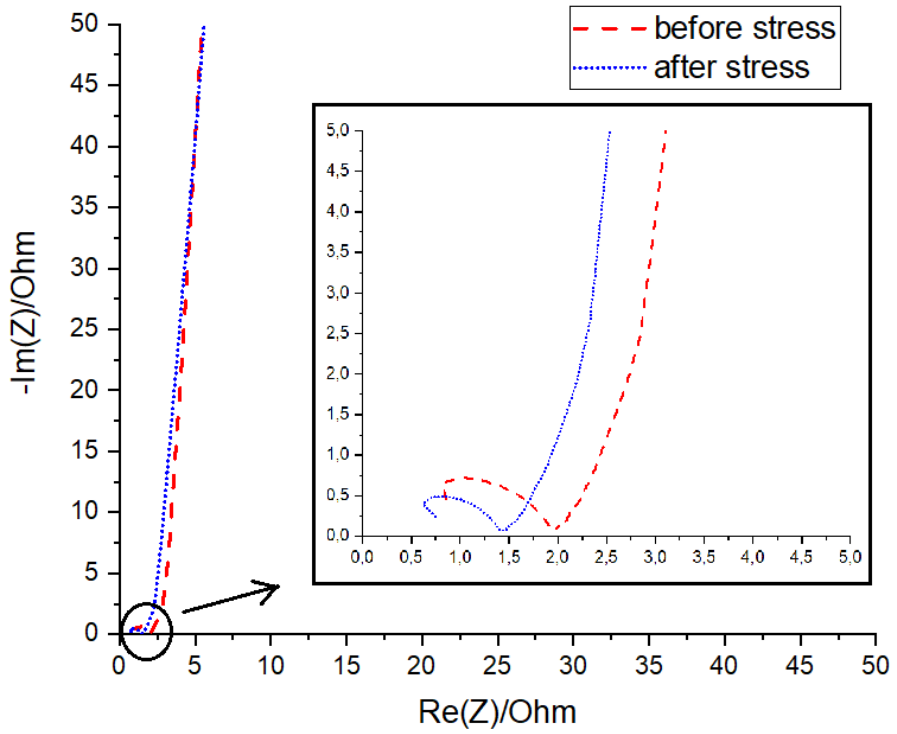

Figure 3.15: ACCBHPC-85105 Nyquist plot at OCP in Li_2SO_4 2M, with detail on high frequency.

One last experiment with ACCBHPC-85105 was performed in Li_2SO_4 2M (neutral environment), for reasons that will be explained in the following section. As it appears from **Fig. 3.13**, the ESW is now extended as the coulombic efficiency does not show sign of decrease around the critical points highlighted before. From now on the ESW will therefore be assumed to be at least 0.8 V, since time constraints prevented the possibility of investigating further potentials (1 mV/s scan over 800 mV for 10 times for forward and reverse scan takes around 4.5 hours, just for the last 10 cycles of the procedure). For what concerns specific capacity, the related graph (**Fig. 3.14**) shows linear increase with potential, with a maximum capacity reached of 19.4 mAh/g (15.25 mAh/g for 0.65 V window). Finally, the Nyquist plot in **Fig. 3.15** shows an impedance behavior that is the one expected for an electrochemical SC, with an approximated vertical line at low frequencies, a linear trait due to Warburg impedance, and a small semicircle indicating R_{ct}. Due to high frequency limitations and tolerances when measuring, it wasn't possible to calculate R_{ct} and R_{ESR}, but the estimated values are comparable to previous measures.

3.2 $LiMn_2O_4$ performance

Lithium Manganese Oxide (LMO) was selected as the active material for the faradaic electrode composing the hybrid SC. It was mixed with the same components (for the same total mass, 500 mg) in different weight percentages: LMO (70 wt%), C65 carbon black (25 wt%), and HPC (5 wt%) (abbreviated LMOCBHPC-70255) in 2.5 mL of DIW.

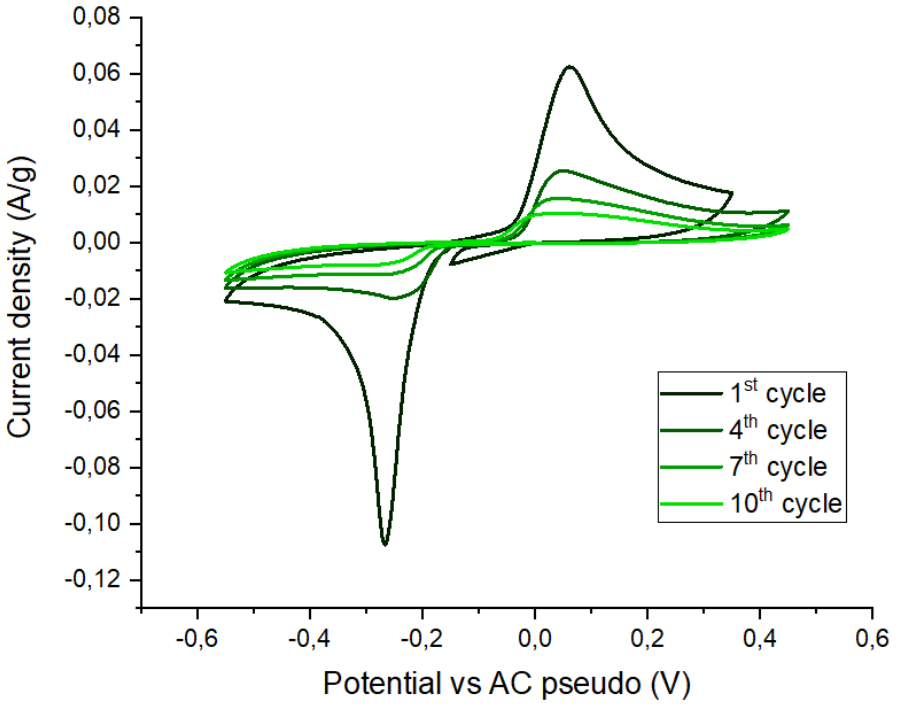

Figure 3.16: Electrochemical stability window search for LMOCBHPC-70255 in LiOH 1M, investigated at 1 mV/s.

As we can see from **Fig. 3.16**, when using LiOH 1M in a 1 mV/s CV there is a noticeable loss of capacitance after a few cycles. This is not ideal for a low maintenance application, but literature on the subject suggested that LMO in neutral environment (Li_2SO_4) has a much better capacitance retention [12]. Some hypotesis were discussed for the explanation of this behavior, like low lithium concentration; but the high electrochemical irreversibility of the process because of the separation between extraction and insertion peaks pushed the work in the direction of a neutral environment.

Following these results and the example reported in [12], a Li_2SO_4 2M solution was

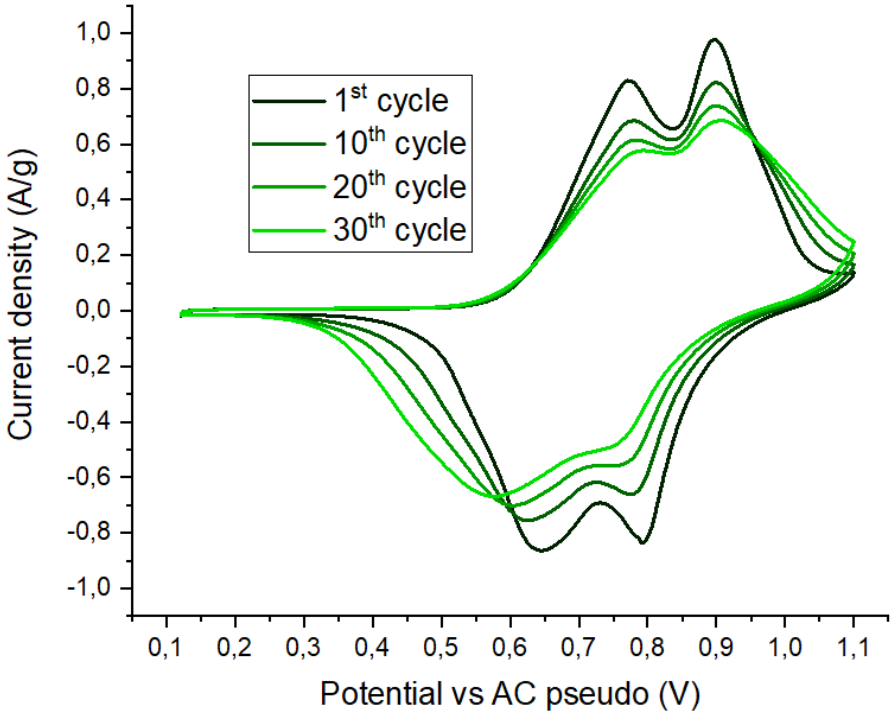

Figure 3.17: Electrochemical stability window search for LMOCBHPC-70255 in Li_2SO_4 2M, investigated at 1 mV/s.

prepared; the result of the 1 mV/s scan is reported in **Fig. 3.17**, showing much better capacitance retention and electrochemical reversibility of the process, wider ESW, and highlighting a second pair of peaks. The fact that both intercalation and de–intercalation peaks are present in the anodic scan, is also convenient for the final device assembly. As it turns out, the two pairs of peaks correspond to a two-step process of insertion/extraction, separated by about 150 mV [38]. After this test, further experimentation was done only using Li_2SO_4 2M. PEIS investigation was carried out to check for possible differences before and after the procedure, the Nyquist plot can be seen in **Fig. 3.18**.

LMO showed a significantly more electrochemically reversible process in Li_2SO_4 w.r.t. LiOH. However, capacity loss was observed also in the case of Li_2SO_4 even if less pronounced. In order to investigate the phenomenon we performed a titration study carried out at low charge dose. In other words, LMO was test in galvanostatic control to study the reversibility of the two oxidation processes at low current rate in order to stress loss phenomena. One experiment was performed by covering the two oxidation reactions, while one experiment was conducted to let the material undergo just one oxidation reaction. The currents were determined by using C

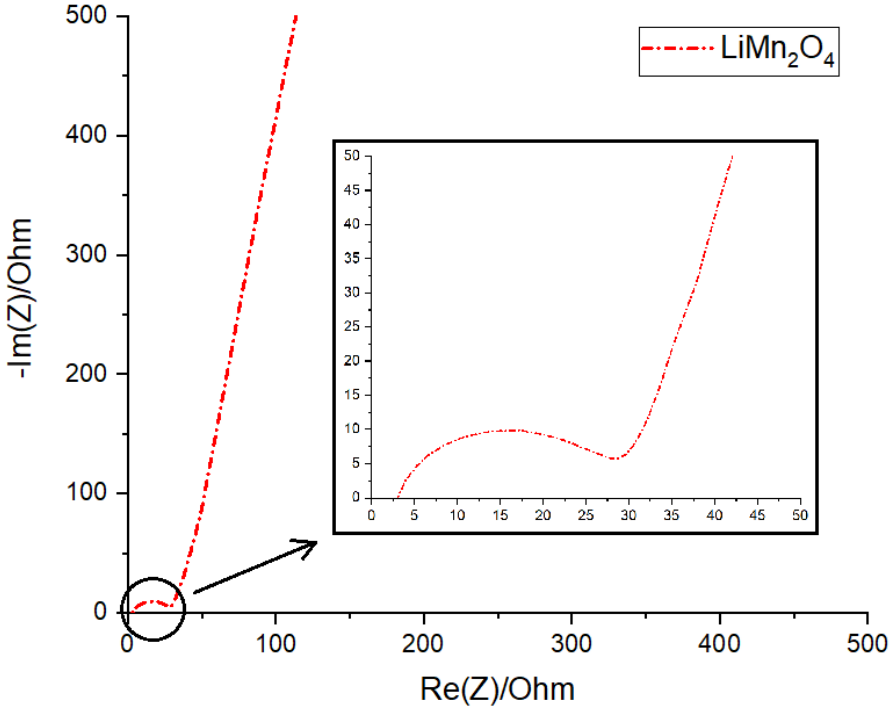

Figure 3.18: LMOCBHPC-70255 Nyquist plot in Li_2SO_4 2M, with detail on high frequency.

rates, therefore taking the theoretical capacity of the material, multiplying it for the wt% inside the electrode of the LMO (0.7) and multiplying again by the total weight of the deposited mass on the current collector, thus obtaining C (usually in the order of hundreds of μA). For both procedures C/10, C/5, C/2, C, 2C and 5C rates have been investigated.

The results are reported in **Fig. 3.19(a)** and **3.20(a)**, showing just the slowest part (C/10) of the experiment; different currents have been set for each one because two electrodes with different mass loading were tested. Just by inspecting quickly the charge and discharge periods, coulombic efficiency in **Fig. 3.19(b)** suggests that the two processes are not reversible and most likely the second one is completely irreversible. Moreover, one might assume that the material produced during the second oxidation is not chemically stable, dissolving in the electrolyte. These results are confirmed by the highly efficient results obtained by causing only the first oxidation, and by noticing that the capacity retention is not affected upon cycling **3.20(b)**. The relative values of specific capacity per C rate are reported, going from slowest (C/10) to fastest (5C); 4 cycles per C rate were executed on the first test, while 6 cycles each were performed for the second. Although at slower rates η_{coul}

was still increasing, and we probably needed much more time for performing the test, the graph shows much better capacity retention and potential for high stability upon cycling.

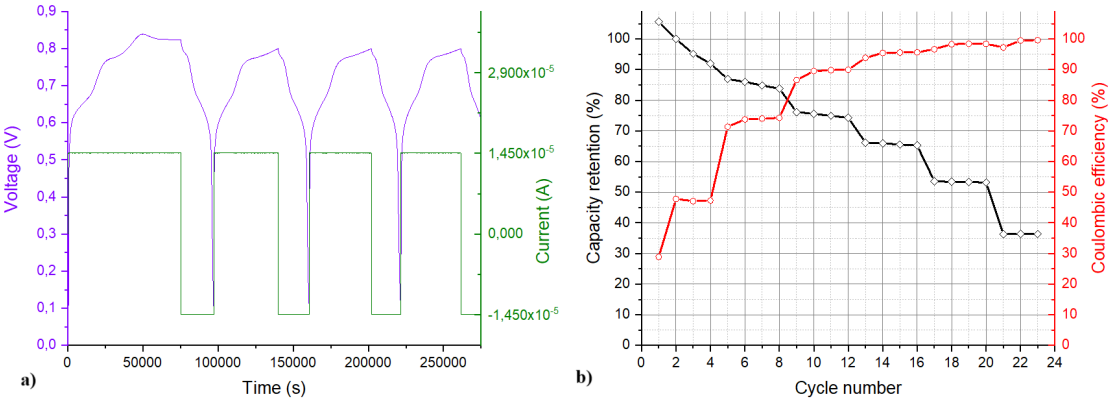

Figure 3.19: (a) Detail of GCD with both redox peaks included in the potential window, in the first cycle the anodic limit was reached, therefore the maximum potential was lowered in the following cycles; (b) specific capacity on C rate variation of the procedure.

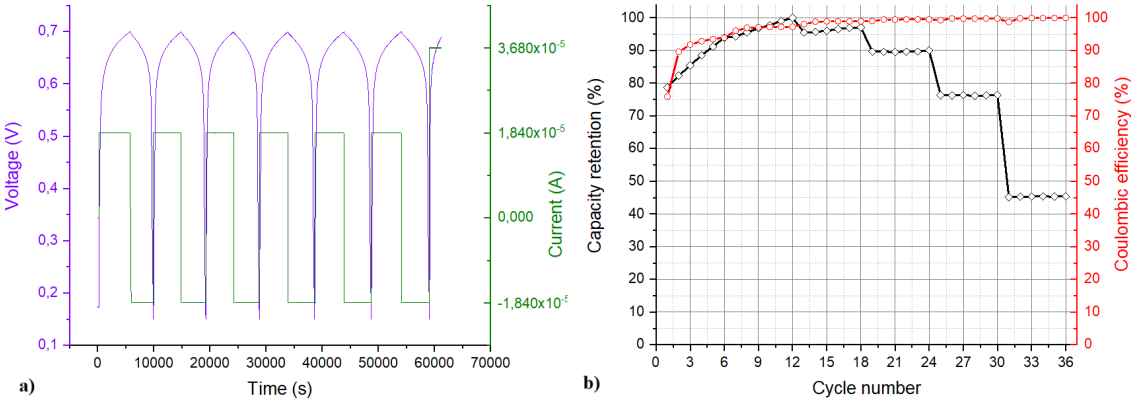

Figure 3.20: (a) Detail of GCD with only the first redox peak included in the potential window; (b) specific capacity on C rate variation, for the first few cycles an increase in capacity due to better coulombic efficiency is visible.

Finally a float test was executed to measure leakage current and cyclability of the faradaic electrode. Part of the procedure can be seen in **Fig. 3.21**, and is composed of 2 cycles of charge and discharge at C/10, calculated as previously described, and a third cycle in which the electrode is charged at the maximum voltage (0.7 V, about 0.5 V over the OCP), that potential is then held for 10 hours, and discharged again to

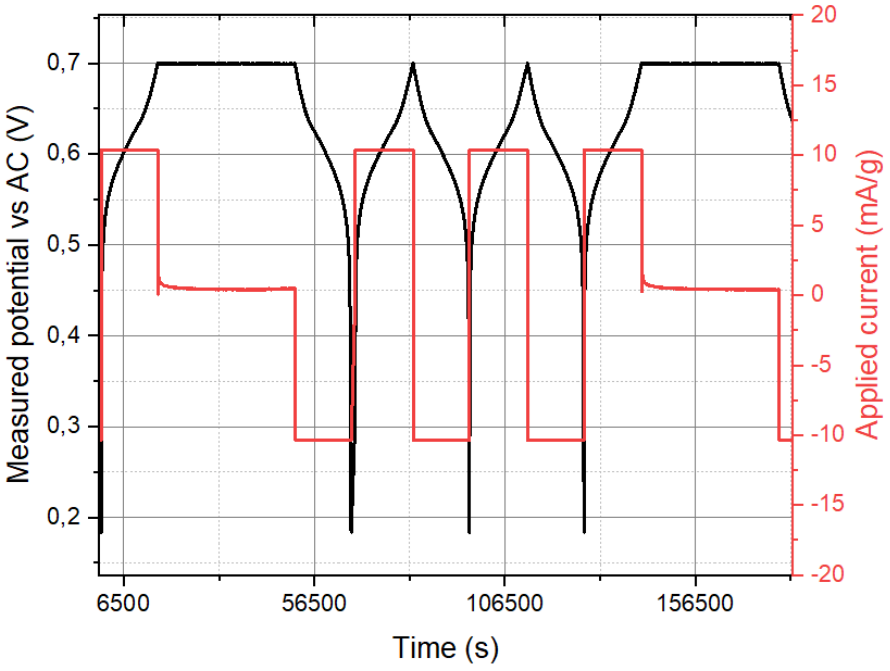

Figure 3.21: Detail of the full float test executed on LMOCBHPC-70255 in Li_2SO_4 2M.

create a loop in the end. Such low constant current was adopted to simulate harsh working conditions, since charging with a DSSC in scarcely lighted environment would take a long time. Depending on measured current density, which in the case of solar cells has a strong dependency on illumination, the DSSC (or the SC) has to be properly sized for an optimal trade-off that allows full charge within the "lighted" period, possibly staying around the maximum rated voltage as shortly as possible, to prevent fast ageing. A PEIS technique is carried out in every loop to see if the device under test undergoes modifications. In this case LMO was registered to have a mean capacity of 42.5 mAh/g, compliant with initial galvanotatic tests (**Fig.3.22**). Coulombic efficiency is also pretty high (96.5%) for a procedure slow enough to stresses out loss phenomena. From every third cycle it is also possible to extract the leakage current, which falls in an interval between 0.9 and 1.2 μA (450 and 600 μA/g, respectively).

Despite having a η_{coul} generally lower than most carbon based electrodes, the energetic efficiency η_{energy}, corresponding to the ratio between energy released and accumulated during charge, is just below 96%, which is a very good result. The Nyquist plot does not show considerable differences between cycles, meaning no significant transformation has happened, and confirming the reversibility of the pro-

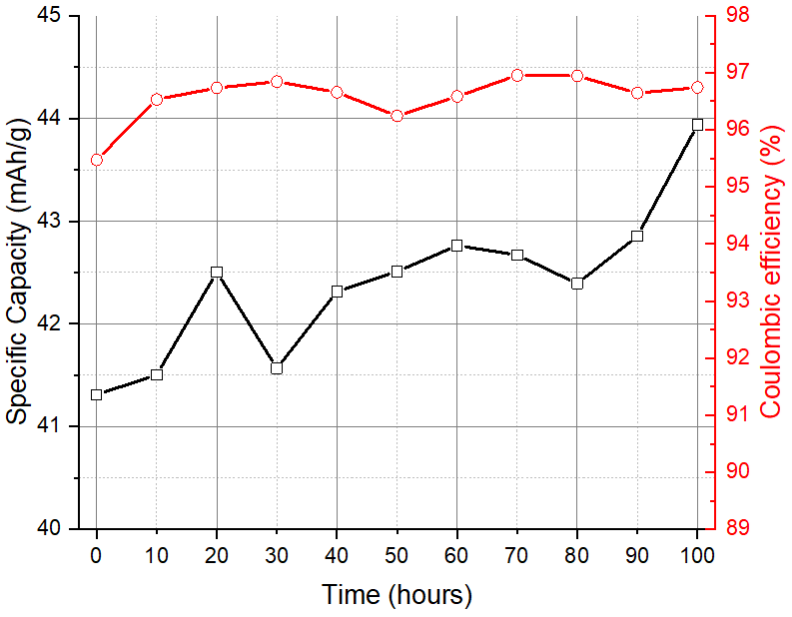

Figure 3.22: Capacity and coulombic efficiency at the start of every potential hold (10h).

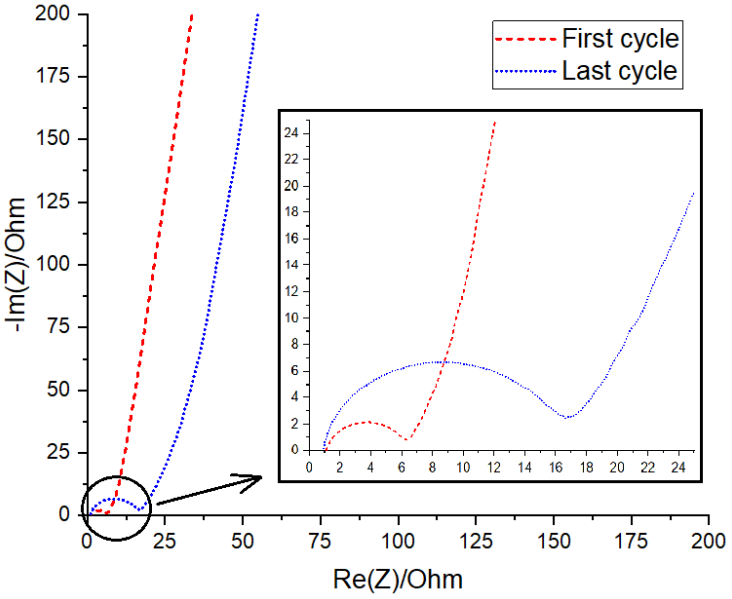

Figure 3.23: LMOCBHPC-70255 Nyquist plot at OCP in Li_2SO_4 2M, with detail on high frequency.

cess. In fact, while the slope of the line at low frequency does not change, the only appreciable difference between the first and last PEIS is an increase of the semicircle corresponding to R_{ct}. This is probably due to a phase change during insertion and extraction of lithium that can result in a change of volume in the active compound, causing a resistance variation. The R_{ESR} is estimated to be around 1.5 Ω.

3.3 Aerogel performance

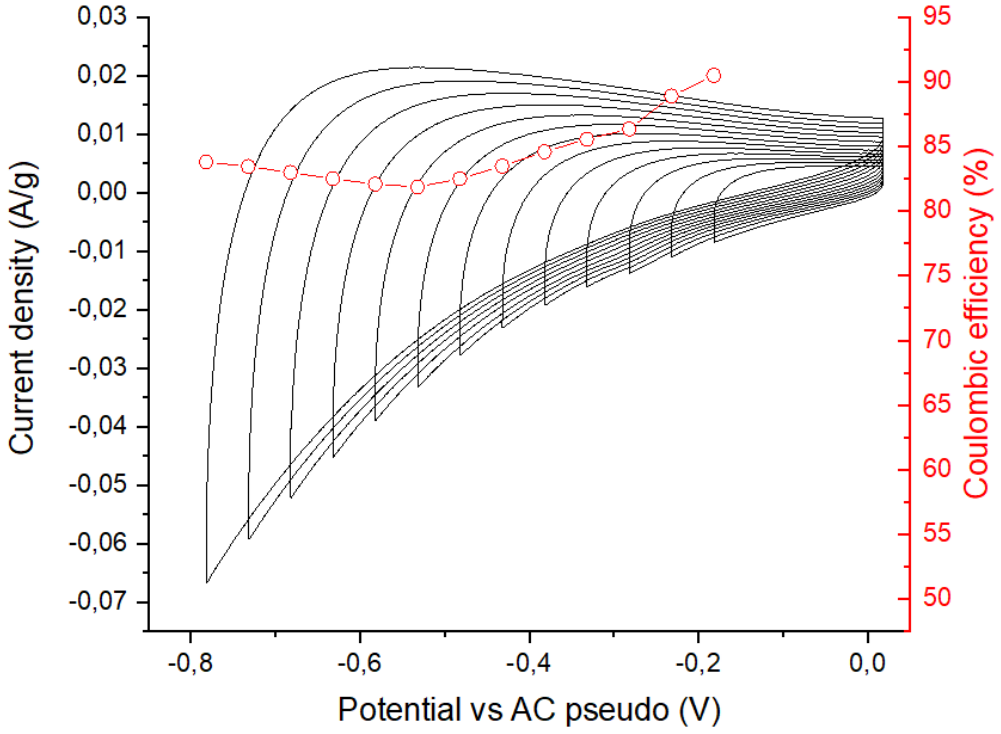

Figure 3.24: Electrochemical stability window for the GELCBHPC-85105 in Li_2SO_4 2M, investigated at 1mV/s.

The first attempt to use aerogel to create a slurry was done by using mortar and pestle to pulverize it. The available compound reached 200 mg at most, therefore 170 mg of it were used to produce the slurry, adjusting the weight of the other components accordingly, while the rest was used to conduct other investigations. The mixture was composed by carbon aerogel (85 wt%), C65 carbon black (10 wt%), and HPC (5 wt%) (abbreviated GELCBHPC-85105), in 1 mL of DIW.
As hinted before, only characterizations in Li_2SO_4 2M will be shown in the following, although the behaviour resulted similar in most of the other electrolytes. The ESW search is shown in **Fig. 3.24**, the graph hints at a rather resistive behavior,

given the shape is quite deformed w.r.t. previous CVs. The rising peak of current towards negative voltages can be easily mistaken for a sign of reductive decomposition of the electrolyte, but the η_{coul} trend disproves this hypothesis. Capacitance values are also quite disappointing **Fig. 3.25**, reaching 3.4 mAh/g at most. Either way, the efficiency seems too low for a porous carbon-based compound and further investigation was conducted.

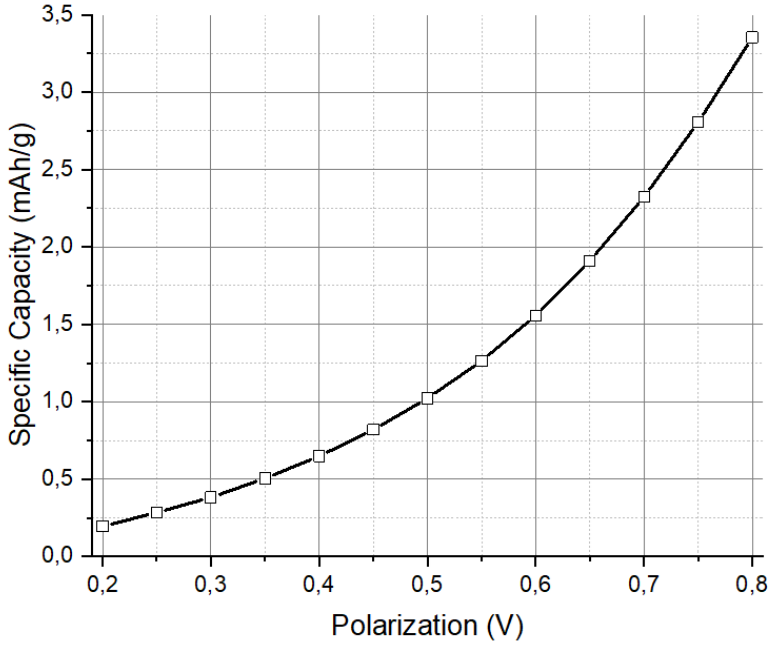

Figure 3.25: Specific capacity variation on potential window increase.

First and foremost, a SEM investigation was carried out on both the aerogel powder and the areogel slurry, since it seemed that the deposited quantity on the Ti current collector was rather thin w.r.t. other coated electrodes (at least to the naked eye). The results provided interesting insights; as we can see from **Fig. 3.26**, the aerogel powder does not appear to be uniform, with big and elongated particles occupating a lot of volume. It would seem that mortar and pestle is not a good way of pulverizing the aerogel, and maybe a more sophisticated technique is necessary. This reflects negatively in the slurry, since it is harder to have a uniform and homogeneous solution with CB and HPC. The impact on the Ti coating is visible in (**Fig. 3.27**), where a comparison between an activated carbon slurry (with PVDF as binder) and the areogel one is presented. It seems like only the smaller particles have been able to merge in the mixture, but this has not created an intricate set of connections like in the case of AC, despite the larger particle dimension in the latter. It is also worth mentioning that on the sample were occasionally found some

traces (negligible) of silicon and nitrogen thanks to the EDX spectroscopy: they are residues of the synthesis procedure.

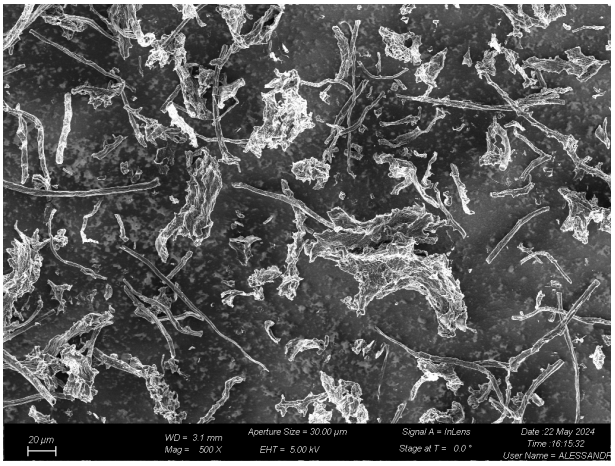

Figure 3.26: SEM image of the aerogel powder obtained by crushing it with mortar and pestle.

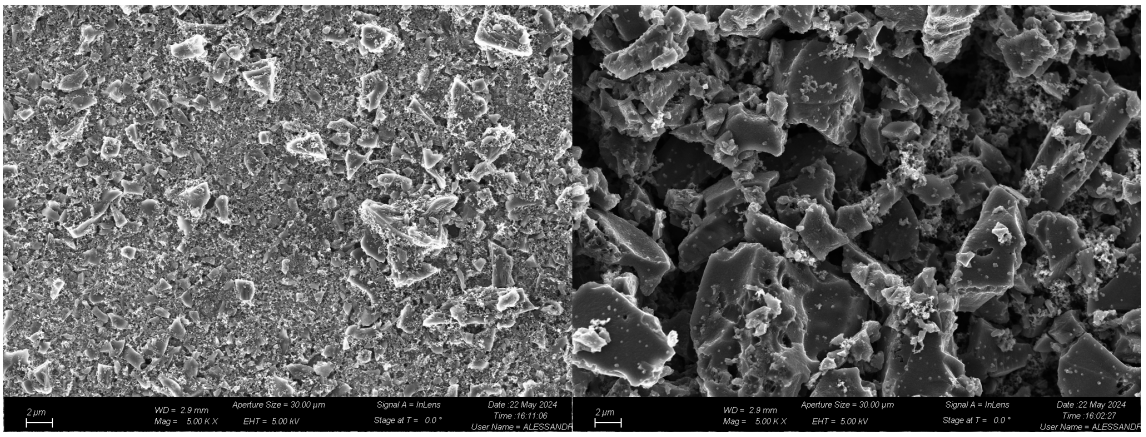

Figure 3.27: SEM comparison of the aerogel slurry (on the left) and AC slurry (on the right) on a Ti current collector.

Furthermore, by cycling the aerogel slurry at even lower scan rates (0.1, 0.2, 0.5 mV/s), an unexpected trend arose (**Fig. 3.28**). Since the charge accumulation is fast in EDLC electrodes (w.r.t. faradaic ones), slowing the process under a certain threshold doesn't result in a capacitance increase, because the charge accumulation mechanism in the double-layer electrode is already exhausted. In this case instead, we observed an increased ability in charge holding; following the example of [40], we analyzed the measured curves to find the diffusive and capacitive components

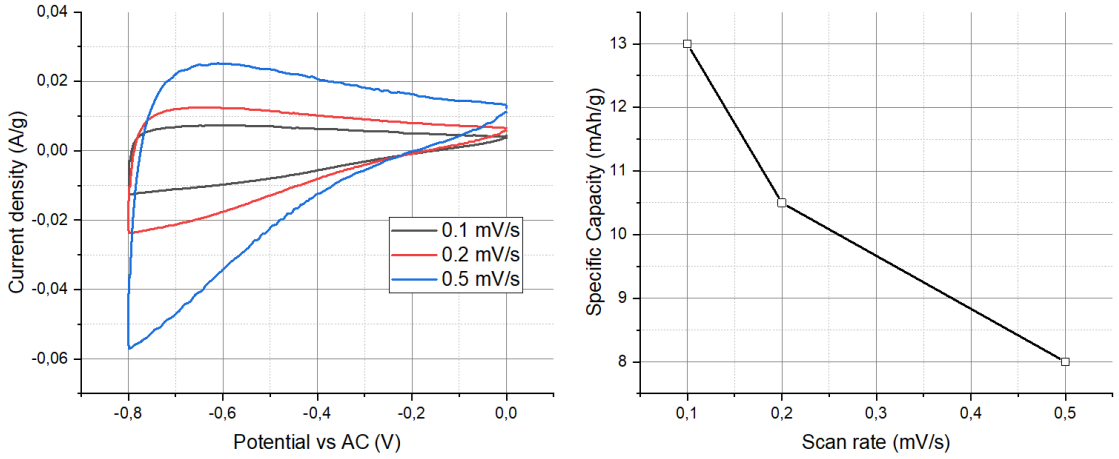

Figure 3.28: Aerogel slurry slower CVs visualization, with capacity estimation based on scan rates.

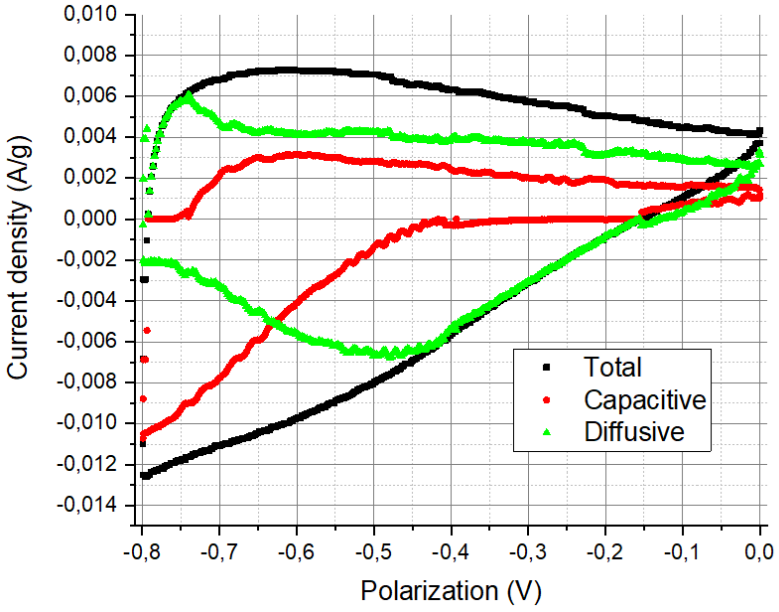

Figure 3.29: Detail on 0.1 mV/s CV, with different current contributions highlighted.

of the total current (**Fig. 3.29**). Although sometimes the fit is not reliable, the diffusive trait dominance is evident and causes the increase in capacitance. Since in theory the device (in its final application) would charge very slowly, this is not that bad, but it wouldn't be efficient in the discharging phase when the powered sensor (or other device) requires more current (in the case of a short but power-demanding

task for example). Once more material was produced, ball milling was the solution of choice to try and solve the homogeneity problem, hoping to also see an increase in capacitive behavior of the material.
To conclude, PEIS results from the ESW search are shown in **Fig. 3.30**, R_{ESR} is pretty low as usual, same goes for the charge transfer resistance, which is typical in carbon-based compounds. A less than ideal capacitive behavior is reported at low frequencies.

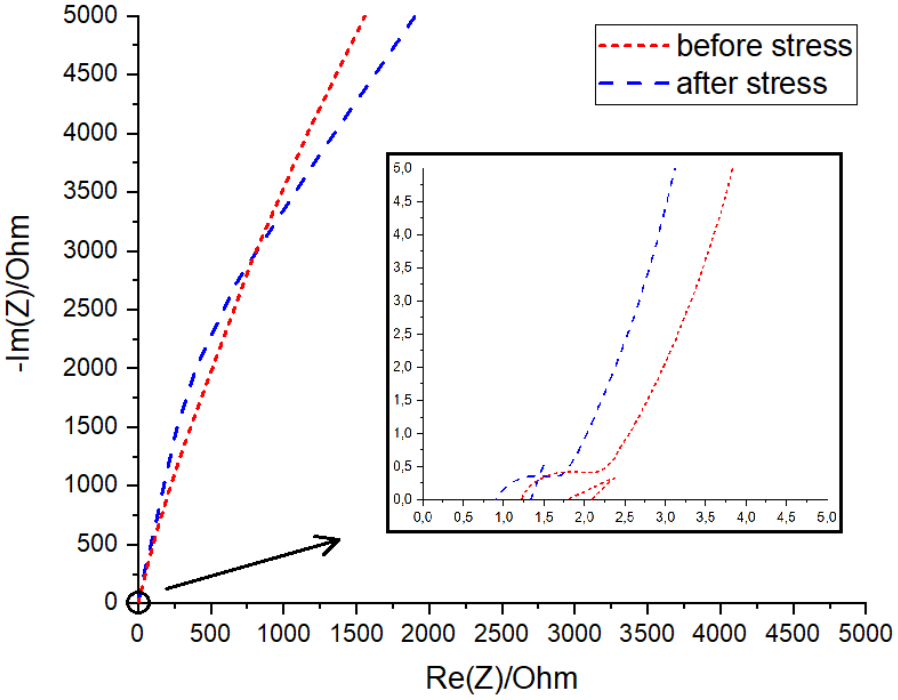

Figure 3.30: GELCBHPC-85105 Nyquist plot at OCP in Li_2SO_4 2M, with detail on high frequency.

3.4 Ball-milled (BM) aerogel performance

It wasn't possible to find good references in literature for ball milling carbon aerogels, or at least not something that was easily reproducible with the means at our disposal. Generally speaking, zirconia seemed like the most common milling material, along with a high balls to compound ratio [33, 11, 51]. Therefore, 2–mm diameter zirconia balls were put inside the milling tank with 300 mg of carbon aerogel, with a mass ratio of 32:1. To avoid any reaction from happening inside the tank while milling, the container was always closed inside a glove box filled with nitrogen. The sample was left milling for a total of 90 minutes at f45, which should correspond to 2700 rpm.

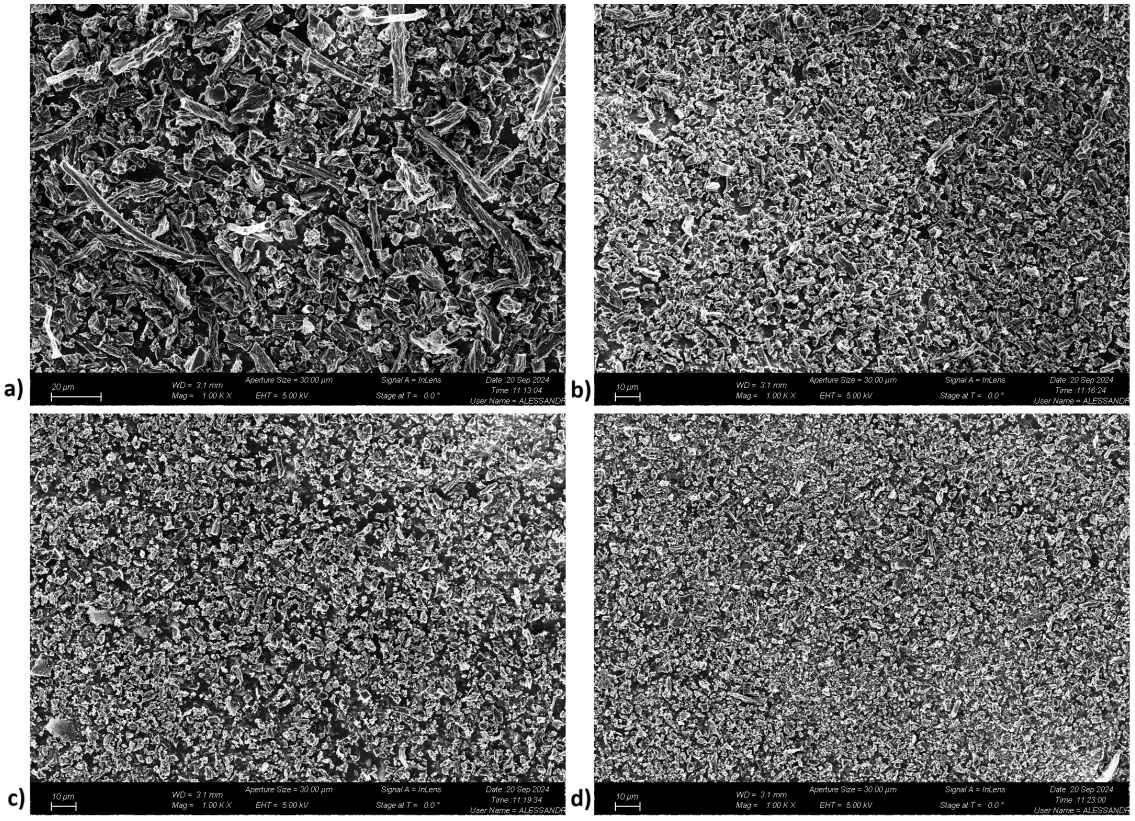

Figure 3.31: SEM images of the BM–aerogel after (a) 10 minutes, (b) 30 minutes, (c) 60 minutes and (d) 90 minutes.

Samples were collected during the procedure after variable time periods, also because heat generation can be a problem at high rotational speeds, and some time to cool off was considered between every interval. The different samples, collected after 10, 30, 60 and 90 minutes of ball milling (referred to from now on as BM10, BM30, BM60

and BM90), were analyzed using the FESEM, to see if there was a considerable difference w.r.t. aerogel pulverized with mortar and pestle but also to evaluate if the general homogeneity of the powder was any better. Results are shown in **Fig. 3.31**. With a rapid examination, it is possible to see a considerable improvement in size uniformity in BM30, with sub-μm dimension showing up in BM90. Reducing the size of the particles too much is not desirable since it could lead to a potential decrease in surface-to-volume ratio: for example, YP-50F has a mean particle size of more than 5 μm [18]. This, combined with the fact that traces of zirconium were found following an EDX spectroscopy of BM60 and BM90(0.1 wt% and 0.3 wt%, respectively), led us to think that ball milling for more than 30 minutes with these parameters is not beneficial. Unfortunately not enough material was available for experimentation, therefore BM90 will be used as the active compound in the new aerogel slurry.

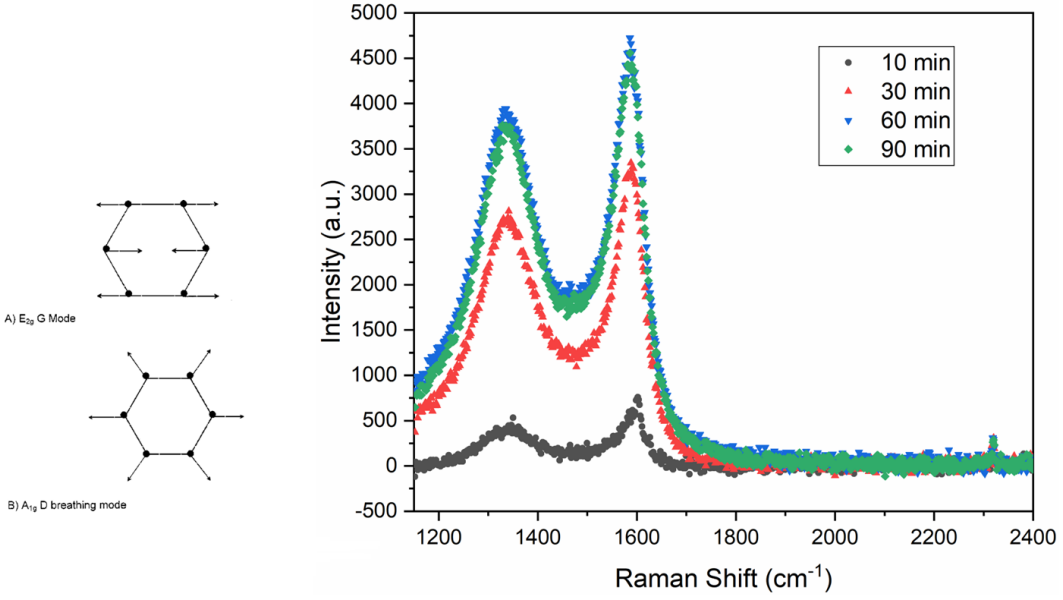

G - Graphite 1580 cm^{-1} E2g in plane vibration
D – Disorder 1360 cm^{-1} A1g in plane breathing
(inactive in large single crystals like in HOPG) due to the presence of disorder in parts like grain edges [39].

Figure 3.32: On the left carbon motions of the (a) G and (b) D modes [39], on the right the Raman spectra of the various samples of BM-aerogel.

To better understand the changing properties of the obtained powder the samples were also analyzed through Raman spectroscopy **Fig. 3.32**. Raman spectroscopy is a valuable tool for characterizing activated carbons and their structural changes. The spectra typically feature prominent G and D bands, with additional peaks identified

through deconvolution techniques ([35]; [7]) (**Fig. 3.33**). These bands provide insights into the carbon's structural order, with the D-band width correlating well with disorder across various carbon materials ([7]). Raman spectroscopy can detect structural changes during carbon activation processes, showing good correlation with XRD results for crystallite size measurements ([31]).

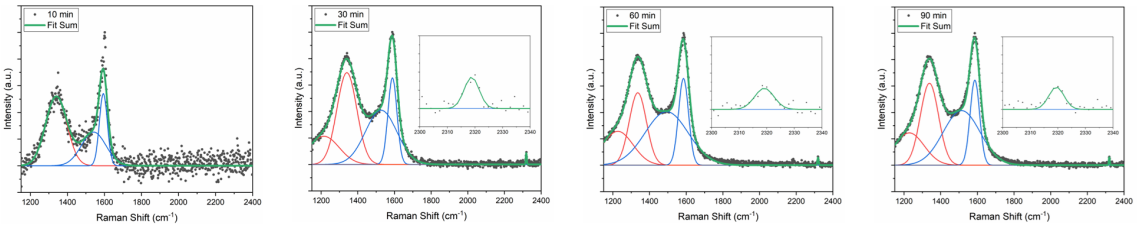

Figure 3.33: Analysis of the peaks in the various samples.

Sample		1D	2D	1G	2G	N	ID/IG
10 min	Height	394.1587	--	411.2049	191.9851	--	0.716
	Pos. [cm^{-1}]	1339.927	..	1594.099	1541.96	--	
	HWHM [cm^{-1}]	67.55822	--	25.29469	77.60099	--	
30 min	Height	2319.639	712.4571	2189.522	1370.395	288.6636	0.8207
	Pos. [cm^{-1}]	1340.38	1215.837	1588.955	1527.324	2318.766	
	HWHM [cm^{-1}]	63.88481	96.9151	28.81312	100.8914	3.186295	
60 min	Height	2592.172	1212.906	3105.447	1915.561	275.0241	0.8599
	Pos. [cm^{-1}]	1336.13	1227.494	1585.191	1493.162	2319.108	
	HWHM [cm^{-1}]	55.22303	97.31277	32.0713	138.2229	4.101886	
90 min	Height	2831.559	1116.585	2940.114	1886.664	280.2423	0.8357
	Pos. [cm^{-1}]	1338.716	1229.18	1586.236	1514.122	2319.462	
	HWHM [cm^{-1}]	58.61658	94.88784	30.54941	118.5166	3.253171	

Table 3.1: Position, height and HWHM of the peaks after different milling times.

Table 3.1 and **Fig. 3.34** report the results of the carried out analysis. The position of the 1G does not correlate with milling time nor with HWHM, if one accounts for the all milling times. The sample ball-milled 90 minutes returns results out of trends. On average, the 1G position is 1588 cm-1 and the upshift with respect to pure graphite (1580 cm^{-1}) can be attributed to the size effect of the basal plane. Hence, the G1 and D1 peaks are associated with winding short basal planes, and are, respectively, ascribed to the in-plane stretching (like E2g) and breathing (like A1g) vibration modes from the basal planes. G2 and D2 peaks are ascribed to sp2

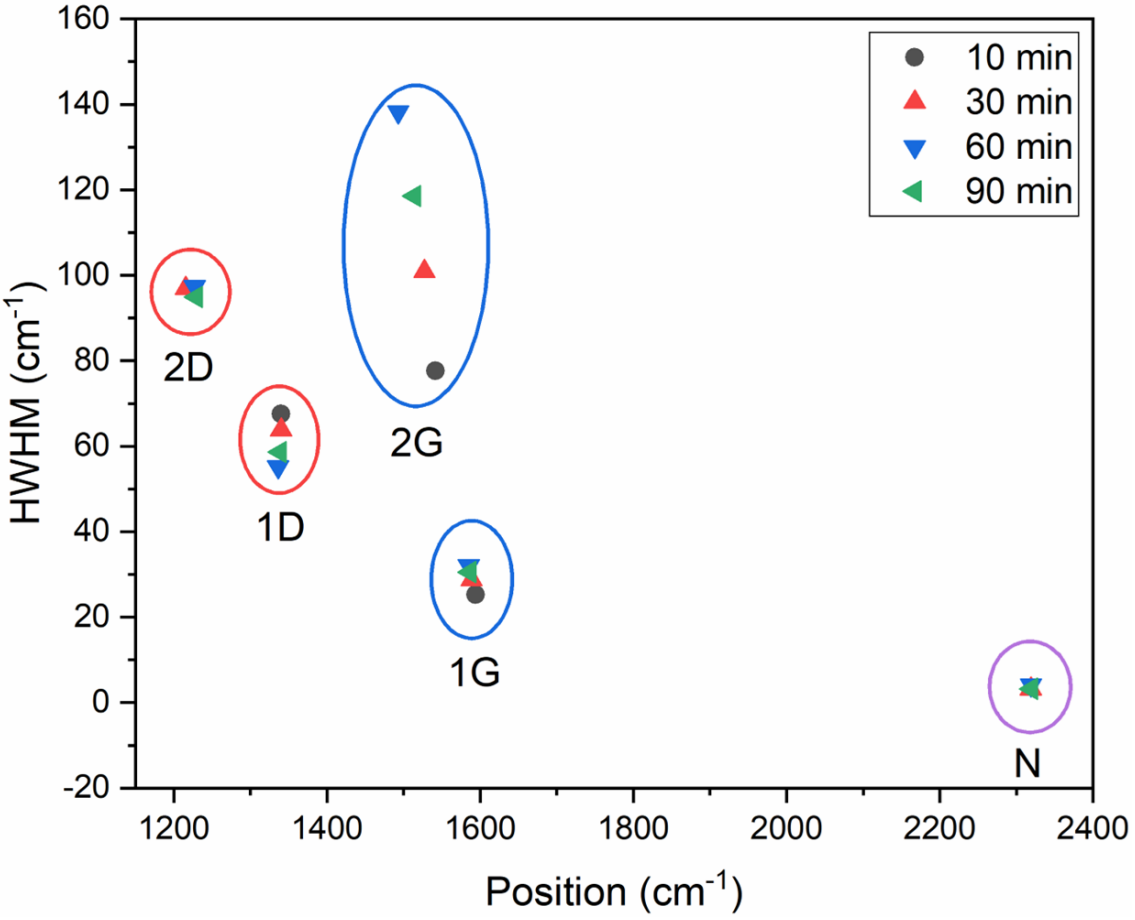

Figure 3.34: Position shift of the measured peaks.

clusters like amorphous carbons with bond angle disorder including more fourfold coordinated bonds than amorphous carbons. The sensible changes in 2G mode suggest a reduction of graphitic domain sizes leading to a more amorphous phase. Similar trends were found by the group of Yuan et. al., in which activated carbon powders were milled up to 24h and more [46]. They observed significant reduction in the carbon property after one hour of milling. Our results partially reflects the ones provided by Yuan and co-workers. Defectiveness evidenced ad both Id/Ig or Ad/Ag ratios increases with the milling time as well as 1D HWHM decreases. The N peak is attributed to the presence of N functional groups in the carbon matrix, coming from the carbon precursors [47].

For what concerns the mixture used to obtain the electrodes, it is composed by 100 mg of crushed aerogel (85 wt%), C65 carbon black (10 wt%), and HPC (5 wt%), in 0.6 mL of DIW. Since the compounds are the same, no additional CVs to find the

ESW were done, assuming it fixed on 0.8 V; instead several cycles at slow scan rates (up to 1 mV/s) were executed to see if the I-V curves were improved by ball milling.

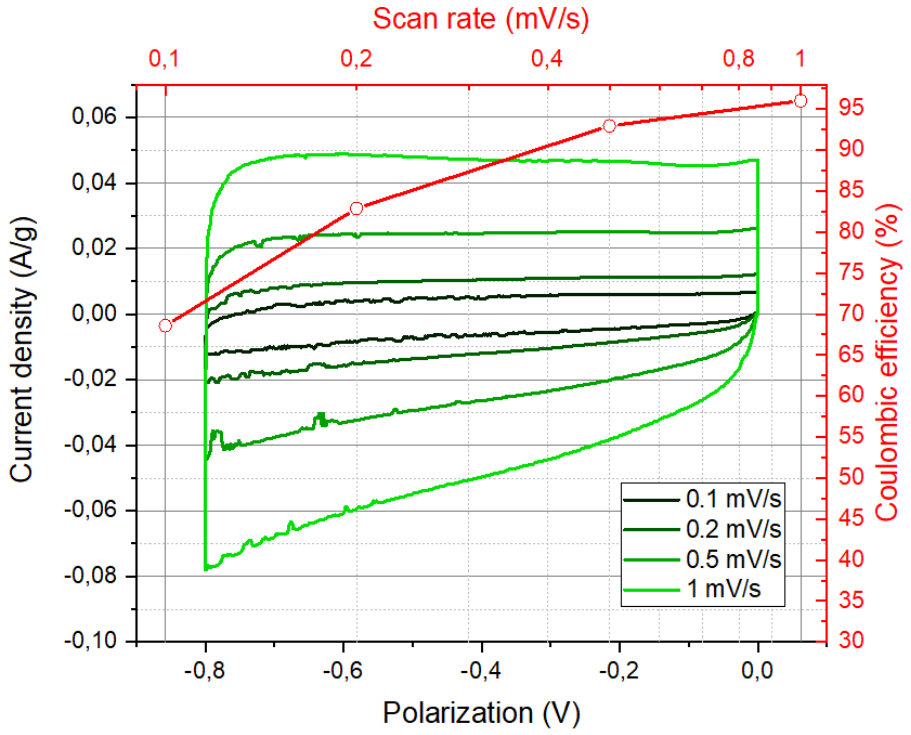

Figure 3.35: Slower CVs executed on the ball milled aerogel, the coulombic efficiency is calculated on the last cycle at that scan rate; only 5 cycles each were performed.

The shape of the curve itself is already indicative of a better capacitive behavior, and the resulting capacitance results far more stable during cycles at different scan rates: values are around 10.5 mAh/g, which is overall less than the maximum obtained with the non-BM aerogel (more than 13 mAh/g, but only for 0.1 mV/s). In **Fig. 3.36**, the diffusive and capacitive currents calculated for the 0.1 mV/s curve are reported.

These results are probably a consequence of the aerogel's lack of a dedicated activation step. Nanometric porous carbon structures generally need a chemical o physical activation phase during their synthesis to achieve the superior surface-to-volume ratio that results in great storage capabilities [1]. Since there isn't one in the aerogel procedure, the surface of the material is not as much developed as it could be, causing resistive traits that are progressively lowered by increasing the overall surface area, that is what probably happened when the aerogel was ball milled.
To conclude, the BM-aerogel was subjected to a float test, in a procedure similar to the one adopted in the LMO case (**Fig. 3.37**). The values of capacitance are

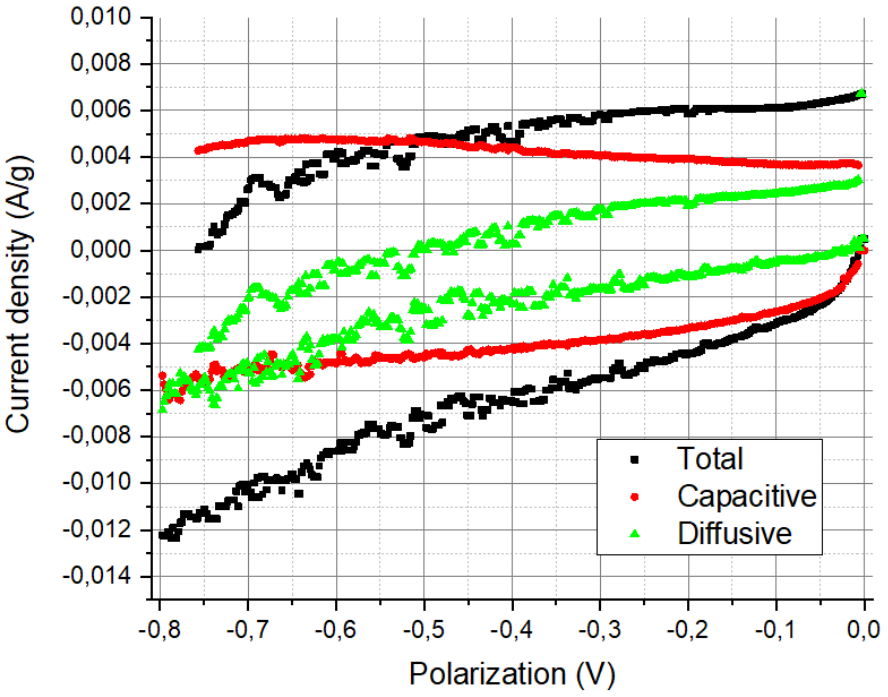

Figure 3.36: Diffusive and capacitive contributions to the total current in the 0.1 mV/s scan; the capacitive behavior seems dominant in this case.

in accordance with the previous scans operated (**Fig. 3.38**); but while coulombic efficiency grazes 100% (values over it are just products of tolerances), the calculated energetic efficiency is much lower, around 80%, meaning resistive contributions within the device are still too high. The leakage current was measured to be around 1 μA, corresponding to roughly 2 mA/g. From the PEIS procedure operated after every third cycle we can see the properties of the compound have not changed (**Fig. 3.39**).
Overall, just looking qualitatively at the comparison between the two approaches in **Fig. 3.40**, it is evident capacitive behavior of the sample has been boosted, although its limitations compared to activated carbon YP-50F remain obvious.

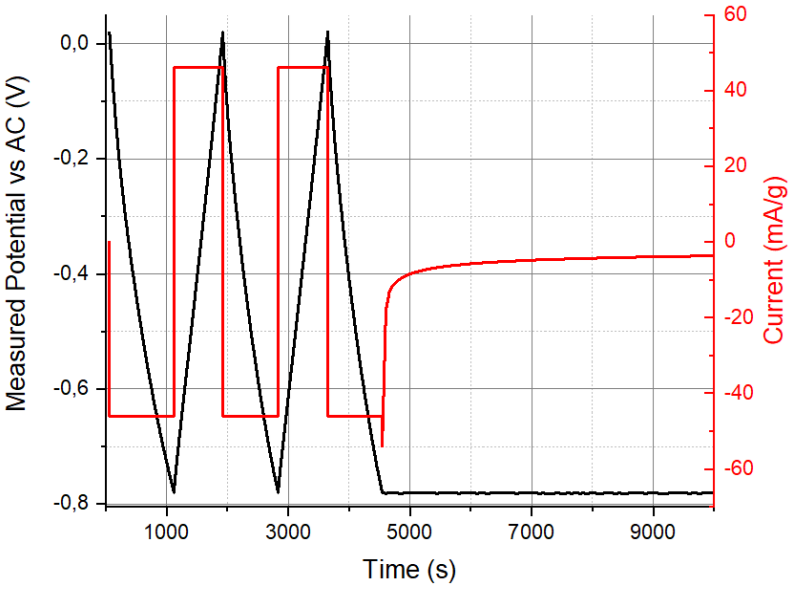

Figure 3.37: Detail on the float test procedure for the BM-aerogel; the current is comparable with C/10 rates of LMO.

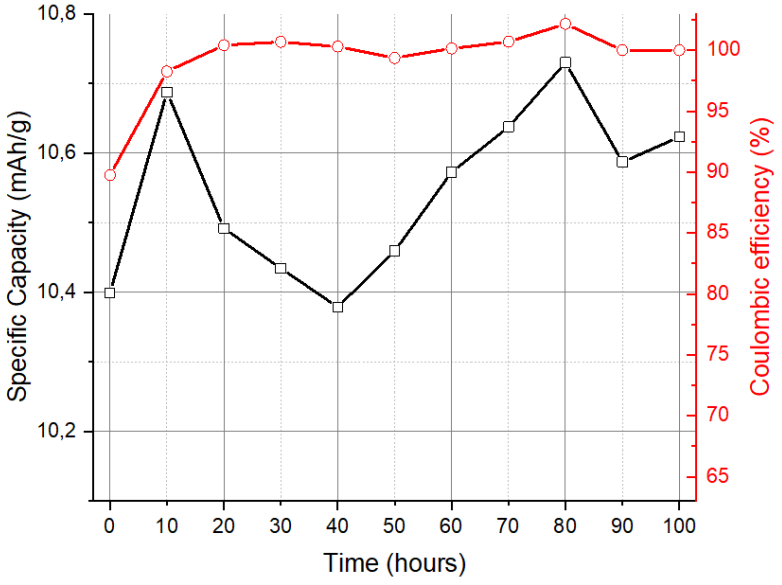

Figure 3.38: Capacity and coulombic efficiency at the start of every potential hold (10h).

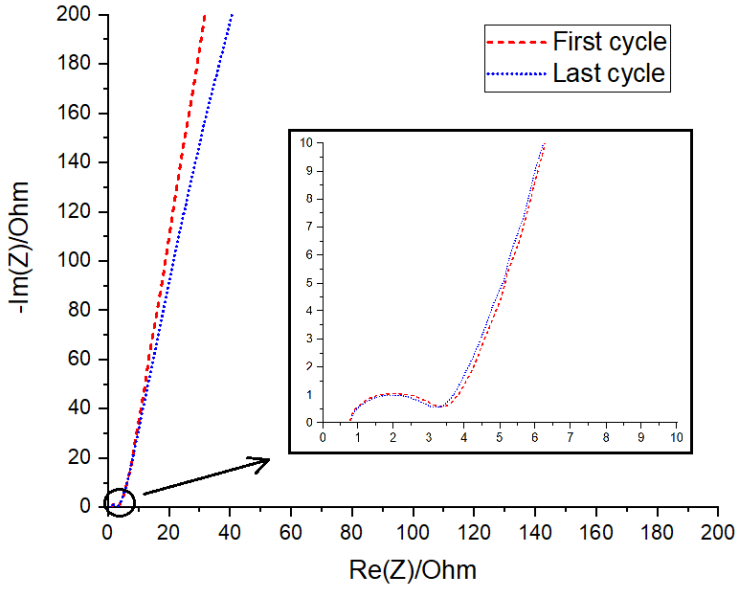

Figure 3.39: GELCBHPC-85105 Nyquist plot at OCP in Li_2SO_4 2M, with detail on high frequency.

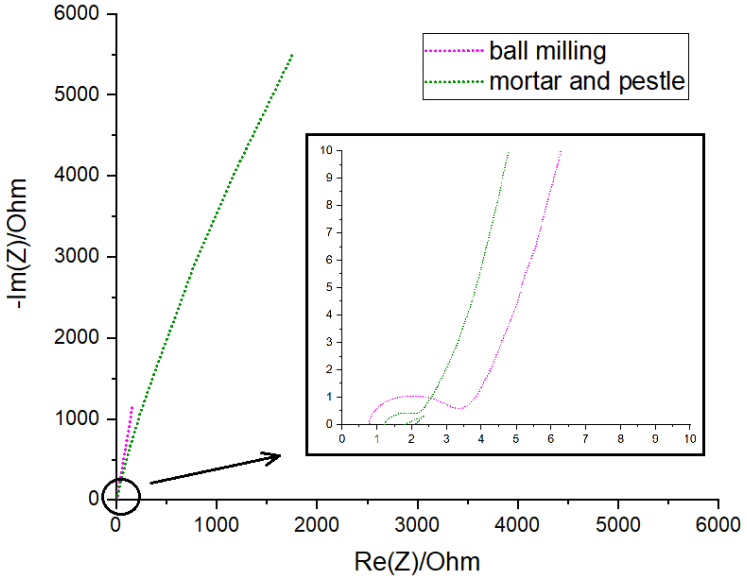

Figure 3.40: The two aerogel Nyquist plots are here presented, frequency range is equal for both. The samples have different mass loading (M&P: 1.12 mg, BM: 0.5 mg) and both the lower impedance and steeper slope at low frequency suggest an improved behavior of the porous carbon after ball milling.

3.5 Assembled devices

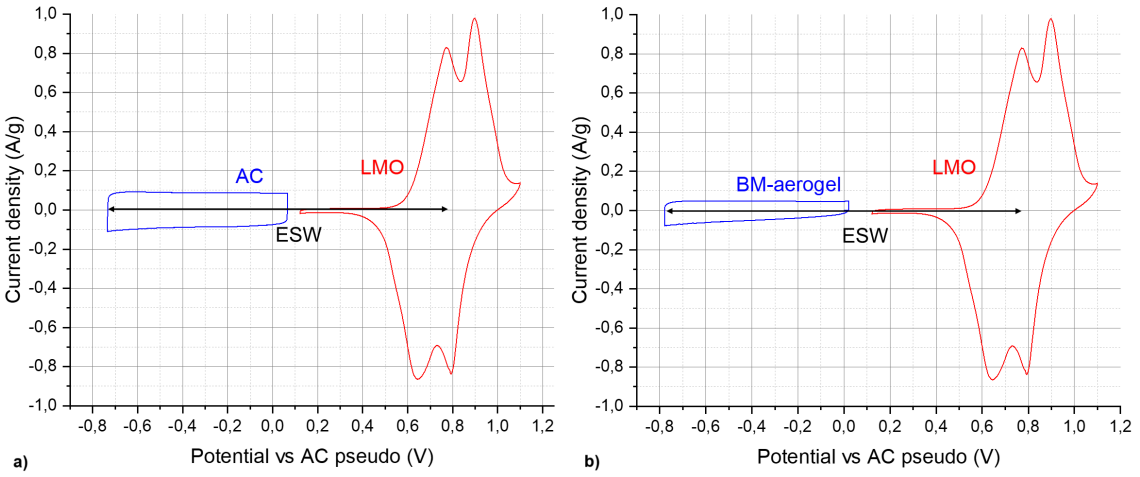

Figure 3.41: Combined electrochemical stability windows of (a) AC/LMO (b) BM-aerogel/LMO.

Two devices containing the chosen active compounds were assembled, one using BM-aerogel, the other exploiting YP-50F, both combined with $LiMn_2O_4$ as the battery-like electrode. The expected capacity for each electrode is reported in **Tab. 3.2**. Since these have to match in order to accumulate the same amount of charge on both ends, mass balancing is needed. For what concerns the aerogel, it was impossible to recreate a 4:1 mass ratio, but the device was set up anyway, while being unbalanced, despite the limited performance. For the YP-50F/$LiMn_2O_4$, after some time, it was possible to combine a 2.95 mg AC electrode with a 1.5 mg faradaic one, coming close enough to the 2:1 ratio needed. As highlighted in **Fig. 3.41**, the ESW of the electrodes has no intersection, meaning the OCP of the assembled devices won't be 0, also note that the potential window does not include both LMO peaks.

Active compound	**Capacity (mAh/g)**
Aerogel	10.6
YP-50F	19.4
$LiMn_2O_4$	42.5

Table 3.2: Capacity of the tested compounds.

3.5.1 Using BM-carbon aerogel powder

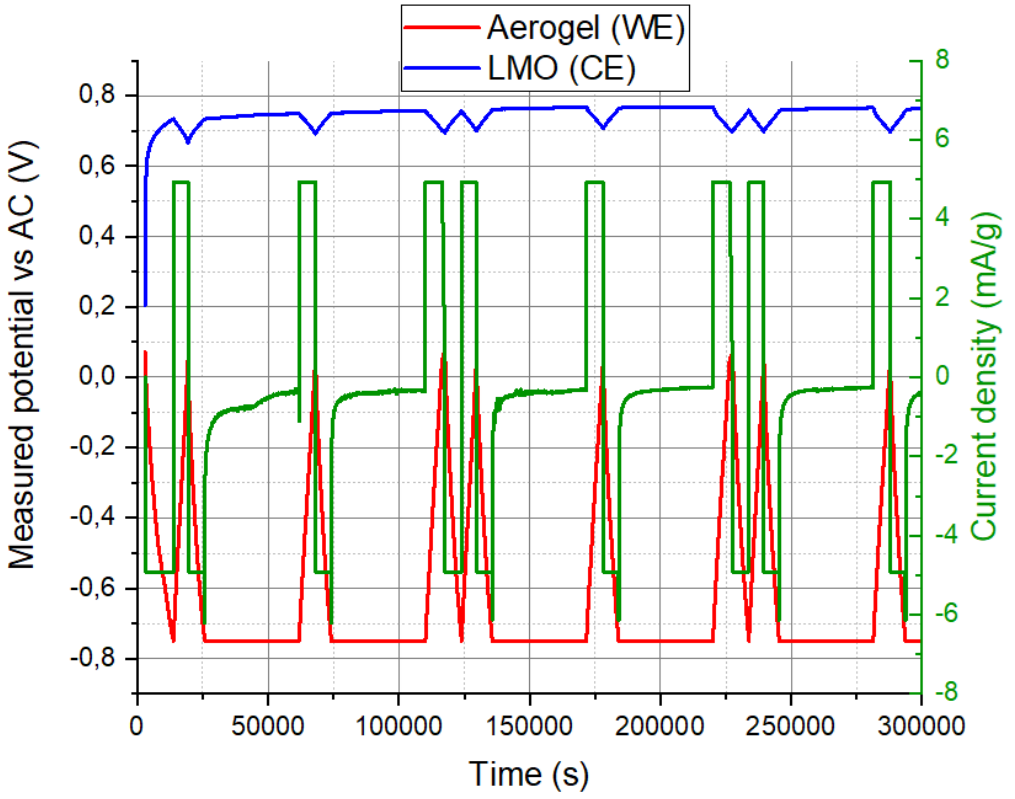

Figure 3.42: Detail of the float test executed on the aerogel/LMO device.

A BM-aerogel electrode with 1.37 mg mass loading and a 1.22 mg LMO electrode were put together inside a Swagelok cell for a float test. The parameter extraction from this experiment serves as a solid starting point for evaluating the performance of the device with YP-50F. To better visualize the processes happening at the device terminals, the measurement was done in 3-electrode configuration, imposing a maximum voltage difference on the carbon side equal to 0.8 V. **Fig. 3.42** shows the potential at WE and CE as well as the current applied during the whole procedure. Because of the faradaic working mechanism, once the side reactions at the carbon side are exhausted, the LMO potential tends to remain around its first redox peak, possibly accumulating more charge when the maximum potential is held for long. In fact during the first voltage hold, the mean current is higher than the following ones, with a visible drop around half of the period. This results in a not-fully discharged device; further release of charge would force the equivalent of a positive potential application to the device's carbon side, with the risk of unwanted irreversible reactions. Aside for some drifting in the curve, the difference between WE and CE

potentials results in a limited voltage excursion, as can be seen in **Fig. 3.43**.

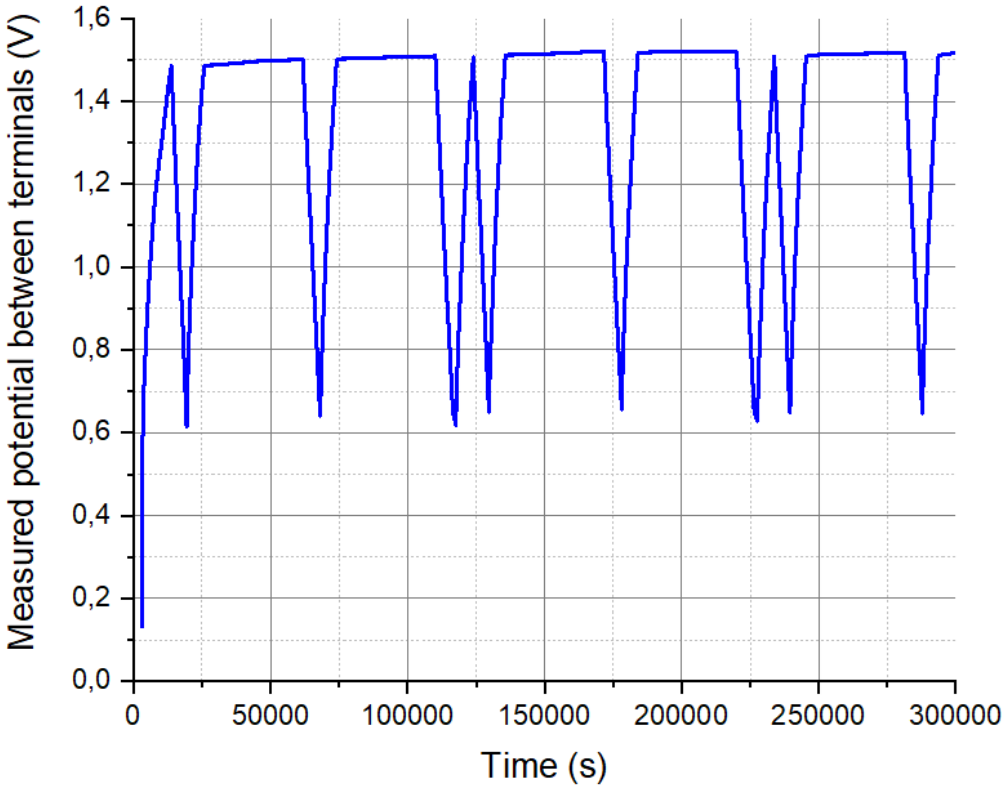

Figure 3.43: Voltage excursion between device's terminals, after the first cycle, the total swing is reduced.

The estimated capacity of the device is around 7.7 mAh/g, with higher peaks of 8.7 mAh/g following a long potential hold, while the η_{energy} for the combined operation of the two compounds is 76%. The leakage current has a decreasing trend over the various cycles, going from 1 μA to 500 nA (385 to 192 μA/g). Because of the residual charge that is left in the LMO after the first cycle, the early Nyquist plots show some differences in the high to mid frequency region (**Fig. 3.44**), with a visible inductive behavior (positive imaginary impedance).

A final GCD in 2 electrode configuration was performed at different current rates: a total of 24 cycles were performed, 2 cycles at 5 mA/g and 10 mA/g, and 5 cycles each at 20, 50, 100, and 200 mA/g. No potential holding between cycles was carried out. This was done in order to obtain the Ragone plot shown in **Fig. 3.45**. It's important to mention that this test was carried out with a device assembled with another pair of electrodes (aerogel mass: 1.47 mg, LMO mass: 1.56 mg). As we can

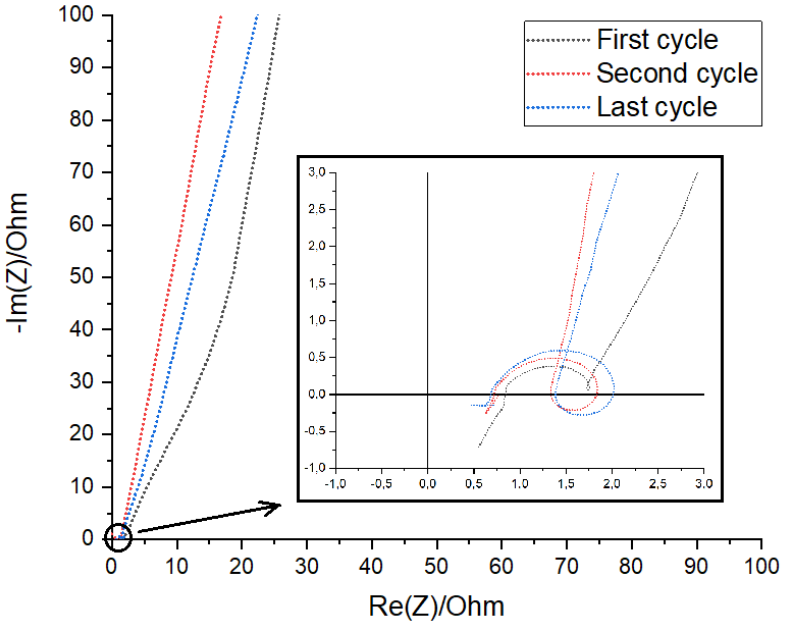

Figure 3.44: Nyquist plot of the float test cycles, with detail on the high to mid frequencies.

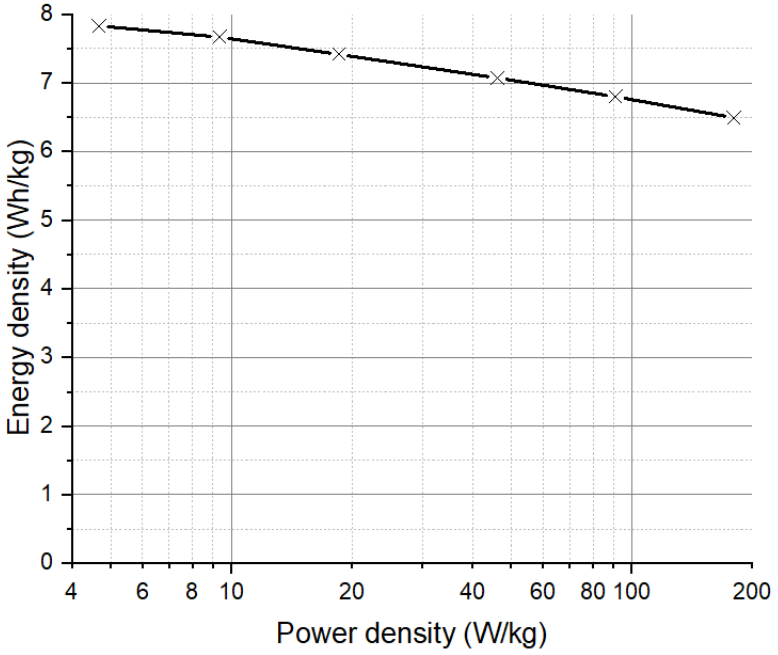

Figure 3.45: Ragone plot of the BM-aerogel/LMO combination.

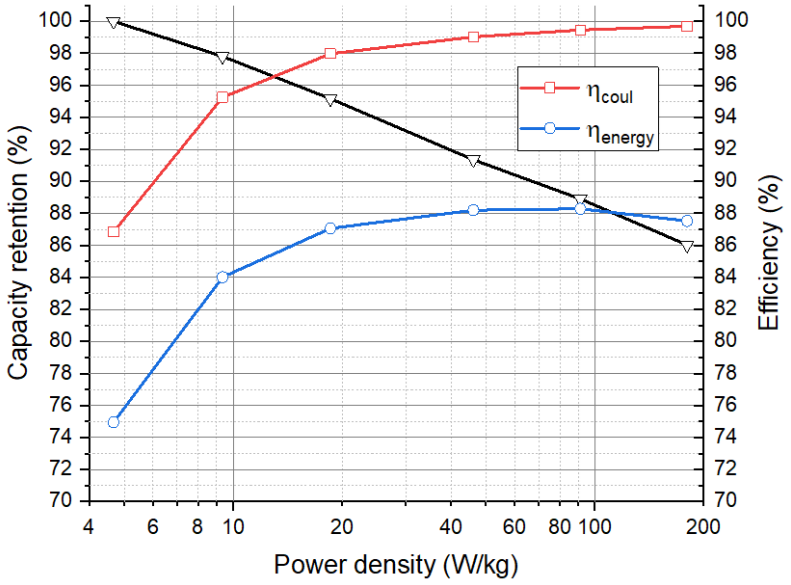

Figure 3.46: Efficiency and capacity for each current rate, reported for the resulting power density.

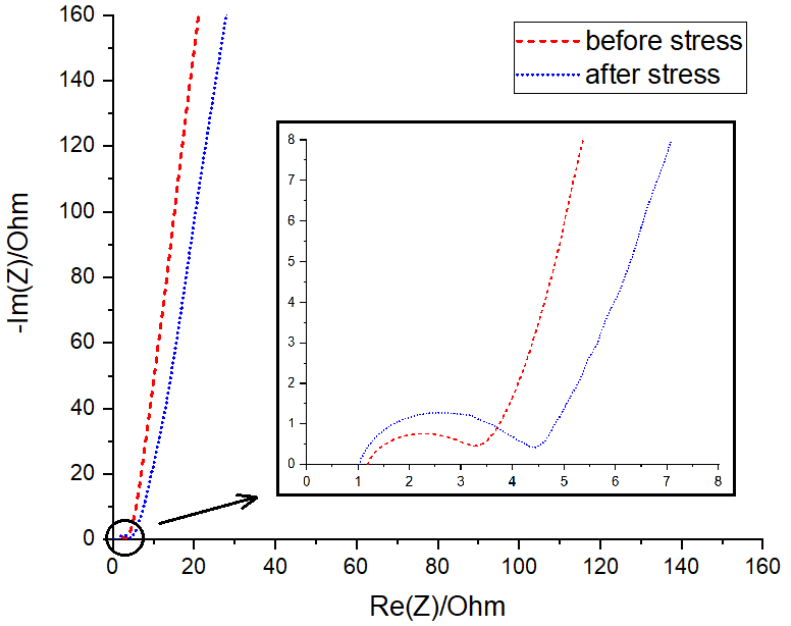

Figure 3.47: Nyquist plot of the cell before and after the GCD to obtain the Ragone plot; although modifications are similar to what was seen previously, no trace of inductive contribution is present.

see from **Fig. 3.46**, the data substantially matches the already obtained one (if we consider it wasn't cycled before), with faster current rates yielding higher η_{coul} and η_{energy} values, while a decrease in capacity due is observable as well.

It is interesting to see that despite the charge unbalance, the Nyquist plot does not show the same frequency behavior transformation: either the cause is the potential hold during the float test, or something was wrong with the former setup.

3.5.2 Using activated carbon YP-50F

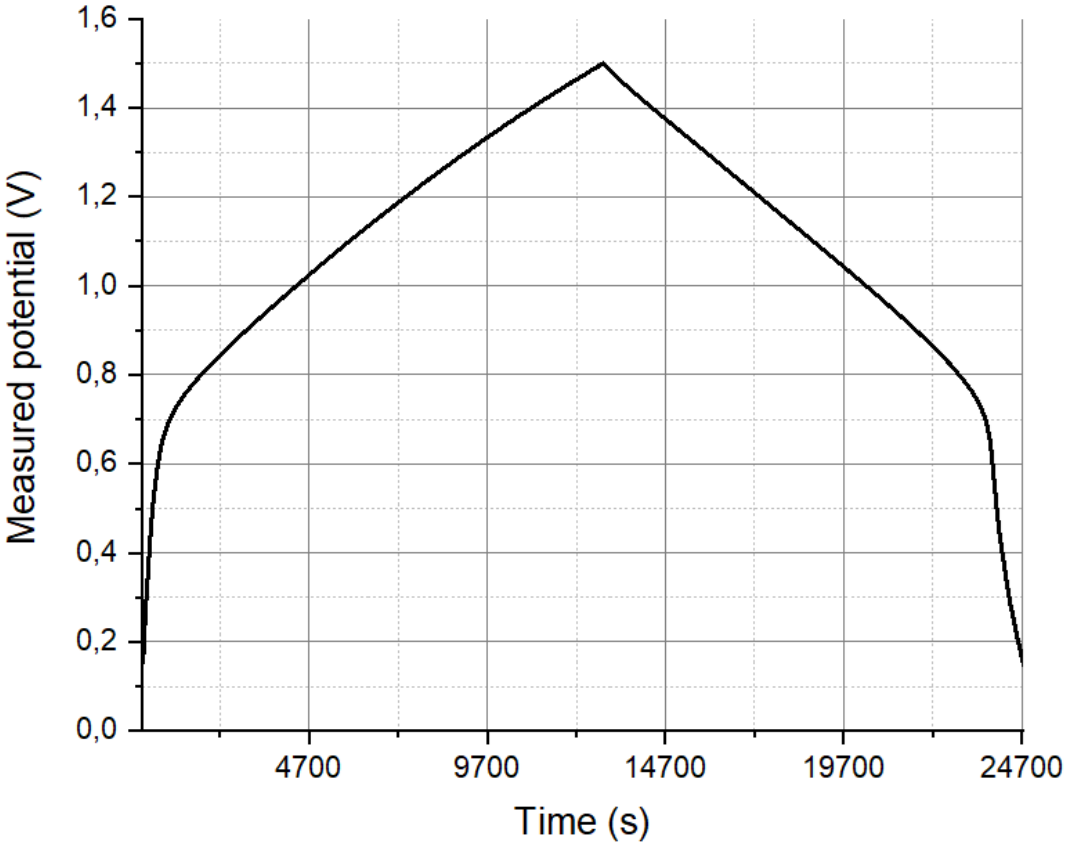

Figure 3.48: Detail on the measured potential over a single charge/discharge of the device, currents are always chosen to simulate solar generated current.

Finally an AC/LMO device was assembled with the mass loading mentioned at the start of the section; a float test was executed again, this time exploiting a 2-electrode measurement. As we can see in **Fig. 3.48**, the shape of the potential curve is exactly what we expected; there is a very fast voltage increase at the start of every charging period, which has a flatter slope once the redox peak of the faradaic compound is reached; the inverse trend is visible for the discharging period. The full voltage swing is applied, starting from the OCP measured at the start of the procedure (144 mV). The non-zero voltage at equilibrium is an unfortunate result of the two materials not having an intersection interval in their ESW, thus losing some charge that could be accumulated from 0 V to OCP, while also raising some concerns for the DSSC integration.

The leakage current is around 1 μA, corresponding to 333 μA/g. The η_{coul} shows a

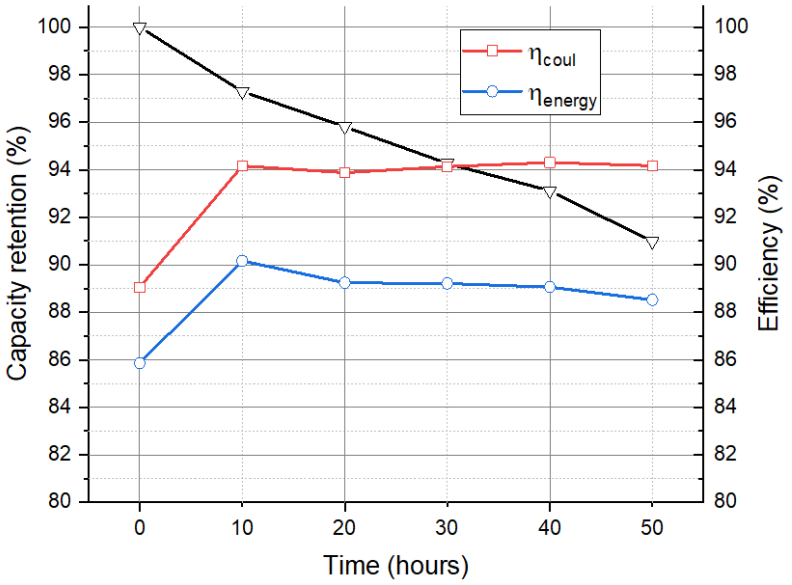

Figure 3.49: Efficiency and capacity retention at the start of every potential hold (10h).

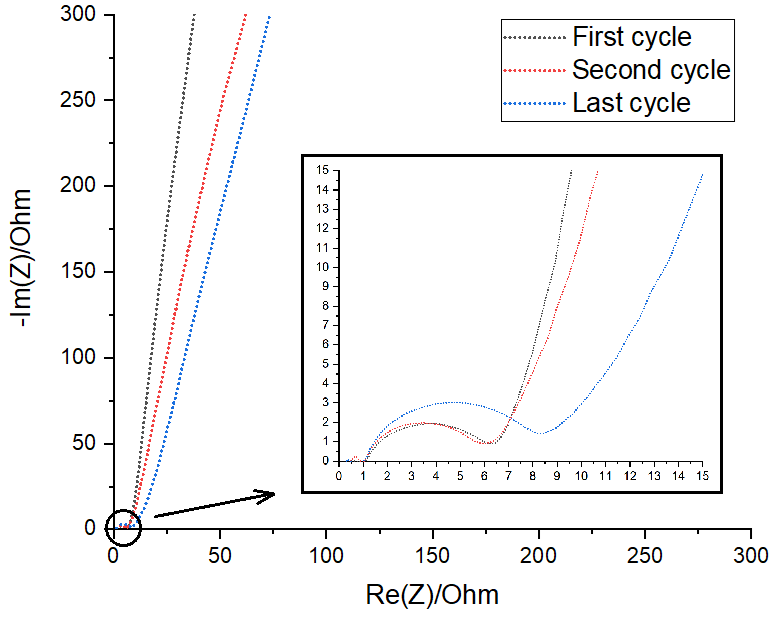

Figure 3.50: Nyquist plot of the float test cycles, with detail on the high to mid frequency.

good trend, with peaks around 94%; the reduction in efficiency vs single electrode characterizations can be attributed to a couple of factors, the former being that the faradaic electrode has not the same performance as a porous carbon one (in terms of η); while the latter could be due to some residual charge left in the system. This can be the cause of the increase in OCP after the procedure (370 vs 144 mV), an outcome that was observed also in the case of the BM-aerogel/LMO device. Energetic efficiency grazes 90%, and the capacity values between cycles can be seen in **Fig. 3.49**. A detail catches the eye more than anything else: there is a decreasing trend in capacity, confirmed by the aerogel float test and a similar one performed in a AC/LMO unbalanced cell. The stability of the single compounds has been tested thoroughly in their respective sections, showing a constant, if not increased capacity due to successive activation of porous sites after the first cycles. This fact coupled with the aforementioned change in OCP, leads us to believe that there is some undischarged energy left in the cell; further investigations should be made repeating the process while being able to monitor bot WE and CE potentials (3-electrode measurement). The Nyquist plot over the cycles is similar, and an increase in R_{ct} is visible (**Fig. 3.50**).

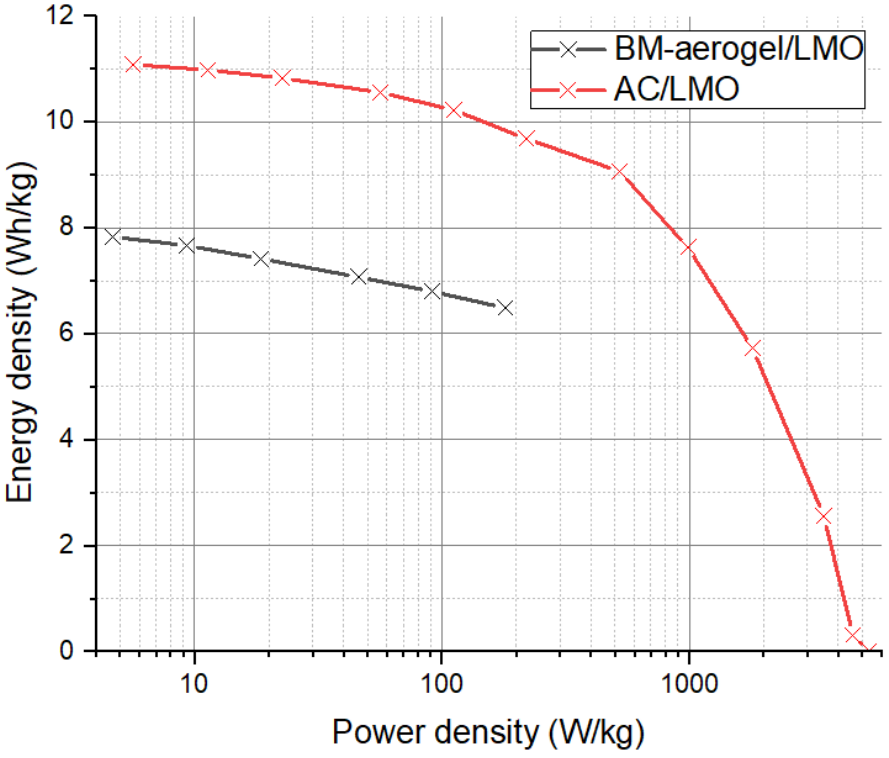

Figure 3.51: Comparison of the two Ragone plots obtained.

Lastly, a GCD similar to the one in **Sec. 3.5.1** has been performed, going much further in current rates. Other than the ones already specified, 5 cyles at 500 mA/g, 1, 2, 5, 10 and 20 A/g were tested. This time the device is the same of the float test, and the voltage excursion has been applied starting by the last (higher) open circuit voltage. The comparison between the two Ragone plots can be seen in **Fig. 3.51**.

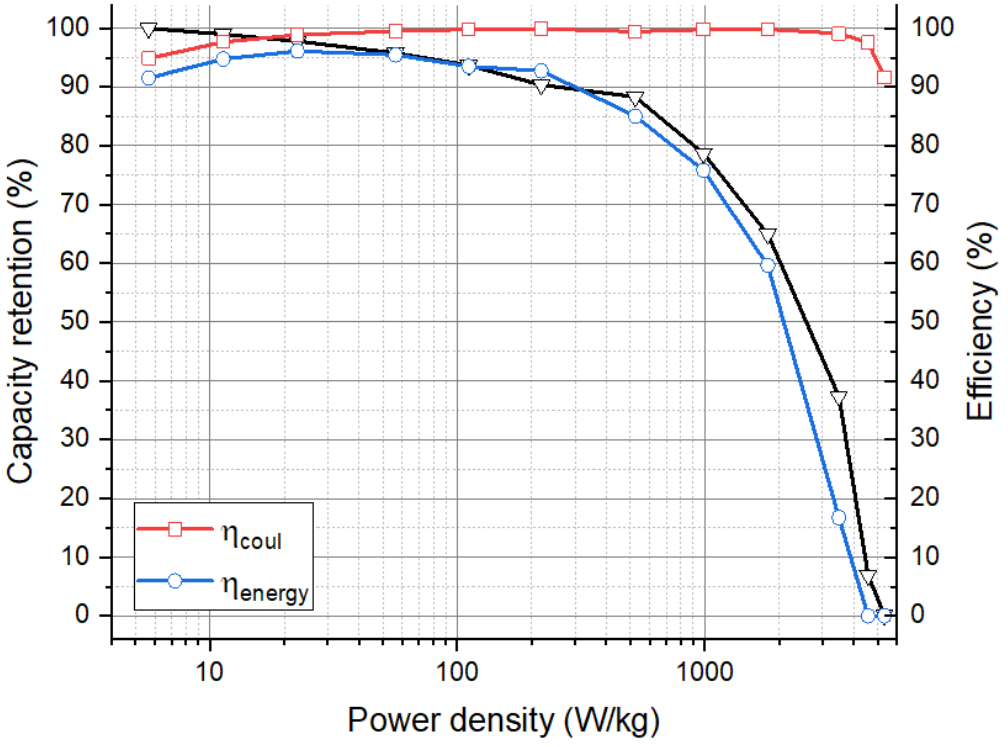

Figure 3.52: Efficiency and capacity for each current rate, reported for the resulting power density.

Similar trends and generally better efficiencies than BM-aerogel/LMO combination can be seen in the early part of **Fig. 3.52**, where a noticeable drop in η_{energy} starts from 50 mA/g. This is a result of the slower time constant of faradaic reactions on the LMO electrode; going back to the float test on the LMO (single electrode) **Sec. 3.2**, and calculating η_{energy} on the C rates, the procedure shows similar performance, with an increasing efficiency up to C (corresponding to about 50 mA/g in this case), where it starts decreasing because the compound lacks the needed time to accumulate all the charge it can store. This is slightly visible also in **Fig. 3.46**, but the overall lower efficiency masks a bit this behaviour. Another cause for this loss in efficiency is the series resistance of the system, whose contribution increases with current.

The Nyquist plot (**Fig. 3.53**) shows similar R_{ESR} for both aerogel and AC devices, thus discarding the hypothesis of a more visible loss because of different values of series resistance. For higher currents R_{ESR} dissipates more and more of the energy inserted in the system; note that for 10 and 20 A/g the reported values are less and less reliable, since the measurement is so fast the curve digital representation does not a good job approximating it.

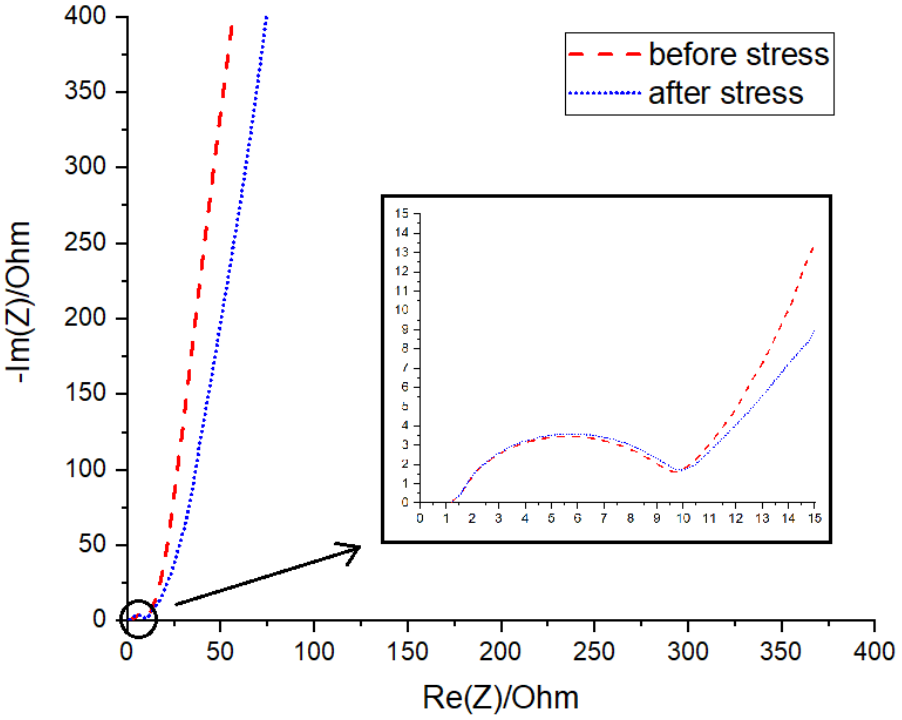

Figure 3.53: Nyquist plot of the cell before and after the GCD to obtain the Ragone plot.

The average gravimetric capacitance of the realized devices, together with single compounds estimations (only for Li_2SO_4 2M), calculated following two different methods, is reported in **Table 3.3**.

Although the results of the tests are satisfactory in their own way, the main reference for this project ([12]) achieves much higher energy than this work at low power densities (>30 Wh/kg for ∼180 W/kg). The reasons can be multiple and have yet to be investigated, but some considerations are reported here. First of all, while this work uses HPC as a binder for the carbon slurry, in [12] polytetrafluoroethylene (PTFE) is exploited, also Ni-grid is the chosen as current collector as opposed to Ti; the estimated ratio between capacities of the compounds is the same, but the calculated values are double the ones reported in this thesis (80 vs 40 mAh/g for

Material	Mass (mg)	Technique	C_s (F/g)
Aerogel	1.12	CV (1 mV/s)	12.84
Aerogel	1.3	CV (0.1 mV/s)	54.33
AC	4.34	CV (1 mV/s)	87.01
BM-Aerogel	0.5	CV (0.1 mV/s)	47.93
BM-Aerogel	0.5	Float Test (C/10)	48.73
AC/LMO (unb)	5 (1:1.37)	Float Test (C/10)	39.63
Gel/LMO	2.6 (1.23:1)	Float Test (C/10)	31.83
AC/LMO (b)	4.5 (2:1)	Float Test (C/10)	22.21
AC/LMO (unb)	5 (1:1.37)	GCD (5 mA/g)	28.55
Gel/LMO	3 (1:1.06)	GCD (5 mA/g)	18.13
AC/LMO (b)	4.5 (2:1)	GCD (5 mA/g)	23.27

Table 3.3: Experimental data for different materials and techniques.

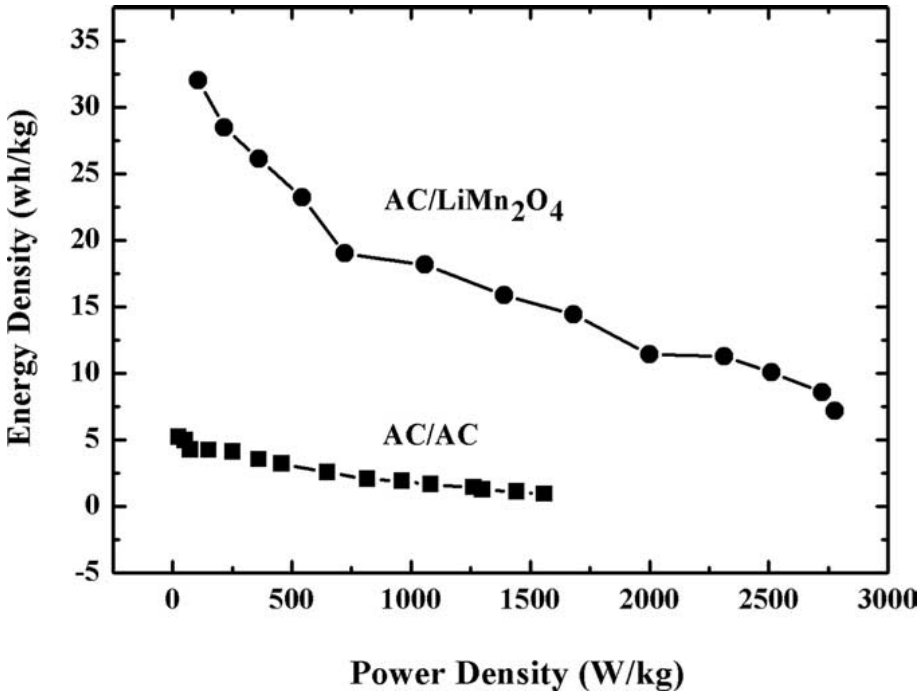

Figure 3.54: Ragone plot of the device developed in [12], compared with an asymmetric EDLC configuration (AC/AC).

LMO, 40 vs 20 mAh/g for AC); last but not least, the mass loading of the electrodes is much heavier in [12] (the mean value for most of the electrodes in this work is 1.5 mg, while in [12] it reaches 12/24 mg in 1 cm^2). All of these factors combined leads us to believe that the device assembled in Wang and Xia's work is more a three-

dimensional device than the one developed in this thesis; while achieving good energy densities at low power capabilities, we can see in **Fig. 3.54** that the performances are not that stable with increasing current rates; while this one seems to behave more steadily. This could be caused by the accessibility of the sites in a much larger volume, that would explain the difference in measured data while also not accounting for the change in binder having its own contribution.

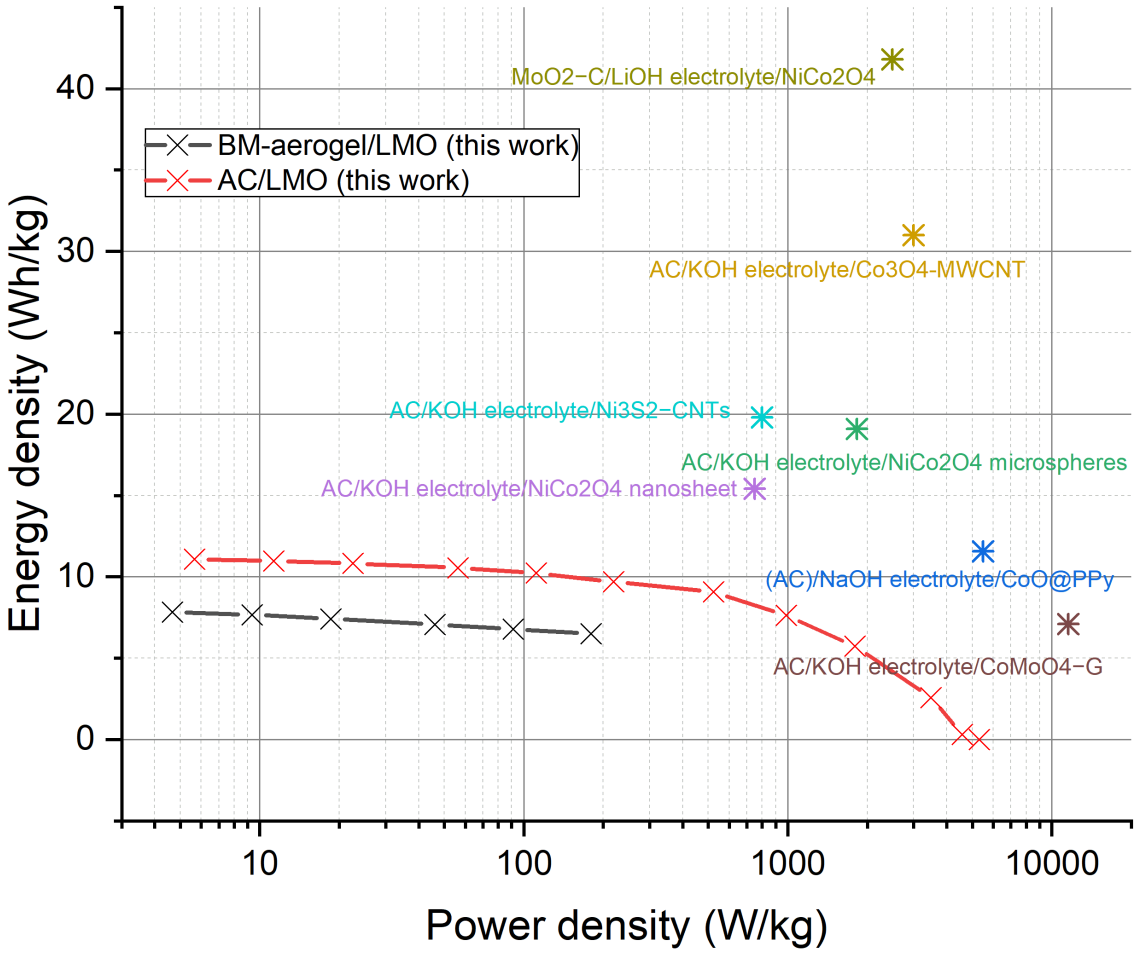

Figure 3.55: Ragone plot of this work compared with other devices extracted from [24].

Other work's experimental data [24] is plotted together with the work presented in this thesis for comparison (**Fig. 3.55**).

3.6 Carbon as counter electrodes in DSSCs

As porous carbons have been already tested in literature as alternatives for Pt–sputtered counter electrodes in DSSCs [22, 5, 21], a Tafel polarization measurement was carried out on the various compounds tested up to now. The experiment is done in a dummy cell configuration; this means two identical counter electrodes are put inside a Swagelok cell symmetrically in order to eliminate photoanode contributions and evaluate catalytic performance. They are separated by a thin glass fiber layer, imbued in a acetonitrile (ACN) electrolyte containing the redox couple I^-/I_3^-, which is the most used in DSSCs because it has been proven to have long term stability. The test consists in a brief voltage sweep between the redox potentials at the anode and cathode of the dummy cell, measuring the resulting current and reporting it in a logarithmic scale (**Fig.3.56**). Three distinctive zones can be identified:

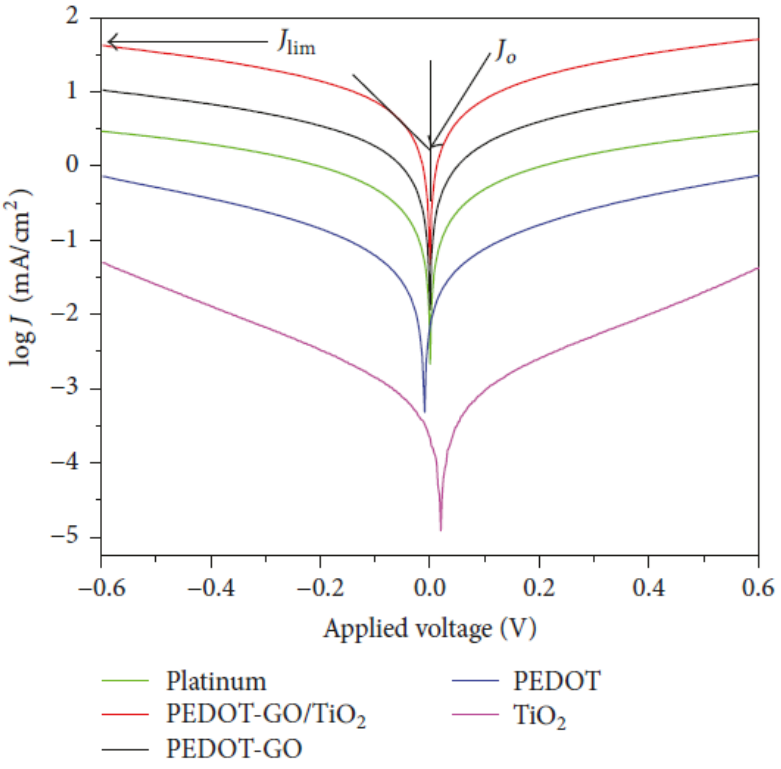

Figure 3.56: An example of Tafel plots executed on various compounds, reporting exchange current density J_0 and limiting current density J_{lim} [26].

- At low potential, there is the polarization zone;
- At an intermediate potential there is the Tafel region, which corresponds to the interval where the plot is well-approximated by the Tafel slope (visible

in semilog plots), a simplification of the Butler–Volmer equation that can be exploited for the individuation of the exchange current I_0 (or J_0 for current density), which is related to the catalytic activity of the electrode w.r.t. the chosen electrolyte.

- At higher potential there is the diffusion zone, where mass transfer conditions can limit the maximum current depending on the system (I_{lim} or J_{lim} for current density).

The exchange current I_0 can be expressed as follows:

$$I_0 = \frac{RT}{nFR_{ct}} \tag{3.2}$$

where R and F are gas and Faraday's constant, T is the room temperature, n the number of electrons involved in the reaction and R_{ct} the charge transfer resistance of the CE at the electrode-electrolyte interface. The limiting current is instead related to:

$$D = \frac{d}{2nFC} I_{lim} \tag{3.3}$$

where D is the diffusion coefficient of the redox couple, d the spacer thickness, C is the triiodide concentration and n and F are the same as above [26].

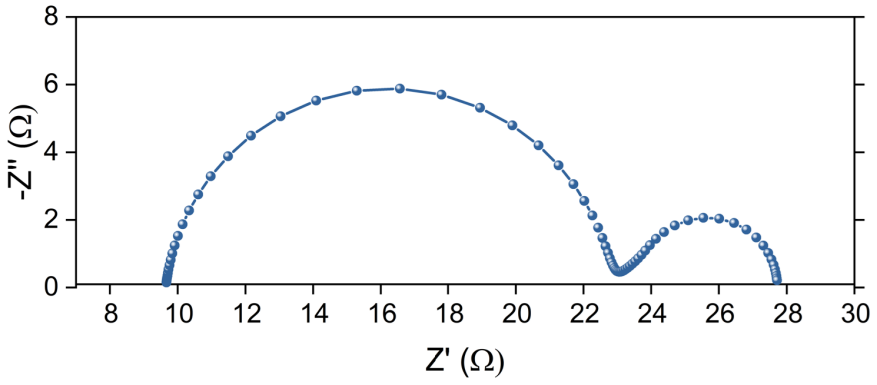

Figure 3.57: The Nyquist plot of various dummy cells [36].

To better understand compound behavior PEIS technique is very handy in a dummy cell configuration: as we can see in **Fig. 3.57**, the Nyquist plot usually shows two semicircles, the left one is related to the electrode-electrolyte charge transfer, as in

the case of SCs; while the right one is representative of the impedance originating by the diffusive transport of redox species toward the electrode caused by a concentration gradient.

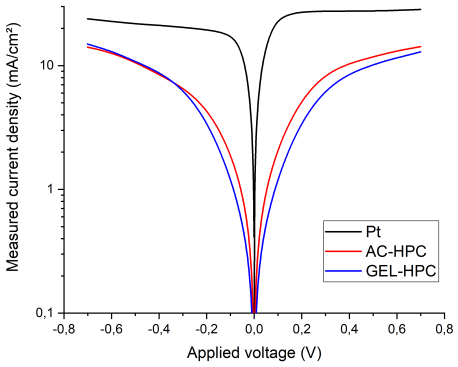

Figure 3.58: Tafel plot of the obtained carbon slurries compared to Pt–sputtered current collector performance.

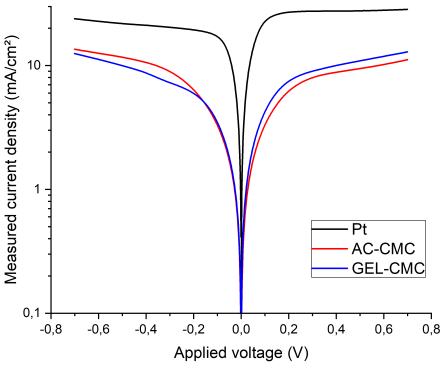

Figure 3.59: Tafel plot of the newly obtained carbon slurries compared to Pt–sputtered current collector performance.

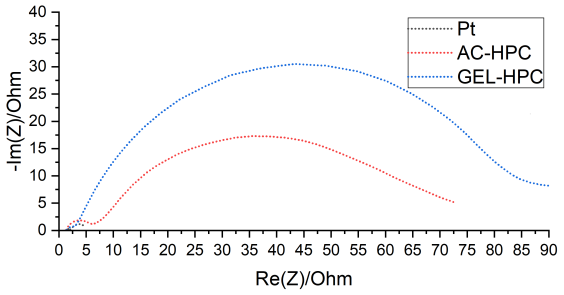

Figure 3.60: Nyquist plot of the processes happening at the electrodes.

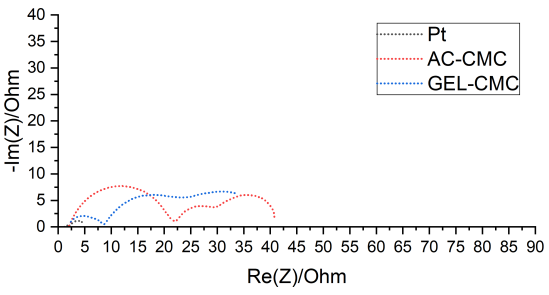

Figure 3.61: Nyquist plot of the processes happening at the electrodes.

Platinum, together with BM–aerogel and AC slurries have been tested in this configuration, obtaining the results depicted in **Fig. 3.58** and **3.60**. From these preliminary results, it appears obvious that in both cases something hinders the charge transfer between electrode and electrolyte, considerably worsening performance not only w.r.t. platinum, but also other literature on carbon-based counter electrodes for DSSCs.

Considered the results, new slurries were prepared using the same weight percentages but substituting HPC with carboxymethyl cellulose (CMC); the results are shown in **Fig. 3.59** and **3.61**. Both the higher slope of the curves in the Tafel plot and

the shrinking of the features of the semicircles in the Nyquist plot show a better catalytic activity of the compounds, with a general decrease in the charge transfer resistance for both carbon-based materials. The current density limit still shows a clear reduction w.r.t. platinum; this could be due to the structure of the slurries, and the different contributions highlighted in **Fig. 3.61** are under investigation. From our understanding of the phenomena, it could be that the iodine/triiodide redox couple is oxidizing the -OH groups that are present in the HPC polymer, forming a gel that increases considerably the charge transfer resistance between electrode and electrolyte; CMC doesn't show signs of reaction instead and is chemically stable. This would explain why the behavior of the slurries containing HPC is anomalous, ultimately making it impossible or at least very limiting to use it with the I^-/I_3^- redox couple. Nonetheless, the possibility to use both AC and BM-aerogel in the right shell as counter electrodes for DSSC has been confirmed.

Chapter 4

Conclusion and future developments

Carbon aerogel and commercially available activated carbon YP-50F (Kuraray) were successfully exploited in combination with lithium manganese oxide to design a sustainable hybrid supercapacitor potentially able to drive, in combination with a dye-sensitized solar cell, low power devices and electronics. The obtained device proves to be stable enough for usage in a variety of charging conditions, and shows low leakage current when fully charged. Despite all the problems encountered, especially during assembly and final testing, results show outstanding cyclability and good capacitance when subjected to simulated currents from a solar-powered source. By further developing this work, there would be a lot of steps needed to improve performance as well as optimizing the procedure:

- As highlighted during carbon aerogel synthesis, it would be nice to recover both silica and carbon sources from the starting material (rice husk), since a procedure has been already developed for separating them [41]. If scalable, the process could truly be a way to dispose of agricultural waste while reusing most of the compounds found in it. It would be also interesting to understand if lignin (eliminated during synthesis) can add a contribution to the total capacitance of the carbon aerogel.
- An activation step addition through the use of chemical (KOH and NaOH) or physical means (steam or CO_2) while pyrolyzing the aerogel would prove beneficial toward the achievement of a very high surface-to-volume ratio during the process, increasing the aerogel performance w.r.t. activated carbon. A perk of using the aerogel over YP-50F can be disorder theory [8], which predicts an increase of EDL capacitance for certain mesoporous structures. Unfortunately, as of right now, the synthesis of carbon aerogel takes too long compared to activated powder (around 2 weeks with the means exploited in this thesis).

If a faster way is found to achieve good quality aerogel, or the procedure is somehow automatized, it could be interesting to continue experimenting; until then methods to obtain activated carbon powder from rice husk should be taken in consideration to speed up testing [3].

- Even if the system proves to be very stable as it is, other faradaic materials could be evaluated in the design. This statement arises from the non-ideal alignment of the ESW of AC and LMO (non-zero voltage across the assembled device terminals), which could cause degradation when the integrated solar cell stops giving energy. The concern about this feature is that when the DSSC becomes a load, it continues to draw current from the energy storage until it is short circuited. This could cause irreversible reactions if the overpotential applied to carbon and LMO is too high. Other than changing the material altogether, future testing of the integrated SC+DSSC system with load is required to get a better understanding of possible problems.
- As only a handful of devices were assembled during final operations, it would be wise to verify repeatability of the tests, since a deposition method in which mass loading is controllable has yet to be found. Without this, it is very difficult to assemble a correctly balanced device without many, many tries.
- HPC as a binder could be substituted to allow an easier monolithic integration, given that it seems to block the iodine/triiodide redox reaction at the counter-electrode of the solar cell. That said, another option is to exploit Cu-based electrolytes, which have been proven to work as well in DSSCs.
- Given the fact that nickel seems to behave as an active compound in supercapacitors [49], its use as a substitute for Ti current collector could prove beneficial in terms of energy and power densities as well as gravimetric capacitance. Further investigations will be conducted.

Bibliography

[1] A. Ahmadpour and D. D. Do. The preparation of active carbons from coal by chemical and physical activation. *Carbon*, vol. 34(4):pp. 471–479, 1996.

[2] Alberto Berrueta, Alfredo Ursùa, Idoia San Martìn, Ali Eftekhari, and Pablo Sanchis. Supercapacitors: Electrical characteristics, modeling, applications, and future trends. *IEEE Access, Special Section on Advanced Energy Storage Technologies and their Applications*, vol. 7, 2019.

[3] Sartaj Ahmad Bhat, Vineet Kumar, Sunil Kumar, A.E. Atabani, Irfan Anjum Badruddin, and Kyu-Jung Chae. Supercapacitors production from waste: A new window for sustainable energy and waste management. *Fuel*, vol. 337:127125, 2023.

[4] Kyle Bradbury. Energy storage technology review. 2010.

[5] M Chen and LL Shao. Review on the recent progress of carbon counter electrodes for dye-sensitized solar cells. *Chemical Engineering Journal*, 304:629–645, 2016.

[6] B.E. Conway. *Electrochemical Supercapacitors: Scientific Fundamentals and Technological Applications*. Springer, Berlin, 1999.

[7] A. Cuesta, P. Dhamelincourt, J. Laureyns, A. Martínez-Alonso, and J.M.D. Tascón. Raman microprobe studies on carbon materials. *Carbon*, 32(8):1523–1532, 1994.

[8] Boris Dyatkin and Yury Gogotsi. Effects of structural disorder and surface chemistry on electric conductivity and capacitance of porous carbon electrodes. *Faraday Discussions*, vol. 172:pp. 139–162, 2014.

[9] A. Eftekhari and F. Molaei. Carbon nanotube-assisted electrodeposition. part i: Battery performance of manganese oxide electrodeposited at low current densities. *J. Power Sources*, vol. 274:pp. 1306–1314, 2015.

[10] A. Eftekhari and F. Molaei. Carbon nanotube-assisted electrodeposition. part ii: Superior pseudo-capacitive behavior of manganese oxide electrodeposited at high current densities. *J. Power Sources*, vol. 274:pp. 1315–1321, 2015.

[11] Takuya Eguchi, Yugo Kanamoto, Masahiro Tomioka, Daisuke Tashima, and Seiji Kumagai. Effect of ball milling on the electrochemical performance of activated carbon with a very high specific surface area. *Batteries*, vol. 6(2):pp. 1–12, 2020.

[12] Yong gang Wang and Yong yao Xia. A new concept hybrid electrochemical supercapacitor: Carbon/limn2o4 aqueous system. *Electrochemistry Communications*, vol. 7(11):pp. 1138–1142, 2005.

[13] Hongcai Gao, Fei Xiao, Chi Bun Ching, and Hongwei Duan. High-performance asymmetric supercapacitor based on graphene hydrogel and nanostructured mno_2. *ACS Applied Materials and Interface*, vol. 4:pp. 2801–2810, 2012.

[14] J. Halme, P. Vaherma, K. Miettunen, and P. Lund. Device physics of dye solar cells. *Advanced Materials*, vol. 22(35), 2010.

[15] Noor I. Jalal et al. A review on supercapacitors: types and components. *Journal of Physics: Conference Series*, 2021.

[16] João I. Yutaka Ota Rodolfo C. Fernandes Rafael Vicentini Cesar J.B. Pagan Leonardo Morais Da Silva João Pedro Aguiar dos Santos, Fernando Cesar Rufino and Hudson Zanin. Best practices for electrochemical characterization of supercapacitors. *Journal of Energy Chemistry*, vol. 80:pp. 265–283, 2023.

[17] Taewhan Ki, Woosung Choi, Heon-Cheol Shin, Jae-Young Choi, Ji Man Kim, Min-Sik Park, and Won-Sub Yoon. Applications of voltammetry in lithium ion battery research. *Journal of Electrochemical Science and Technology*, 2020.

[18] Jesse S. Ko, Chun-Han Lai, Jeffrey W. Long, Debra R. Rolison, Bruce Dunn, and Johanna Nelson Weker. Differentiating double-layer, psuedocapacitance, and battery-like mechanisms by analyzing impedance measurements in three dimensions. *ACS Applied Materials & Interfaces*, vol. 12(12):pp. 14071–14078, 2020.

[19] D. Larcher and J-M. Tarascon. Towards greener and more sustainable batteries for electrical energy storage. *Nature Chemistry*, vol. 7, 2015.

[20] Alexandros Ch. Lazanas and Mamas I. Prodromidis. Electrochemichal impedance spectroscopy - a tutorial. *Measurement Science*, vol. 3:pp. 162–193, 2023.

[21] B Lee, DB Buchholz, and RPH Chang. An all carbon counter electrode for dye sensitized solar cells. *Energy & Environmental Science*, 5(7):9173–9179, 2012.

[22] WJ Lee, E Ramasamy, DY Lee, and JS Song. Performance variation of carbon counter electrode based dye-sensitized solar cell. *Solar Energy Materials and Solar Cells*, 92(7):814–818, 2008.

[23] W. Li, W. R. McKinnon, and J. R. Dahn. Lithium intercalation from aqueous solutions. *Journal of The Electrochemical Society*, vol. 141(9):pp. 2310–2316, 1994.

[24] Yuanyuan Li, Fan Tang, Renjie Wang, Chong Wang, and Jinping Liu. Novel dual-ion hybrid supercapacitor based on a nico2o4 nanowire cathode and moo2-c nanofilm anode. *ACS Applied Materials & Interfaces*, 8:30232–30238, 2016.

[25] Lin-Yu Long, Yun-Xuan Weng, and Yu-Zhong Wang. Cellulose aerogels: Synthesis, applications, and prospects. *Polymers*, 2018.

[26] Muhammad Norhaffis Mustafa, Suhaidi Shafie, Zulkarnain Zainal, and Yusran Sulaiman. A novel poly(3,4-ethylenedioxythiophene)-graphene oxide/titanium dioxide composites counter electrode for dye-sensitized solar cell. *Journal of Nanomaterials*, 2017, 2017.

[27] Ruiqi Na, Nan Lu, Leibo Li, Yudong Liu, Jiashuang Luan, and Guibin Wang. A robust conductive polymer network as a multi-functional binder and conductive additive for supercapacitors. *ChemElectroChem*, vol. 7(n. 14), 2020.

[28] Navid Nasajpour-Esfahani, Davoud Dastan, As'ad Alizadeh, Pouria Shirvanisamani, Mohammadreza Rozati, Eden Ricciardi, Bo Lewis, Ashish Aphale, and Davood Toghraie. A critical review on intrinsic conducting polymers and their applications. *Journal of Industrial and Engineering Chemistry*, vol. 125:pp. 14–37, 2023.

[29] Panasonic. Basic knowledge about capacitors.

[30] Marc Perez and Richard Perez. Update 2022 – a fundamental look at supply side energy reserves for the planet. *Solar Energy Advances*, 2:100014, 2022.

[31] Jae-Seung Roh. Structural study of the activated carbon fiber using laser raman spectroscopy. *Carbon letters*, 9, 06 2008.

[32] P.W. Ruch, D. Cericola, M. Hahn, R. Kötz, and A. Wokaun. On the use of activated carbon as a quasi-reference electrode in non-aqueous electrolyte solutions. *Journal of Electroanalytical Chemistry*, vol. 636:pp. 128–131, 2009.

[33] Marina Schwan, Jessica Schettler, Felix M. Badaczewski, Charlotte Heinrich, Bernd M. Smarsly, and Barbara Milow. The effect of pulverization methods on the microstructure of stiff, ductile, and flexible carbon aerogels. *Journal of Materials Science*, vol. 55:pp. 5861–5879, 2020.

[34] Manuel Scimeca, Simone Bischetti, Harpreet Kaur Lamsira, Rita Bonfiglio, and Elena Bonanno. Energy dispersive x-ray (edx) microanalysis: A powerful tool in biomedical research and diagnosis. *European journal of histochemistry*, vol. 62, 2018.

[35] N. Shimodaira and A. Masui. Raman spectroscopic investigations of activated carbon materials. *J. Appl. Phys.*, 92:902–909, 2002.

[36] Roberto Speranza, Marco Reina, Pietro Zaccagnini, Alessandro Pedico, and Andrea Lamberti. Laser-induced graphene as a sustainable counter electrode for dssc enabling flexible self-powered integrated harvesting and storage device for indoor application. *Electrochimica Acta*, 460:142514, 2023.

[37] Sang Hoon Sung, Sunhyung Kim, Jeong Hoon Park, Jun Dong Park, and Kyung Hyun Ahn. Role of pvdf in rheology and microstructure of ncm cathode slurries for lithium-ion battery. *Materials*, vol. 13(20), 2020.

[38] Michael M. Thackeray. Manganese oxides for lithium batteries. *Progress in Solid State Chemistry*, 25(1-2):1–71, 1997.

[39] F. Tuinstra and J. L. Koenig. Raman spectrum of graphite. *Journal of Chemical Physics*, 53:1126, 1970.

[40] John Wang, Julien Polleux, James Lim, and Bruce Dunn. Pseudocapacitive contributions to electrochemical energy storage in tio_2 (anatase) nanoparticles. *The Journal of Physical Chemistry C*, vol. 111(40):pp. 14925–14931, 2007.

[41] Zichao Wei, Andrew T. Smith, William R. T. Tait, Jingjing Liu, Hao Ding, Hui Wang, Weixing Wang, and Luyi Sun. Lignocellulose aerogel and amorphous silica nanoparticles from rice husks. *Journal of Leather Science and Engineering*, vol. 3, 2021.

[42] Wahyu Widanarto et al. Production of reduced graphene oxide from activated rice husk charcoal using a high-energy ball milling method. *Physica Scripta*, vol. 98, 2023.

[43] Wikipedia. Capacitor.

[44] Daxiong Wu and et al. Roadmap on aqueous batteries. *Journal of Physics Energy*, vol. 4, 2022.

[45] Z.-S. Wu, W. Ren, D.-W. Wang, F. Li, B. Liu, and H.-M. Cheng. High-energy mno2 nanowire/graphene and graphene asymmetric electrochemical capacitors. *ACS Nano*, vol .4(n. 10):pp. 5835–5842, 2010.

[46] Renlu Yuan, Yue Dong, Ruoyang Hou, Lei Shang, Jiapeng Zhang, Su Zhang, Xiaohong Chen, and Huaihe Song. Structural transformation of porous and disordered carbon during ball-milling. *Chemical Engineering Journal*, 454:140418, 2023.

[47] P. Zaccagnini, Y. Tien, L. Baudino, A. Pedico, S. Bianco, and A. Lamberti. Optimization of laser-induced graphene electrodes for high voltage and highly stable microsupercapacitors. *Advanced Materials Technologies*, 8(1):2300833, 2023.

[48] Dacheng Zhang, Xiong Zhang, Yao Chen, Peng Yu, Changhui Wang, and Yanwei Ma. Enhanced capacitance and rate capability of graphene/polypyrrole composite as electrode material for supercapacitors. *Journal of Power Sources*, vol. 196:pp. 5990–5996, 2011.

[49] Liuyang Zhang, Diwen Shi, Tao Liu, Mietek Jaroniec, and Jiaguo Yu. Nickel-based materials for supercapacitors. *Materials Today*, 25:35–65, 2019.

[50] Sanliang Zhang and Ning Pan. Supercapacitors performance evaluation. *Advanced Energy Materials*, vol.5, 2015.

[51] He Zhou, Xin-Hua Wang, Hai-Zhen Liu, Shi-Chao Gao, and Mi Yan. Improved hydrogen storage properties of libh4 confined with activated charcoal by ball milling. *Rare Metals*, vol. 38(4):pp. 321–326, 2019.

[52] Ana D. Đurović, Zorica S. Stojanović, Snežana Ž. Kravić, Zvonimir J. Sutorović, Tanja Ž. Brezo, Nada L. Grahovac, and Spasenija D. Milanović. A comparison of different methods to remove dissolved oxygen: Application to the electrochemical determination of imidacloprid. *Acta Periodica Technologica*, vol. 46:pp. 149–155, 2015.